AN OBSERVATIONAL STUDY OF THE SOUTH PACIFIC CONVERGENCE ZONE USING SATELLITE AND MODEL RE-ANALYSIS DATA

A Dissertation

by

STEPHEN B. COCKS

Submitted to the Office of Graduate Studies of
Texas A&M University
in partial fulfillment of the requirements for the degree of

DOCTOR OF PHILOSOPHY

December 2003

Major Subject: Atmospheric Sciences

AN OBSERVATIONAL STUDY OF THE SOUTH PACIFIC CONVERGENCE ZONE USING SATELLITE AND MODEL RE-ANALYSIS DATA

A Dissertation

by

STEPHEN B. COCKS

Submitted to the Office of Graduate Studies of
Texas A&M University
in partial fulfillment of the requirements for the degree of

DOCTOR OF PHILOSOPHY

Approved as to style and content by:

Richard Lee Panetta (Chair of Committee)	Thomas Wilheit (Member)
Ping Chang (Member)	Richard Orville (Member)

Richard Orville
(Head of Department)

December 2003

Major Subject: Atmospheric Sciences

ABSTRACT

An Observational Study of the South Pacific Convergence Zone

Using Satellite and Model Re-Analysis Data. (December 2003)

Stephen B. Cocks, B.S., University of Oklahoma;

M.S., Colorado State University

Chair of Advisory Committee: Dr. Richard Lee Panetta

Satellite derived wind, rain rate and sea surface temperature data combined with NCEP analysis data are used to examine the structure of the South Pacific Convergence Zone (SPCZ) during La Nina conditions. Annual means indicate that the axes of maximum surface convergence and rain rates are essentially co-located in the Northern Hemisphere Inter-Tropical Convergence Zone and over the tropical (TR) portions of the SPCZ. However, over sub-tropical (ST) and middle latitudes (ML), the axis of maximum convergence is eastward and equatorward of the axis of maximum rain rates such that surface divergence predominates over the these portions of the SPCZ rain rate maximum. Analysis of NCEP data also exhibit a similar convergence distribution at 1000 hPa; however, at the 925, 850 and 700 hPa levels convergence replaces divergence and is co-located with the axis of maximum rain rates. Seasonal rain rate patterns indicated that the TR and ST SPCZ are more convectively active during Austral Summer and Fall while the ML SPCZ is more active during the Fall and Winter. Vertical wind shear and the variability of the meridional flow indicate the ML SPCZ is strongly associated with the mid-latitude storm track while the TR SPCZ is associated with low wind shear. The ST SPCZ represents a transition zone between an environment dominated by low shear and one that is more baroclinic.

Lag correlation analysis using rain rate, 200 hPa divergence and height anomaly data as well as composite analysis of high rain fall events revealed wave like patterns over the ST and ML SPCZ. The estimated wavelengths range from 4700 to 5500 km, values that correspond to wave numbers 7 and 8; individual anomalies tend to move eastward at speeds of 5 to 7 m/s. The vertical structure of the height anomalies suggest baroclinic dynamics are important to the development of the mean rainfall pattern in the ML SPCZ and to a lesser extent the ST SPCZ. During high rain rate events, only a given portion of the SPCZ, approximately 3000 to 4000 km in length, is convectively active.

TABLE OF CONTENTS

Page

ABSTRACT iii

TABLE OF CONTENTS v

LIST OF FIGURES vii

LIST OF TABLES xi

CHAPTER

I INTRODUCTION 1

The South Pacific Convergence Zone 1
Previous Observational Work 3
Numerical Model Studies 5
Issues Explored 7

II DATA SETS USED 9

NCEP Re-Analysis Data 9
Scatterometer Data 10
Satellite Derived SST Data 14
Satellite Derived Rain Rates 17
Data Set Distributions 24

III ANNUAL DISTRIBUTIONS OF SOME PHYSICAL PARAMETERS IN THE SPCZ 28

Distribution of Rain Rates and SSTs across the Pacific 28
Distribution of Convergence across the Pacific 30
Scatter Plots of Rain Rates and Divergence 46
Lightning Characteristics in the SPCZ Region 48
Summary 49

IV SEASONAL DISTRIBUTIONS OF SOME PHYSICAL PARAMETERS IN THE SPCZ 52

Seasonal Distribution of SSTs, Rain Rates and Vertical Wind Shear 52
Seasonal Distribution of Convergence 60
The Vertical Distribution of Convergence and Heights 67

CHAPTER Page

Seasonal Scatter Plots of Rain Rates and Divergence 76
Summary 82

V LAG CORRELATION ANALYSIS 87

Introduction 87
Correlation Analysis Methods 88
Spectra and Auto/Cross Correlation of Rain, Height and Div. within the SPCZ 92
Lag Correlation Using Rain Rate Anomalies 98
Lag Correlation Using Rain Rate and Divergence Anomalies 102
Lag Correlation Using Rain Rates and Height Anomalies 106
Summary 110

VI COMPOSITES OF HIGH AND LOW RAIN RATE EVENTS 112

Compositing Methodology 112
Seasonal Trends for High and Low Rain Rate Days 113
HRRD Composites of the SPCZ Test Regions 117
LRRD Composites of the SPCZ Test Regions 129
Vertical Structure of Height Anomalies for HRRD Composites 129
Summary 136

VII SUMMARY AND CONCLUSIONS 139

REFERENCES 146

APPENDIX 153

VITA 155

LIST OF FIGURES

FIGURE Page

1. A three year average (1998-2001) of global annual precipitation (totaled in mm) estimated from Microwave Sounding Unit data 1

2. Schematic illustrating Kodama's model for Sub-Tropical Convergence Zones 5

3. Example of coverage gaps for approximately one day in scatterometer data; the large gap in the Pacific Ocean is the result of data not yet ingested..... 11

4. Three day average of SSTs calculated without smoothing (top) and with smoothing (bottom) 16

5. Schematic of what happens to microwave radiation as it passes through the atmosphere, reflects off the ocean and back into space 18

6. Schematic of the contribution, in terms of microwave emission, from various atmospheric constituents to the microwave derived brightness temperature (Tb) 20

7. Schematic of the algorithm used to create GPCP rain rate data 23

8. Test regions used for quantitative analysis in chapters III through VI 24

9. Histograms of 500 HPa height anomalies for the TR, ST and ML SPCZ regions 25

10. Histograms of rain rate anomalies for the TR, ST and ML SPCZ regions..... 26

11. Three year average of SSTs (shaded) and rain rates (contoured) over the South Pacific and the tropical North Pacific..... 28

12. Three year average of 850-200 hPa vertical wind shear (shaded) with rain rates (contoured) over the tropical North and the South Pacific..... 29

13. Two year average of SSTs (shaded) and scatterometer derived convergence (top) and divergence (bottom; contoured & in units * 10^6) over the South Pacific and the tropical North Pacific 31

14 Two year average of scatterometer derived convergence (top) and divergence (bottom; shaded & in units * 10^6) and rain rates (contoured) over the tropical North and the South Pacific 33

15. Two year average of scatterometer derived convergence only (shaded & in units * 10^6) and rain rates (contoured) over the tropical South and the North Pacific..... 34

FIGURE Page

16. Mean square root and mean of rain rates (top), mean square root of convergence and mean of rain rates (bottom) 35

17. Comparison of GPCP and NCEP rain rates to scatterometer derived convergence (only) as follows: top, a three year average of GPCP and NCEP rain rates; bottom, a two year average of NCEP rain rates and convergence 37

18. Three year average of GPCP rain rates (shade) and NCEP re-analysis derived convergence (contoured) over the tropical North and the South Pacific..... 38

19. Three year average of GPCP rain rates (shade) and NCEP re-analysis heights (contoured) over the tropical North and the South Pacific..... 41

20. Scatter plots of rain rates and divergence for the surface through 850 hPa layers for the atmosphere: 'TR' denotes tropical, and 'ST' sub-tropical SPCZ 44

21. Scatter plots of rain rates and divergence for the surface through 850 hPa layers for the atmosphere: 'ML' denotes mid-latitude SPCZ, and 'NPCZ' a region located within the North Pacific storm track 45

22. The number of lightning strikes (flashes) for a given portion of the South Pacific during 1999 and 2000..... 47

23. Seasonal averages of rain rates (contoured) and SSTs (shade) 53

24. Seasonal averages of rain rates (contoured) and 850-200 hPa vertical wind shear (shade)..... 55

25. Seasonal averages of rain rates (contoured) and the standard deviation of the 200 hPa wind (shade)..... 58

26. Seasonal averages of surface convergence (contoured) and SSTs (shade) 61

27. Seasonal averages of scatterometer derived surface convergence (shade) and rain rates (contours)..... 65

28. Three year average of 1000 and 850 hPa convergence (contours) and rain rates (shade) during Austral winter..... 68

29. Same as figure 28 except for September through November..... 69

30. Same as figure 28 except for December through February..... 70

31. Same as figure 28 except for March through May..... 71

FIGURE Page

32. Three year average of 1000 and 850 hPa heights (contours) and winds (vectors) along with rain rates (shade) during Austral winter 72

33. Same as figure 32 except for September through November 73

34. Same as figure 32 except for December through February 74

35. Same as figure 32 except for September through November 75

36. Schematic illustrating the effect of the surface on wind flow around high and low pressure areas 76

37. Summer (left) and fall (right) scatter plots of rain rates and divergence for the surface through 850 hPa layers of the TR SPCZ 77

38. Same as figure 37 except for the ST SPCZ 78

39. Same as figure 37 except for the ML SPCZ 79

40. Two conceptual ideas illustrating how the SPCZ becomes convectively active for a given time period 88

41. Average rain rate time series for gridpoints in the TR, ST and ML SPCZ test regions 90

42. Normalized spectra of satellite derived rain rates for the TR SPCZ region 91

43. Normalized, smoothed spectra of satellite derived rain rates for the TR, ST and ML SPCZ 93

44. Auto-correlation functions for rain rate anomalies in the TR, ST and ML SPCZ 94

45. Cross-correlation functions between rain rate anomalies in one section of the SPCZ with rain rates in another SPCZ section 96

46. Auto-correlation functions for 200 hPa height anomalies in the TR, ST and ML SPCZ 97

47. Backward and forward lag correlation results of rain rates within the TR SPCZ test region (black box) with the rest of the South Pacific 99

48. Same as figure 47 except for the ST SPCZ 100

49. Same as figure 47 except for the ML SPCZ 101

FIGURE Page

50. Backward and forward lag correlation results of rain rates within the TR SPCZ test region (black box) with 200 hPa divergence across the rest of the South Pacific 103

51. Same as figure 50 except for the ST SPCZ..... 104

52. Same as figure 50 except for the ML SPCZ 105

53. Backward and forward lag correlation results of rain rate anomalies within the TR SPCZ test region (black box) with 500 hPa height anomalies across the rest of the South Pacific..... 107

54. Same as figure 53 except for the ST SPCZ..... 108

55. Same as figure 53 except for the ML SPCZ 109

56. Histograms of High Rain Rate Days (HRRDs) by month for the TR, ST (top) and ML SPCZ (bottom)..... 115

57. Same as 56 except for Low Rain Rate Days (LRRDs)..... 116

58. Composite of HRRDs over the TR region..... 118

59. Same as figure 58 except for the ST SPCZ..... 120

60. Same as figure 58 except for the ML SPCZ 122

61. Raw rain rates (shaded) and 200-850 hPa shear for HRRD composite Day 0 for the various SPCZ test regions..... 123

62. Composite of LRRDs over the TR region 126

63. Same as figure 62 except for the ST SPCZ..... 127

64. Same as figure 62 except for the ML SPCZ 128

65. Raw rain rates (shaded) and 200-850 hPa shear for LRRD composite Day 0 for the various SPCZ test regions..... 130

66. Day 0 composite with 200, 500 and 850 hPa height anomalies (solid/dashed lines), rain rates (shaded) and the zero contour of the mean zonal wind (dash-dot) for TR SPCZ..... 132

67. Same as figure 66 except for the ST SPCZ..... 133

68. Same as figure 66 except for the ML SPCZ 134

LIST OF TABLES

TABLE Page

1. Correlation of rain rates vs. 200 hPa divergence for different combinations of the TR, ST and ML SPCZ using a three year period. 98

2. The percentage of HRRD, VHRRD and LRRD days comprising the dataset and the percentage of rain contributed to the total rainfall for each SPCZ test region 114

CHAPTER I

INTRODUCTION

The South Pacific Convergence Zone

The South Pacific Convergence Zone (SPCZ) is a northwest to southeast oriented zone of persistent cloudiness and rainfall extending from New Guinea southeastward across the international dateline into middle latitudes and is frequently observed in climatology studies

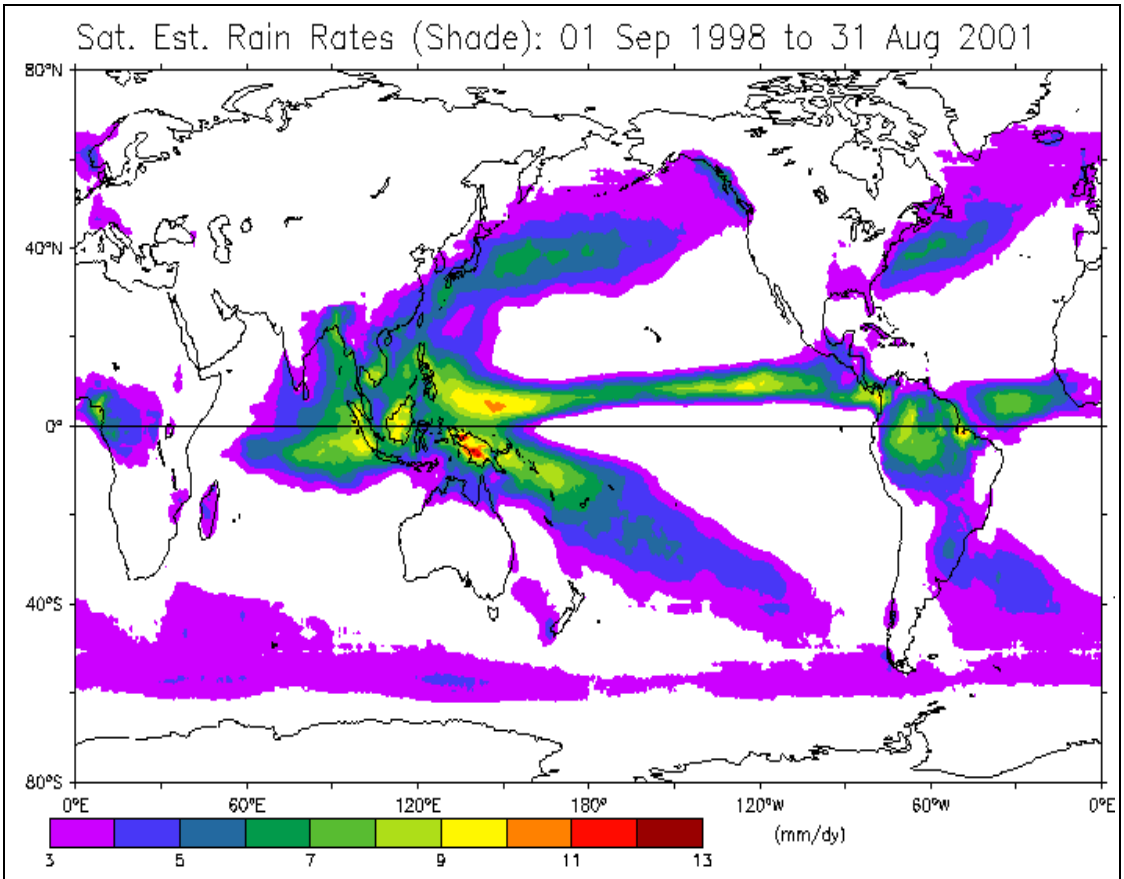

Figure 1: A three year average (1998-2001) of global annual precipitation (totaled in mm) estimated from Microwave Sounding Unit data.

This dissertation follows the style and format of the *Journal of Climate*.

(Waliser and Gautier, 1993; Spencer, 1993). Figure 1 is a three year average of rainfall showing the major precipitation maxima of the world, including the SPCZ. Although there are similarities, such as the southeastward or northeastward orientation of the rain rate pattern, there are some unique differences between the SPCZ and other precipitation maxima. The precipitation maxima off the Asian, North and South American coasts appear to extend from a major land mass; the SPCZ does not. The SPCZ extends from the deep tropical regions into higher latitudes while the other precipitation maxima tend to begin in sub-tropical latitudes. Although not visible in figure 1, other studies have suggested a distinct structure within the SPCZ rain rate maximum. Vincent (1982, 1994) noted a similar structure in satellite and sea level pressure patterns in the SPCZ region during a three week period. At tropical latitudes, the rain rate diagonal appears to extend more zonally while at sub-tropical and higher latitudes it extends more towards the southeast. Vincent called the west-to-east oriented cloud band in the tropical latitudes the zonal SPCZ. The northwest-to-southeast oriented cloud band in sub-tropical and higher latitudes he called the diagonal SPCZ. This structure is interesting because it may indicate differences between dynamical processes producing rainfall in the tropics and those at higher latitudes. The zonal SPCZ is a location where warm ($\geq 26°C$) Sea Surface Temperatures (SSTs) and persistent low-level convergence create an environment favorable for deep convection throughout the year. The SPCZ diagonal, however, lies across much cooler SSTs therefore deep convection is much more dependent upon short term changes in the atmosphere that allow atmospheric stability to decrease.

The author was an operational weather forecaster in the tropical Pacific for three years and has personally observed a range of disturbances, from weak depressions to intense tropical cyclones, develop within tropical portions of the SPCZ and eventually track poleward. This isn't surprising as investigators have documented the existence of tropical cyclogenesis in the region

(Gray; 1968; Gray, 1975; Vincent, 1982). However, the author has also observed the passage of middle latitude frontal systems within the SPCZ region, with cloud bands appearing to extend from tropical to middle latitudes. These observations lead to questions about how the SPCZ rain rate maximum develops.

Previous Observational Work

The circulation of the South Pacific Ocean, and hence the SPCZ, was not well known until the coming of the satellite age. Early analysis of satellite imagery by a number of investigators (Godshall, 1968; Gruber, 1972; Streten, 1973) established the presence of a persistent cloud band across the South Pacific Ocean. Streten's (1973) analysis suggested the cloud band location was closely related to a mid-latitude, long-wave trough. Trenberth (1976) reported that the SPCZ appeared to be linked to the easternmost extension of the Australian Monsoon west of 180°E. East of the dateline the SPCZ had the appearance of a convergence zone in association with a prominent sub-tropical jet. He also noted that changes in the SPCZ's position are related to the Southern Oscillation. When surface pressures are low over Indonesia/northern Australia and high in the South Pacific, the SPCZ lies further south and slightly west of its mean position. On the other hand, when surface pressures are high over Indonesia/northern Australia and low in the South Pacific, the SPCZ lies further north and east of its mean position. Using five-day averaged satellite data, Streten (1978) noted the SPCZ cloud band tended to exhibit slow eastward motion followed by a rapid shift westward; this motion had a quasi-periodicity of 20-25 days. He hypothesized cloud band position changes were related to the passage of mid-latitude troughs.

Using ECMWF Level III-b analysis derived from data collected during FGGE, Vincent (1982) examined the circulation of the SPCZ cloud band for a nine-day period in January, 1979. He found that vertical wind shear was weak within the zonal section of the SPCZ which suggested to him that latent heat processes are more important to the development and

maintenance of this feature. In the SPCZ diagonal, the presence of significant amounts of vertical wind shear indicated baroclinic processes were important. He also found that a sub-tropical jet was present and parallel to the cloud band. Huang and Vincent (1983) documented how changes in the SPCZ cloud band were related to changes in the large-scale synoptic environment during the period 10-27 January, 1979. Initially, the SPCZ cloud band was located eastward and equatorward of an upper level northwest-to-southeast oriented trough. As the trough became more meridionally oriented, the diagonal section also assumed the same orientation. As the trough weakened and the upper level zonal flow became more zonal the SPCZ cloud band dissipated.

The association of an upper level trough and sub-tropical jet to the SPCZ cloud band was also noted by Kiladis and Weickmann (1992a). They found evidence suggesting the presence of upper level troughs located west of negative Outgoing Longwave Radiation (OLR) anomalies in the SPCZ. The troughs attained maximum amplitude prior to a minimum in the OLR anomalies implying that troughs are either forcing, or at least enhancing convection within the SPCZ. Kiladis and Weickmann (1992b) analyzed a case study suggesting the importance of mid-latitude dynamics to the development of an SPCZ cloud band. During a four day period, a mid-latitude trough reached maximum amplification one day prior to the development of a solid band of convection stretching from tropical to mid-latitude regions. The cloud band dissipated as the mid-latitude trough weakened and upper level flow became more zonal. These findings led Kiladis and Weickmann to conclude that the SPCZ is a region of frequent frontal activity interacting with warm, moist trade flow from the South Pacific High and cool southeasterly flow ahead of transient anti-cyclones. They speculated that the SPCZ climatological rainfall pattern is the net result of an aggregate of surface fronts enhancing convection in the region.

Using NMC global objective analysis and OLR data, Kodama (1992 and 1993) claimed that the SPCZ was similar to other regions of persistent clouds and rain found in the sub-tropics. He called these regions Sub-Tropical Convergence Zones (STCZs) and found they develop when two synoptic conditions were met. The first was the existence of moist, low-level, poleward flows on the western periphery of the sub-tropical highs. The second was the presence of an upper level sub-tropical jet which lay parallel to and along the cloud band. The cloud band was located on the eastern periphery of an upper level trough. If only one of these criteria was met, then only weak rainfall areas (or none at all) developed in the sub-tropics. These large scale features are illustrated in figure 2.

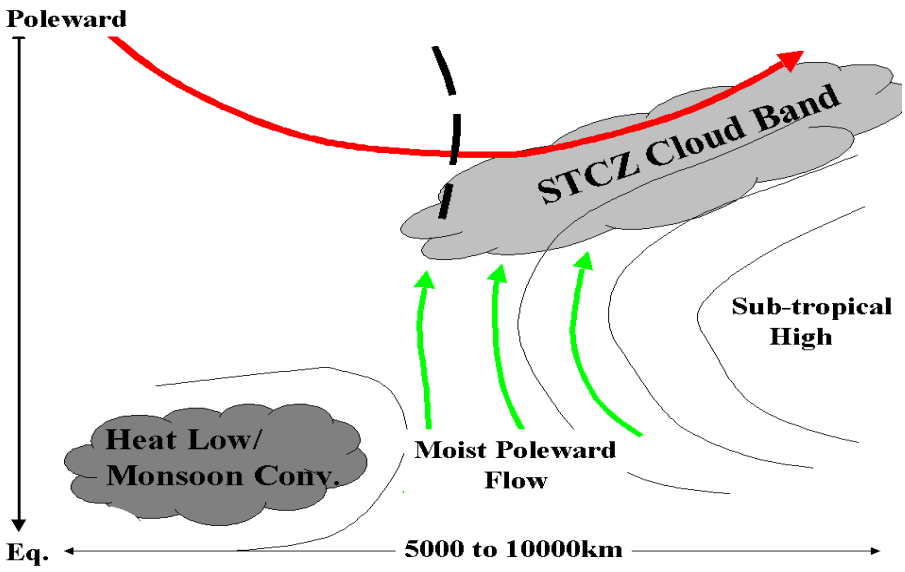

Figure 2: Schematic illustrating Kodama's model for Sub-Tropical Convergence Zones. The solid red line denotes the sub-tropical jet in sub-tropical latitudes, dashed black line the upper level trough axis, thin black lines isobars of sea-level pressure, and the solid green lines the moist poleward flow. This figure was adapted from Kodama (1993).

Numerical Model Studies

There have been a number of numerical studies that have important implications for the SPCZ. Using a linear, viscous model Gill (1980) studied the response of the atmosphere to a

tropical heat source. He found that the atmospheric response to a heat source centered along the equator would be the development of an equatorial trough with twin cyclones on the northwest and southwest flanks of the forcing region. As the heat source is moved off of the equator into tropical latitudes of either the Northern or Southern Hemisphere, the cyclone in the same hemisphere intensifies at the expense of the other cyclone (in the other hemisphere). The resulting wind flow is somewhat reminiscent of a monsoon like circulation. Hendon (1986) used a simplified non-linear model to show that strong heat sources can radiate stationary Rossby wave trains into the mid-latitudes. Kodama (1999) used an aqua planet, GCM simulation to examine the atmosphere's response to a heat source as it is moved off the equator and the specific implications for STCZs. He found the formation of a model STCZ was strongly dependent upon the latitude of the heat source. A heat source north of the equator led to the development of a southwest-to-northeast oriented surface low that stretched from tropical to sub-tropical regions. The surface low induces the wind flow such that moisture laden air is advected into the subtropics with moisture convergence occurring east of the trough axis. The result is the development of deep convection and hence rainfall. The strong convective outflow aloft developed and maintained a strong upper level jet. The upper level westerly flow tended to extend well into the lower troposphere during rainy periods (as simulated by the model).

Kiladis et al. (1989) examined whether the orientation of the SPCZ diagonal was related to the distribution of SSTs or land mass in the Southern Hemisphere. Using climatological data for rainfall, SSTs and surface wind convergence during the month of January, they found the axis of maximum rainfall was equatorward of the axis of maximum surface wind convergence; in turn, the axis of maximum rainfall lay poleward of the axis of maximum SSTs (their figure 1). This result indicated that the orientation of the SPCZ was not simply related to the SST distribution. Kiladis et al. conjectured that the distribution of continents affected the SPCZ's position and

proceeded to investigate this idea with numerical simulations. Simulations were conducted with South America removed, Australia removed and one where both continents were included (the control run. Their results showed the removal of the South American continent had little substantial effect on the precipitation and surface pressure pattern in the SPCZ region. However, the removal of Australia, through removal of the continental heat low, eliminated the Australian monsoon circulation. This resulted in a significantly weakened SPCZ as observed in the model.

Webster and Holton (1982) conducted numerical experiments to gain insight into the possibility that mid-latitude cyclones can affect tropical convection. Using a non-linear shallow water model, they found mid-latitude Rossby waves have little affect on equatorial regions if a region of easterly flow exists between the disturbance source and the equator. However, mid-latitude Rossby waves may significantly influence equatorial regions if an area of westerly flow exists between the wave and the tropics, and the zonal wavelength is less than the zonal length of the westerly flow duct. The wave's magnitude of forcing in the tropics was strongly dependent on the magnitude of the equatorial westerly flow. Across portions of the SPCZ diagonal, the January 200 HPa westerly flow can extend into the sub-tropical and tropical latitudes with velocities of 5 to 15 m/s (Sadler, 1975; Webster and Holton, 1982). Therefore, the possibility exists that mid-latitude Rossby waves may enhance convection over a large portion of the SPCZ under the right conditions.

Issues Explored

Although climatologies of the South Pacific are available, there have not been many that focused on the SPCZ. Additionally, there have been studies on the potential influence of upper level troughs on SPCZ convection but I wish to further extend this idea. This research project will try to answer the following questions. Are there any distinct seasonal variations in rainfall within the SPCZ and if so, do different sections of the SPCZ become active during different

seasons? Is there a relationship between convection in the tropics and that in the middle latitudes within the SPCZ? How important are mid-latitude cyclones to the development of rainfall within the SPCZ? Do mid-latitude cyclones have an affect on convection in tropical portions of the SPCZ? To answer these questions, I will explore the horizontal and vertical structure of the SPCZ over a three year period using a combination of satellite and model analysis data. The annual and seasonal distribution of various physical parameters, as well as their horizontal and vertical structure in the atmosphere, will be examined in this study. Lag correlation analysis will be used to investigate how the SPCZ becomes convectively active during synoptic scale events. It will also be used to determine the importance of mid-latitude troughs in the development of rain rates in the SPCZ. Composite analysis will be used to highlight the horizontal and vertical structure of the atmosphere during high and low rain rate events within the SPCZ.

CHAPTER II

DATA SETS USED

In order to study the South Pacific Convergence Zone (SPCZ) on seasonal and shorter time scales, observations with a high spatial and temporal resolution are desired. Unfortunately, there are very few ship and island observations available in these remote regions. However, over the past ten years a number of high quality data sets have become available for research in the traditionally data void regions such as the South Pacific Ocean. I will summarize below those which I used for this study.

NCEP Re-Analysis Data

As the South Pacific is generally a remote ocean basin, wind and height fields will have to come from model analyses derived from what few observations are available. In recent years, the NCEP-NCAR Re-analysis project has made quality research data widely available (Kistler, et al. 2001; Kalnay et al. 1996). The data has a grid resolution of 2.5 x 2.5 degrees and is available in one day time steps. The wind and height fields produced by the re-analysis does incorporate satellite cloud drift winds and sounder data. These fields are classified as class 'A' variables, that is, those variables that are strongly influenced by available observations and are considered the most reliable produced by the re-analysis project (Kalnay et al; 1996). NCEP rain rate data is also examined in this research project but is used with care. The reason for the caution is that rain rate is a class 'C' NCEP variable. This means there are no observations directly affecting the variable and it is solely derived from the model fields.

There are some drawbacks to using NCEP re-analysis data. In a comparison with a subjective analysis of monthly ship observations over the tropical Pacific, NCEP-NCAR re-analysis surface wind flow was found to be suspect within approximately 10°N-10°S (Putman, et al., 2000). Additionally, there are very little data over the South Pacific for the model to ingest; therefore,

there will likely cases where the re-analysis does not detect synoptic scale systems that might otherwise be found if observational data were available. Nonetheless, I can use these data in conjunction with satellite derived data sets and if there is good agreement I will have confidence in using the NCEP data.

Scatterometer Data

Over the past several years satellite-based sensors have provided a wealth of data especially suited for atmospheric studies over the oceans. The data from one such instrument, the scatterometer, can be used to determine the near surface wind direction and speed with accuracy. How is this possible? When the wind blows across the ocean's surface it induces many kinds of waves, each with its own amplitude and period. From space, the scatterometer emits radiation towards the sea surface where those waves that are close to the wavelength of the radar will backscatter the radiation through Bragg Scattering. Bragg Scattering describes the process where reflected radiation from one wave reinforces, or cancels, that from the successive wave depending upon the spacing of the waves and the viewing geometry (Kidder & Vonder Haar, 1995). As the radar has a wavelength of approximately two centimeters, capillary waves, with a length scale on the order of centimeters, are largely responsible for the backscattered radiation. Studies with aircraft mounted radar in the 1960s indicate the backscattered radiation from capillary waves is related to the local surface wind speed. Direction can be determined via multiple scans of the same location on the sea surface from different azimuth angles. A complicated model function is used to extract wind speed and direction from the backscattered radiation from the different sensor scans (Kidder & Vonder Haar, 1995). A number of scatterometers have been placed in orbit; the data I used in this study comes from the QuikSCAT instrument, placed in space in early 1998 as a short-notice replacement for the failed NASA Scatterometer (NSCAT). The QuikSCAT scatterometer uses two conically rotating beams at

incidence angles of approximately 46° and 54° to "sense" the sea surface. The resulting data swaths are 1600 km wide (Schlax, et al, 2000) with a resolution of approximately 25 km (Bourassa et al, 2003). Bourassa et al. (2003) compared scatterometer data obtained from the QuikSCAT instrument to ship observations that were spatially and temporally co-located with the satellite swath. Under rain-free conditions, the results showed that using QSCAT-1 and Kuo-2000 model functions to extract wind speed and direction, uncertainties of 0.45m/s and 5° and 0.3m/s and 3° respectively were found. The data were nearly perfect in determining direction for surface wind speeds greater than 8 m/s although ambiguity errors exceeded 20° for wind speeds

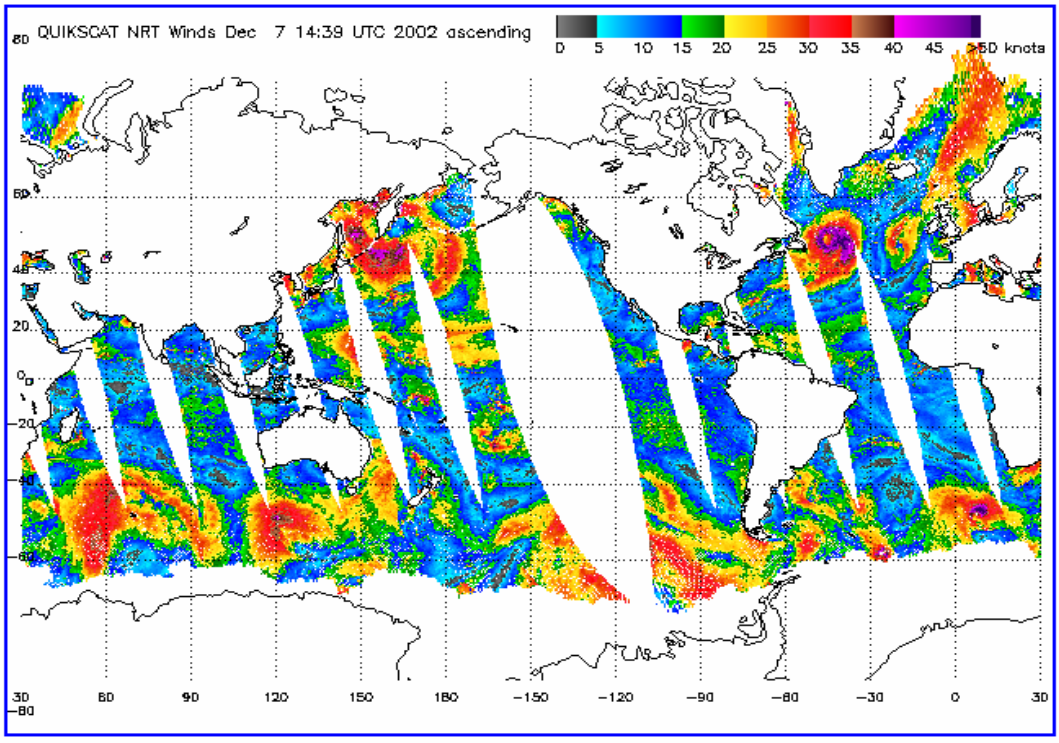

Figure 3: Example of coverage gaps for approximately one day in scatterometer data; the large gap in the Pacific Ocean is the result of data not yet ingested.

less than 5m/s. A disadvantage to using Quikscat, or for that matter any low orbiting satellite data, is the episodic nature of its availability for a given location and time. As the Quikscat

sensor has a rather narrow swath, the data obtained does not completely overlap within a twenty four hour period resulting in coverage gaps as shown in figure 3. The challenge for researchers became how to fill these data gaps in a meaningful way so as to provide a continuous, daily data set. Pegion et al. (2000) used a complex statistical technique to fill these data gaps and create gridded wind fields using data from the now defunct NSCAT scatterometer. An eight day weighted temporal running average of NSCAT data was used to create a smooth background field which functions as an initial guess for gaps between satellite swaths. Next, wind stress fields were created by directly minimizing a "cost function," an algorithm used to maximize the information available from scatterometer data swaths and minimize smoothing. Daily scatterometer data and the background field are entered into the cost function equation which is subsequently solved for a minimum (see Pegion, et al. (2000) for additional details). The resulting output is a zonal and meridional wind component at every grid point for the region in question.

The uncertainties in a gridded wind field are expected to be larger than those associated with individual comparisons with ship/buoy observations due to sampling errors. Schlax, et al. (2000) carefully examined this topic using idealized data for six different scatterometer missions. Within swaths, the data distribution is uniform but the swaths themselves are not uniformly distributed due to the satellites' retro-grading orbits; therefore, the space-time sampling pattern is extremely complex. The temporal sampling pattern exhibits bursts of closely spaced satellite swaths followed by longer gaps before data at one location became available again. All of these effects result in a pattern that is highly variable with longitude and latitude. Schlax et al. (2000) calculated the sampling error in such a manner as to allow for a completely uniform error distribution implying that local regions may have higher or lower errors in the wind fields. Nonetheless, using this technique to take into account the sampling and potential measurement

errors, their results indicated the QuikScat scatterometer should have a mean error/uncertainty of 1.5 ± 0.7 m/s for a spatial and temporal resolution of 1° and 2 days. For a spatial and temporal resolution of 2 degrees and 4 days, the mean error/uncertainty of the wind would be 1.2 ± 0.5 m/s.

Finally, Quikscat scatterometer wind vector errors are sensitive to the magnitude of the wind speed and rain rates. That is the higher the wind speed and/or rain rates, the greater the error. The error produced by these effects can lead to a substantial overestimate of the actual wind speed (Weissman, et al., 2002). One way to alleviate this problem is to use a software algorithm to "flag" data where rain has been detected (Bourassa et al., 2003). By using rain flags, rain contaminated data is removed resulting in much smaller wind vector errors. However, the algorithms are not perfect and sometimes data that originally is rain-free is removed by mistake; even when the algorithm works perfectly, there is always the fact that some amount of data is removed due to rain. Therefore, using scatterometer data in convectively active regions always means there is some uncertainty due to the smoothing of the data. However the alternative to scatterometer data is to use spatially averaged ship data which has a much coarser spatial and temporal resolution or to use model re-analysis, the limitations of which have already been discussed in the previous section. In spite of unavoidable uncertainties, I believe the use of scatterometer data in combination other observational and model re-analysis data-sets should be more than adequate for this study.

For my research project, I used gridded Quickscat near surface wind fields provided by the Center of Oceanic and Atmospheric Prediction Studies at Florida State University. The rain contaminated observations were removed using a standard rain flag (Bourassa, personal communication, 2002); data were "gridded" using a method similar to that described in Pegion et

al (2000). The dataset contains zonal and meridional pseudo-stress fields that are mathematically described by the following:

$$u^*=Uu \quad \text{and} \quad v^*=Uv \tag{1}$$

where 'u*' and 'v*' are the zonal and meridional component of the pseudo-stress fields, 'u' and 'v' the zonal and meridional component of the wind fields and 'U' the wind speed magnitude. Using simple algebra, the magnitude of the wind speed can be found using the relationship:

$$U=(u^{*2}+v^{*2})^{1/4} \tag{2}$$

From this, I determine the zonal and meridional wind components using the relations:

$$u=u^*/U \qquad v=v^*/U \tag{3}$$

The data-set is ideal for examining phenomenon with spatial scales ≥ 400km and time scales ≥ 3 days although careful use on a daily time scale is possible on a case by case basis (Mark Bourassa, personal correspondence, 2002). For quality control, samples of gridded winds were subjectively compared with raw scatterometer and low-cloud track wind data and found to agree very well. The data's spatial resolution is available in 1° x 1° grids on a global scale at six-hour time steps. For my study, I averaged the six-hourly data to create one day time steps.

Satellite Derived SST Data

Satellite sensors have also provided much information about the temperature of the ocean's surface. Ships were the chief means for acquiring SST measurements until satellite technology made the tracking and reporting of drifting and moored buoys feasible (Emery, et al. 2001). In the middle 1970s, researchers developed ways of calculating SSTs using the satellite-observed infrared radiation passively emitted by the sea surface. However, at these wavelengths there is substantial attenuation by atmospheric water vapor. Cloud cover between the satellite and the sea surface would absorb infrared radiation to such an extent that prevents any useful SST retrievals (Wentz, et al., 2000). This means a significant amount of data is lost over regions of

persistent cloud cover, such as the ITCZ and the SPCZ. Microwave radiometers offer a way around this problem. As Wentz et al. (2000) report: "at frequencies below about 12GHz, the surface radiance is proportional to SST and microwaves penetrate clouds with little attenuation, giving a clear view of the sea surface under all weather conditions except rain." The TRMM satellite's microwave radiometer (TMI) has a 10.7 GHz channel making it extremely useful for measuring SST in regions of persistent cloud cover. Comparisons with buoy data indicated the SST measurements were adequately accurate with a root mean square difference ranging from 0.5 to 0.7°C. Additionally, the 759 km wide swath of the TMI sensor and the low inclination orbit enabled full coverage of the global tropics every three-days (Kummerow et al., 1998).

There are, however, some disadvantages using this data. Spatial resolution is rather coarse (about 50 km) and complete global coverage occurs approximately every three days (Wentz et al., 2000). Another disadvantage is the significant attenuation and scattering of microwave radiation by raindrops. This has the affect of preventing the satellite from sensing the microwave radiation upwelling from the ocean's surface. Therefore, regions that have persistent rain, such as the ITCZ and parts of the SPCZ, have the potential for a number of data-drops. However, the total area of cloud cover is more than the total area of clouds bearing rain meaning more data would be loss using infrared techniques to determine SSTs than would be using the microwave technique.

This does not mean there aren't gaps caused by rain in the TMI derived SST field; on the contrary, figure 4 (top picture) shows that three day averages of SSTs still contain gaps in the SST data. A smoothing algorithm was used to replace data gaps by averaging values surrounding a gap. The width of the averaging "window" was chosen to be five gridpoints and all of the surrounding points were weighted equally. If any of the surrounding gridpoints

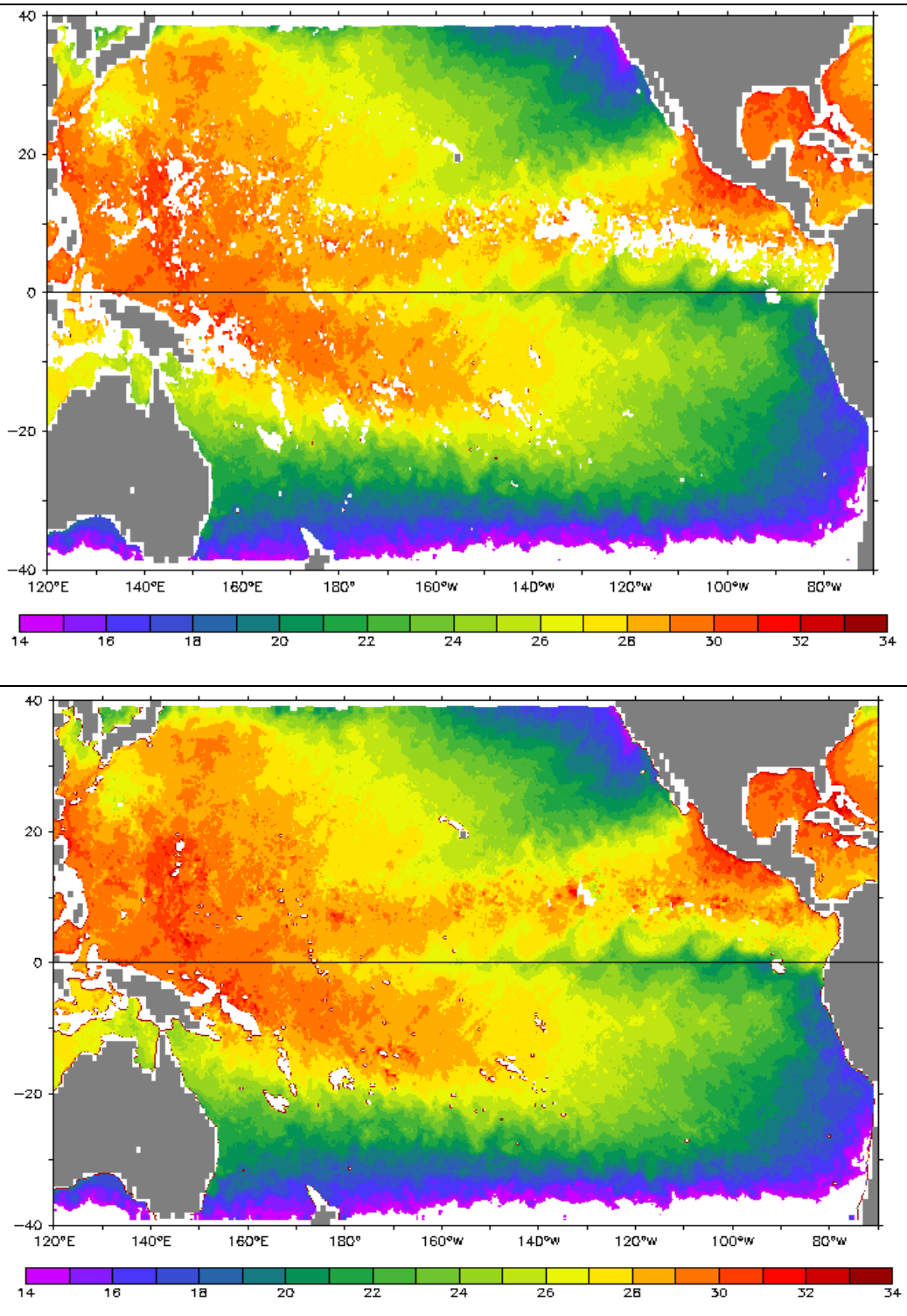

Figure 4: Three day average of SSTs calculated without smoothing (top) and with smoothing (bottom).

contained data gaps as well, they were omitted from the average; if every surrounding gridpoint didn't have a value, an average was not made. The drawback to this is the smoothing of any small scale features that may be present. However, I am interested in examining SSTs on seasonal time scales and this will not affect my research goals. The bottom of figure 4 shows the results after using the smoothing algorithm. Only a few spots have not been filled and these are due to islands.

Satellite Derived Rain Rates

Over the past thirty years, satellite estimated rainfall has played an increasingly important role in research. The reason is obvious: it is much harder to create a rain gauge network over water, via instrumented ships and buoys, than over land. Despite an assortment of research ships and buoys, there is nowhere near enough to provide a network of rainfall observations over the remote oceans nor would it be economically feasible to create one. Therefore, remote sensing is an extremely practical resource for estimating rainfall over the oceans.

How can satellite data be used to create rain rate estimates? One way is through the interaction of microwaves with rain drops. In the atmosphere, typical cloud droplets have radii of 10 μm while raindrops have radii of around 1000 μm. The wavelength of microwave radiation is on the order of 1cm or 10^4 μm so it interacts weakly (scattered) with cloud droplets and small, widely scattered ice particles such as found in cirrus clouds. Therefore, non-raining clouds are virtually transparent to microwave radiation at frequencies of 19.35 GHz (1.55cm wavelength). On the other hand, microwave radiation will interact substantially with raindrops and graupel particles (Wallace and Hobbs, 1977) as well as water vapor and molecular oxygen (Wilheit et al., 1977). Figure 5 roughly illustrates what happens when microwave radiation passes through the atmosphere. Ignoring scattering effects, cosmic background microwave

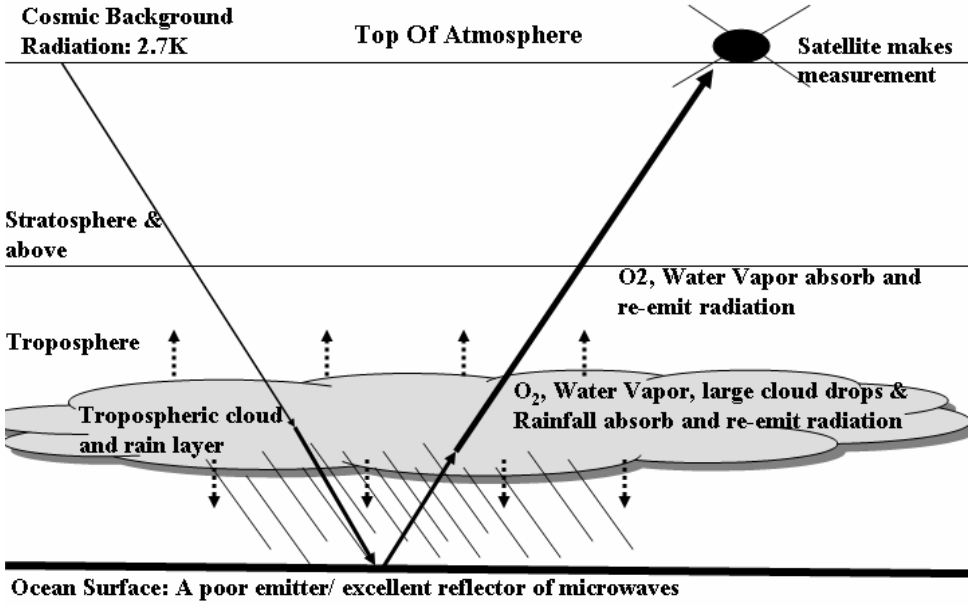

Figure 5: Schematic of what happens to microwave radiation as it passes through the atmosphere, reflects off the ocean and back into space. Thin solid arrows represent radiation originating from space; arrows thickening in size represent the increase in radiation due to absorbtion and re-emission. Dotted arrows represent microwave radiation emitted by rain, O_2 and water vapor.

radiation generally passes unhindered through the atmosphere until it reaches the troposphere. Here, oxygen and water vapor will absorb some of the radiation and re-emit it in all directions. More absorbtion and re-emission occurs if precipitation bearing clouds are present along the path of the radiation in the troposphere. Once the radiation strikes the ocean surface a large portion of it is reflected back towards space as the ocean surface is a good reflector of microwave radiation. On its path back to space, microwaves encounter more oxygen, water vapor and possibly more rain bearing clouds that will, once again, absorb and re-emit radiation in all directions. A microwave radiometer mounted on a polar orbiting satellite can measure the amount of microwave radiation upwelling from the earth.

How can you relate upwelling radiation to a rainfall estimate? From observations and theory, blackbody radiation and temperature are related via Planck's Law:

$$B = c_1 * \lambda^{-5} / [\exp(c_2/(\lambda T)) - 1] \quad (4)$$

where 'B' is the blackbody radiation, 'c_1' and 'c_2' are constants, 'λ' a specific wavelength and 'T' the layer's temperature. Now for microwave wavelengths $c_2/(\lambda T) << 1$ and, using the approximation Exp $(\lambda T) \cong 1 + \lambda T$, Planck's function can be re-written as:

$$B \cong c_1 * T / (c_2 * \lambda^{-4}) \quad (5)$$

When dealing with microwave wavelengths it is customary to divide the radiance 'B' by $(c_1 * \lambda^4 / c_2)$; the resulting quotient is referred to as the brightness temperature (Kidder & Vonder Haar, 1995):

$$T \cong B * c2 * \lambda^{-4} / c1 \quad (6)$$

From 6 it is easy to see that an increase in radiance from rain bearing clouds, water vapor and molecular oxygen results in an increase in the brightness temperature. In an oceanic region where there is little or no rain, the primary emitters of microwave radiation are water vapor and molecular oxygen. As the ocean surface is a good reflector of microwaves it appears uniformly cold in microwave brightness temperature fields. The warmer brightness temperatures associated with precipitation bearing clouds contrast very well against the ocean's cold brightness temperature background (Wilheit, et al., 1976).

Figure 6 further illustrates the contribution of various radiation sources to the calculated brightness temperature as a function of height. It is important to note that increases in rain rates contribute to brightness temperature increases due to more rain droplets absorbing and re-emitting microwave radiation. Wilheit (1977) took advantage of this physical characteristic to derive, using the radiative transfer equations, a quantitative method for estimating rain rates from

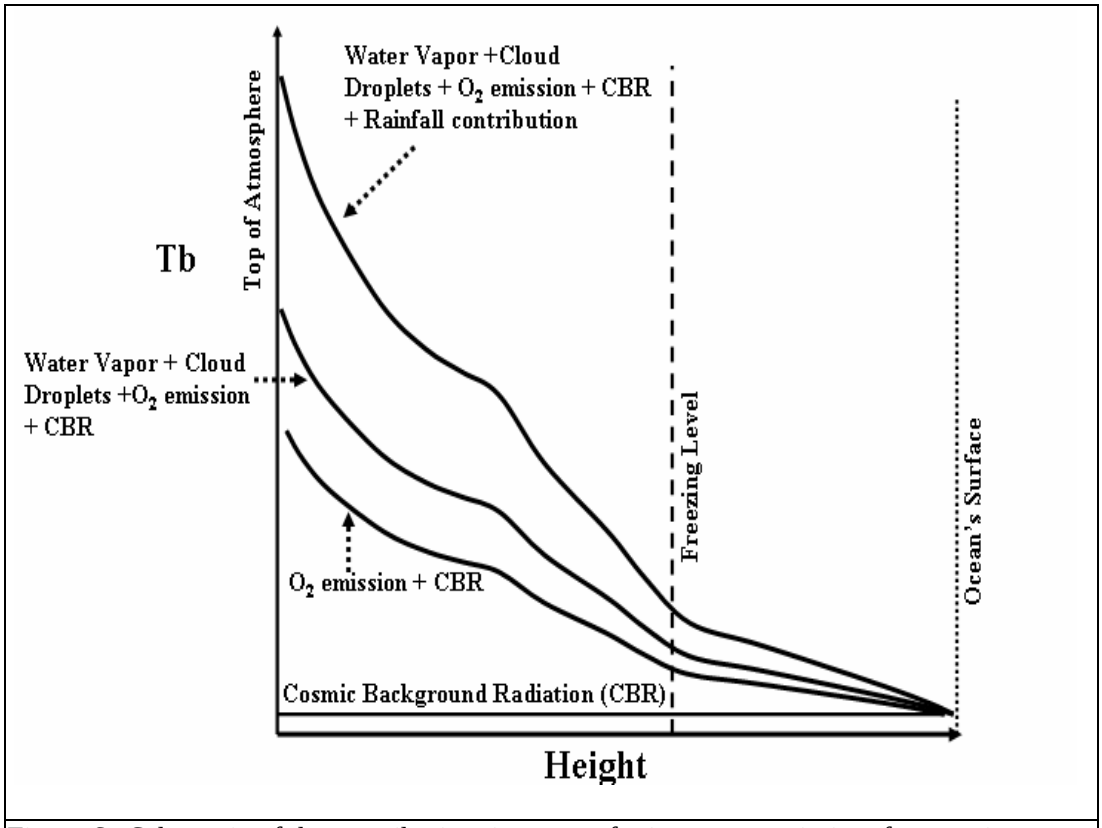

Figure 6: Schematic of the contribution, in terms of microwave emission, from various atmospheric constituents to the microwave derived brightness temperature (Tb). The figure is not drawn to scale.

microwave sensors. The results, when compared with observational data, were good and provided a physically based relationship for measuring rainfall over the oceans. However, a major disadvantage of microwave rain rate estimates is the poor spatial and temporal resolutions, due to the sensors placement on polar orbiting satellites (Huffman, 1997). Therefore other methods of estimating rain were needed for research requiring data with better spatial and temporal scales.

Arkin (1979) and Richards and Arkin (1981) developed an empirical method to estimate rain rates using infrared satellite data. Using GARP Atlantic Tropical Experiment data (GATE), these studies indicated that for area averaged grid boxes the total rainfall was significantly related to the mean fractional area of clouds with averaged equivalent black body temperatures

ranging from 220° to 250° K. As noted in Richards and Arkin (1981), improved correlations with rainfall observations resulted when either the spatial or temporal scales were increased. Arkin and Meisner (1987) showed that cloud tops colder than 235° K area averaged over 2.5° X 2.5° grid boxes showed the strongest relationship with area averaged total rainfall. They used these results to develop a simple technique for estimating precipitation using geo-stationary satellite imagery. The technique showed good agreement with published climatologies over the tropical oceans; however, significant differences could be found over land areas. Although this technique quickly proved useful over the oceanic regions, there is a distinct disadvantage. The physical relationship between infrared radiance and instantaneous surface precipitation is relatively weak. For instance, the rain rate is essentially the fractional amount of clouds colder than 235K multiplied by a constant of 3 mm/hr and the length of time used to determine the fractional cloud cover amount. Essentially, this assumes cold cirrus clouds will provide a rain rate of 3 mm/dy which is a rain rate more typical of stratiform as opposed to convective rain. That is, not all cirrus clouds will have rain associated with them. On the other hand, not all rain bearing clouds are colder than 235K. This is particularly bothersome especially since convection is so dominant in the tropics.

The various advantages/disadvantages of gauge, microwave and infrared precipitation estimates led investigators to try combining the various techniques to obtain a superior product. Adler et al. (1993) developed a method for combining geo-stationary infrared satellite data with 37 and 85 GHz microwave data available on the Defense Meteorological Satellite Program satellite to estimate rainfall. Their results showed when the microwave technique performed well, the combined microwave/infrared monthly total estimates performed better than either the microwave or infrared techniques. Kummerow and Giglio (1995, and henceforth KG95) also combined microwave and infrared satellite data to infer precipitation estimates over ocean and

land areas, except they developed different algorithms. Over ocean areas, the algorithm used 19GHz data to estimate rain rates while over land 85GHz data was used. KG95 investigated several ways to calibrate infrared brightness temperatures with microwave data. The strategy was to obtain co-located infrared and microwave images observed within 90 minutes of each other. The total number of pixels indicating rain and the associated rain rate were calculated using the microwave data. A threshold temperature was derived in the infrared image to match the areal amount of rain as determined by microwave data. Once found, infrared pixels colder than this threshold temperature were considered to contain rain. Rain rates calculated from microwave imagery were assigned to the raining areas in the infrared data. KG95's results showed that the combined technique performed better than either the microwave or infrared techniques when compared to one month of gauge and radar data over land. Using one month of atoll gauge data in the Western Pacific the results were a little surprising: the combined technique was unable to improve upon the infrared technique, presumably because of the poorer spatial and temporal coverage from the microwave radiometers. However, the combined technique did improve upon the microwave estimates.

Huffman et al. (1997) developed a similar algorithm to that of KG95 for combining microwave and infrared imagery to develop rain rate estimates. Once satellite based estimates were created, they were combined with land based rain gauge data to create 2.5° X 2.5° monthly global rain rate estimates. The algorithm incorporated rain gauge data by taking the combined microwave/infrared satellite rain rate estimate over land and multiplying it by the ratio of the area averaged gauge to satellite estimates. Qualitative analysis showed general agreement with prior global precipitation studies although systematic differences were noted on regional scales. Comparisons with an independently derived gauge data-set showed the combined date-set performed better than the gauge or satellite estimates alone. The spatial and temporal resolution

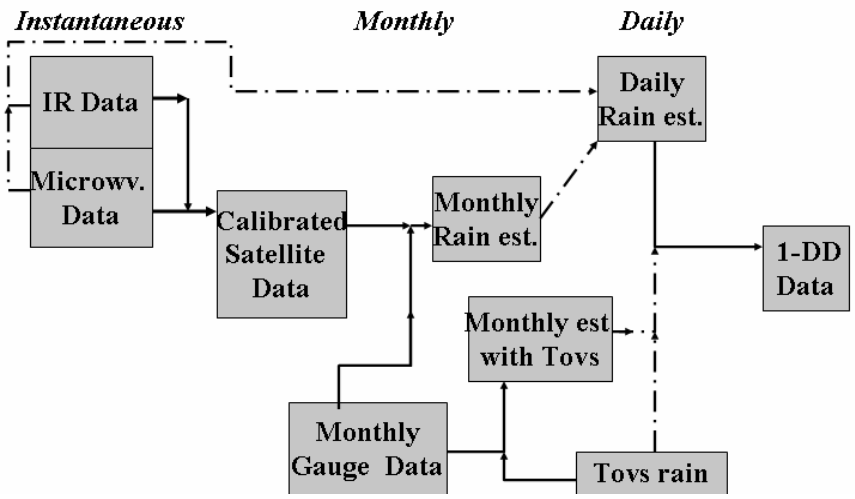

Figure 7: Schematic of the algorithm used to create GPCP rain rate data. Adapted from Huffman, et al (2001).

of the data set is 1° x °1 spatial at one day time steps (Huffman et al. (1997); Huffman et al. (2001)). The steps used to create this product are approximately illustrated in figure 7. First, all co-located and contemporaneous microwave and infrared imagery were collected and calibrated to get monthly rain totals. The calibration was applied to the entire infrared data-set and the resulting rain rates were calibrated with available rain gauge data as prescribed by Huffman et al. (1997). Next, daily microwave and infrared imagery were used to determine brightness temperature thresholds for rain and non-raining areas using daily data. Once accomplished, the task was to ensure the daily rainfall totals, when summed for each month, added up to those found in the monthly rain data; if not a correction factor was applied. This process was completed for the infrared data within 40°S and 40°N; poleward of this latitude the infrared technique for estimating rain rates is deficient in distinguishing between deep convection and non-raining cirrus clouds. Therefore, precipitation estimates from the TIROS Operational Vertical Sounding (TOVS) data (Susskind, et al., 1997) were incorporated into the data-set for higher latitudes. Verification studies with a land based rain gauge network showed estimated

and observed rain rates were well correlated on daily time scales, although absolute errors, at times, could be rather high. As with the infrared technique alone, absolute errors decreased when data was averaged over larger spatial and time scales. Using rain gauge data from the Pacific atoll regions, monthly GPCP data had a 15 percent low bias. Although a full statistical calculation of the uncertainty is not yet complete, it is expected the daily data will have the same bias due to the nature of the processing algorithm (Huffman, oral communciation, 2002).

Using these data sets I examined the SPCZ. The NCEP Re-analysis, TRMM SST and GPCP rain rate data were collected for the period of 1 September 1998 to 31 August 2001, a time where either La Nina or neutral conditions existed in the Pacific Ocean. The scatterometer wind fields were used for the period 1 September 1999 to 31 August 2001, the only time when this data was available. Nonetheless, these data-sets, when combined together, enabled a thorough examination of the horizontal and vertical structure of the SPCZ.

Data Set Distributions

I now show some sample data distributions for the NCEP re-analysis and the GPCP rain rate data-sets. First, I divide the SPCZ into three 10° wide and 15° long test regions that lay across the center of the rain rate maximum as shown in figure 8. These regions are meant to

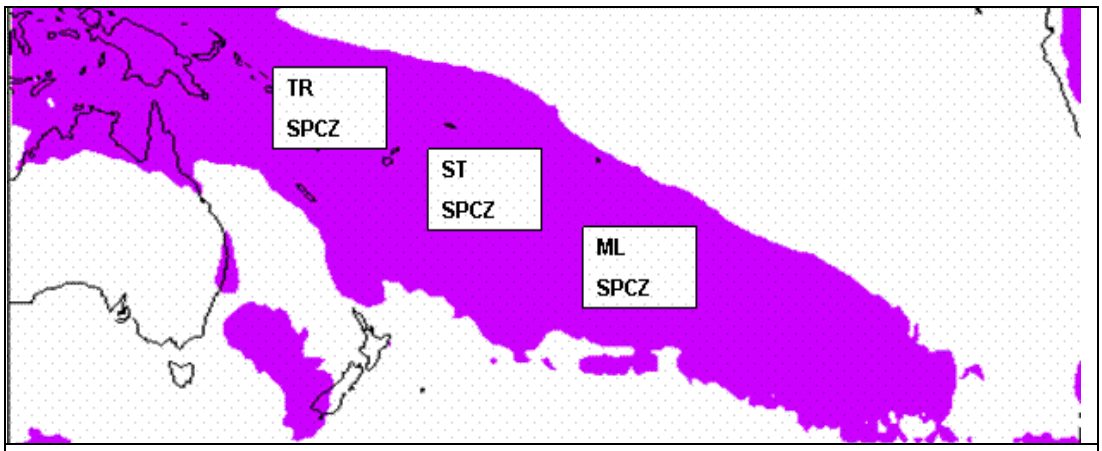

Figure 8: Test regions used for quantitative analysis in chapters III through VI. The purple shade represents the three year average of rain rates ≥ 3mm/dy.

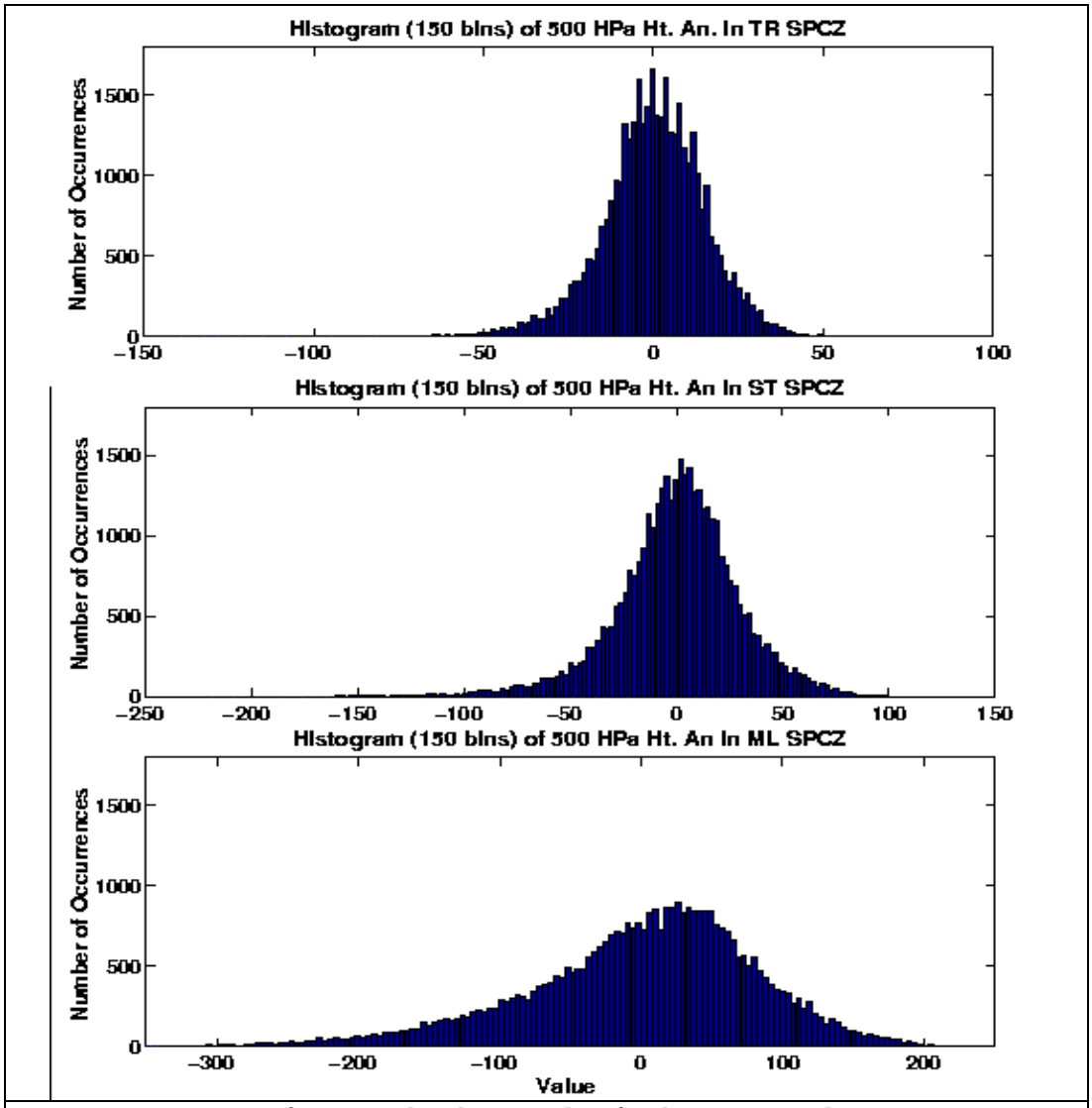

Figure 9: Histograms of 500 HPa height anomalies for the TR, ST and ML SPCZ regions.

approximately delineate the tropical, sub-tropical and mid-latitude sections of the SPCZ. Figure 9 shows histograms for the 500 hPa height anomalies for these SPCZ test regions. Although these distributions are not strictly normal, the deviations from normality are not too large. The histograms for the scatterometer and NCEP winds are similar to those seen in figure 9; that is, the distributions are not far from Guassian. Figure 10 shows the rain rate distribution for the SPCZ test regions. Clearly, the rain rate histograms are highly skewed toward positive

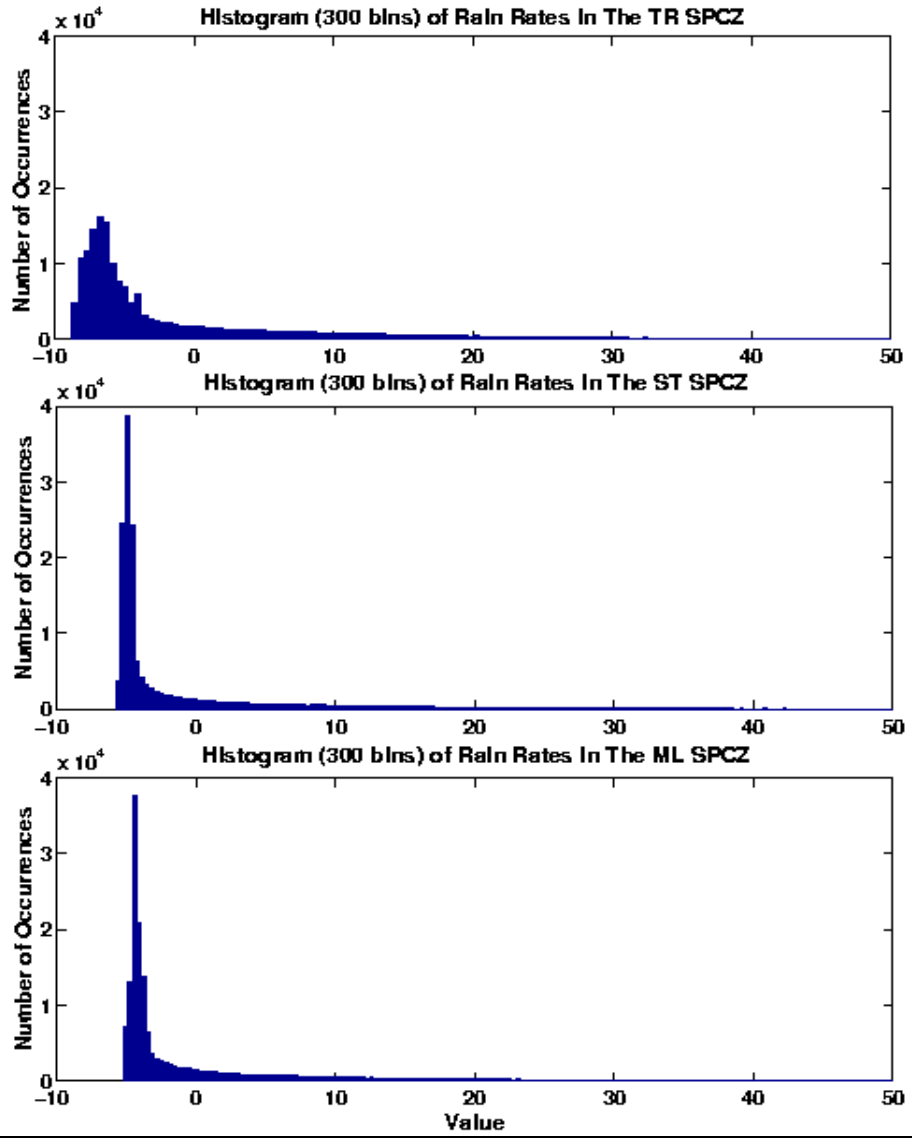

Figure 10: Histograms of rain rate anomalies for the TR, ST and ML SPCZ regions.

anomalies, a common characteristic in precipitation data-sets that is due to the nature of rainfall. That is, there may be a number of days where rainfall does not occur over a given region. When rain develops, rain rates are always positive and can go from a drizzle to a heavy downpour within minutes. Therefore, rain rate distributions are highly non-normal which means determining statistical significance of some results will be quite difficult for the rain rate data.

More on the different quantitative methods used to examine the SPCZ will be discussed in subsequent chapters.

CHAPTER III

ANNUAL DISTRIBUTIONS OF SOME PHYSICAL PARAMETERS IN THE SPCZ

Distribution of Rain Rates and SSTs across the Pacific

Figure 11 shows a three-year average of rain rates and SSTs; clearly visible are rain rate and SST maxima in the Northern Hemisphere Inter-Tropical Convergence Zone (hereafter, NHITCZ) and the SPCZ. The NHITCZ rain rate maximum is zonally oriented, and is narrower in the Eastern and Central Pacific than it is in the Western Pacific. The SPCZ rain rate

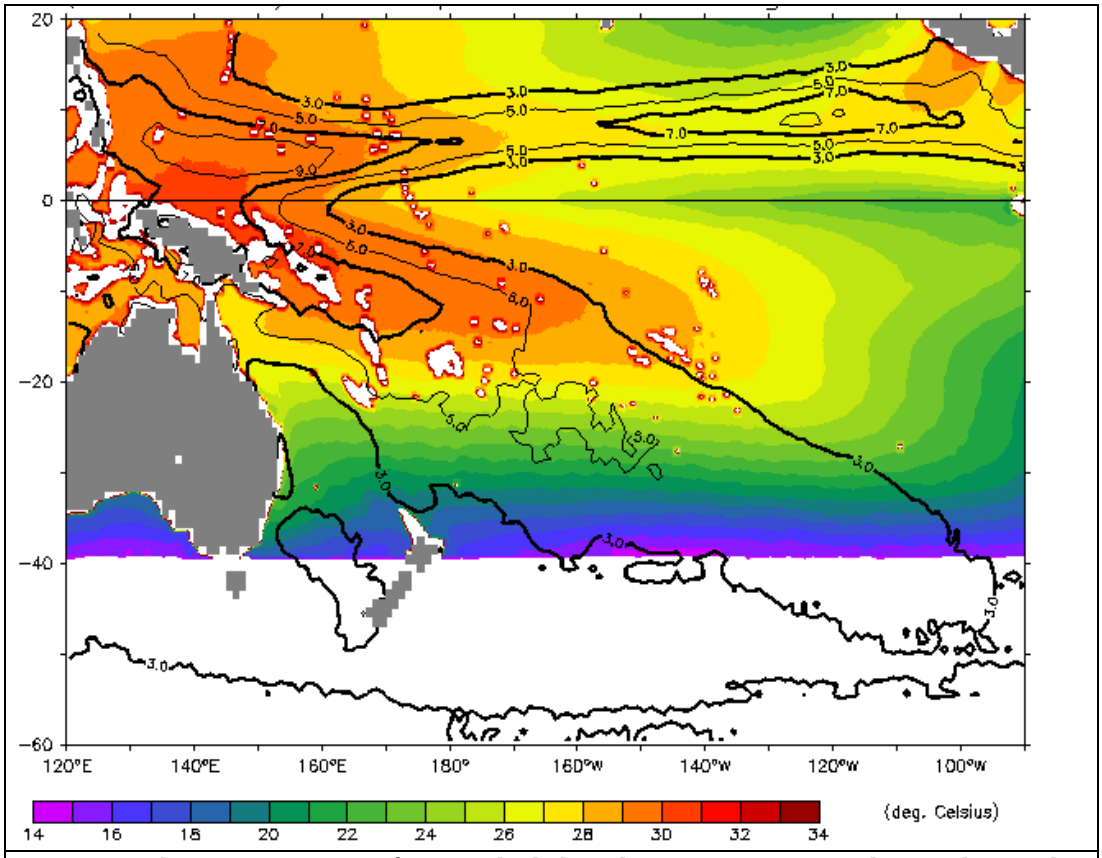

Figure 11: Three year average of SSTs (shaded) and rain rates (contoured) over the South Pacific and the tropical North Pacific. The period of record is 1 September 1998 to 31 August 2001.

maximum has a single diagonal structure stretching from New Guinea southeastward to 45°S 100°W. During the data record (September 1998 to August 2001) there is only a slight suggestion of a zonal structure in the SPCZ rain maximum. This does not mean a zonal structure is never present; Trenberth (1976) noted that the SPCZ exhibits a more zonal structure during El Nino. Data for the 2002-2003 El Nino was not available at the start of this research project, otherwise I would have made a comparison to see if this generalization held true.

In the tropical regions of both hemispheres, the rain rate and SST maxima are closely co-located. This is consistent with the findings of Graham and Barnett (1987); that is, deep convection over large spatial (> 500 to 1000 km) and temporal (> 1 to 2 months) scales is associated with SSTs in excess of 27.5°C. This was not the case for the sub-tropical and mid-latitude portions of the SPCZ, that is, for those regions poleward of ~20°S. As seen in other

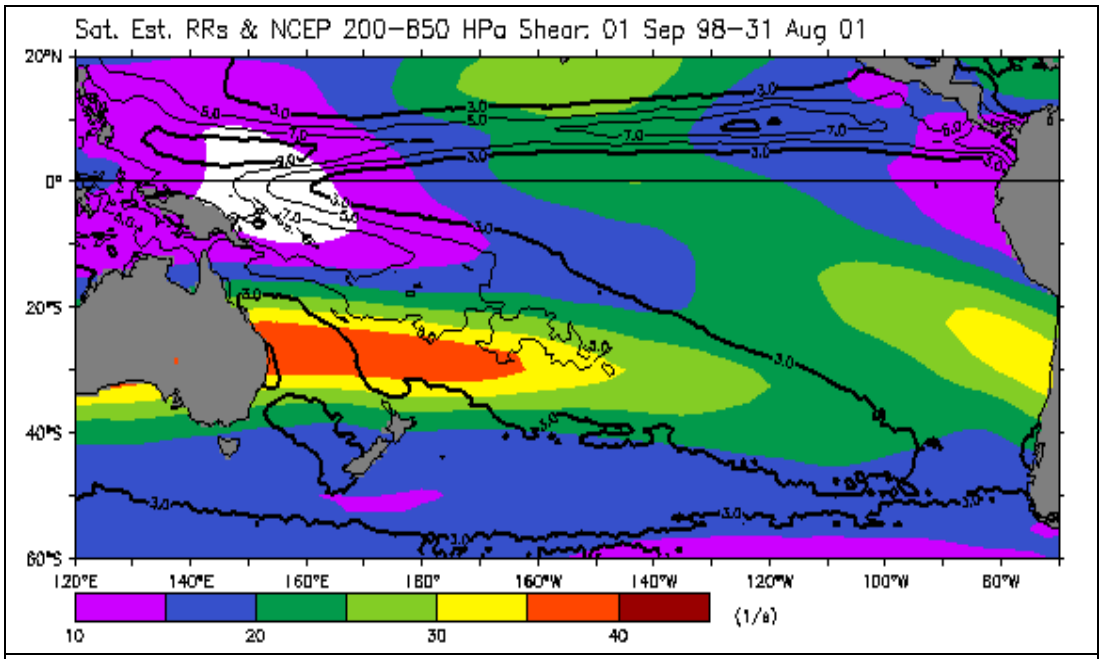

Figure 12: Three year average of 850-200 hPa vertical wind shear (shaded) with rain rates (contoured) over the tropical North and the South Pacific. The period of record is 1 September 1998 to 31 August 2001.

climatological studies (Kiladis et al, 1989; Hurrell et al, 1998; Vincent, 1998), the sub-tropical and mid-latitude portions of the SPCZ rain rate maximum lies across a strong gradient in SSTs. Using NCEP analysis data I calculated the vertical wind shear between 200 and 850 hPa and this is shown in figure 12. A maximum in vertical wind shear is visible across sub-tropical and mid-latitude portions of the SPCZ rain rate maximum and is nearly co-located with the tight SST gradient seen in figure 11. The shear maximum is a reflection of a maximum in the zonal wind at these latitudes (not shown). The position of the zonal jet along the strong low level temperature gradient is consistent with thermal wind balance.

Distribution of Convergence across the Pacific

Figure 13 shows the scatterometer derived wind vectors, convergence and SSTs for a two-year period (zero contours included on both). In general, the convergence maxima are co-locatedwith SST maxima in tropical regions. There are two exceptions to this, both located in the South Pacific. The first exception is located between 150° and 100°W where there is a region of weak convergence that lies above cool SSTs that are part of a strong gradient. The second is located over the equatorial Eastern South Pacific where there is a region of convergence south of the equatorial cold tongue, the strip of cool SSTs along the equator. The relation between the equatorial cold tongue and the convergence/divergence couplet has been studied by Wallace (1989) and Wallace and Mitchell (1992). Another interesting feature in figure 13 is the presence of much higher values of convergence, almost an order of magnitude higher, in the Eastern and Central North Pacific when compared to the Western North and South Pacific. This is a remarkable feature when one recalls from figure 11 that rain rates in the Western North

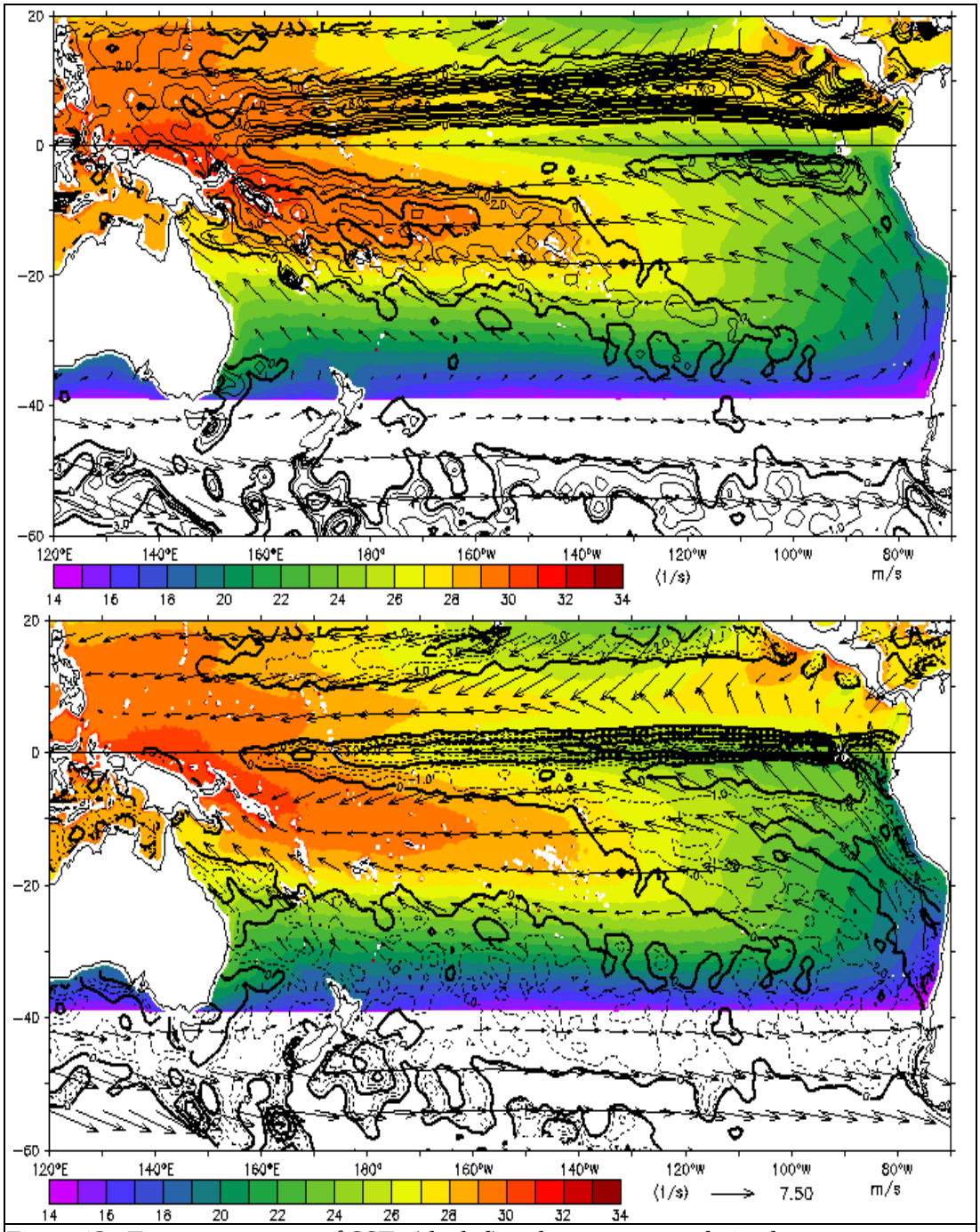

Figure 13: Two year average of SSTs (shaded) and scatterometer derived convergence (top) and divergence (bottom; contoured & in units * 10^6) over the South Pacific and the tropical North Pacific. Wind vectors are plotted as arrows. The period of record is 1 September 1999 to 31 August 2001.

Pacific, Western South Pacific and the Eastern North Pacific are comparable. It is important to note that studies (Gray and Jacobsen, 1977; McBride and Gray, 1980; Mapes and Houze, 1995) have documented that cloud clusters in the tropical Western Pacific are typically associated with a deep layer of convergence, the maximum of which is often not located at the surface. Therefore, I do not draw the conclusion that this convergence pattern is due to substantial error in the scatterometer dataset. The higher convergence values may be a reflection of the stronger surface pressure gradients equatorward of the Northern and Southern Hemisphere sub-tropical highs in the Eastern sections of the Pacific Ocean. Despite the stronger convergence in the Eastern Pacific, there is evidence that the convection there is shallower. Using ECMWF analysis in conjunction with TRMM microwave and radar data, Berg et al. (2002) found cloud depths were deeper in the western North Pacific while shallower, stratiform type rain systems were more common in the Eastern North Pacific during boreal winter.

The distribution of rain rates ≥ 3 mm/dy and surface convergence are shown in figures 14 and the results were surprising. The author expected to find strong low level convergence co-located with the SPCZ rain rate maximum. This was not the case. Instead, a band of weak divergence, values ranging from near zero to $3x10^{-6}$ s^{-1}, is present across much of the sub-tropical and mid-latitude sections of the SPCZ. Overall, the axis of maximum convergence was located equatorward and eastward of the axis of maximum rain rates. This is in contrast to the findings of Kiladis et al (1989) who found the axis of maximum convergence poleward of the axis of maximum SSTs for January climatology. Rain rate and convergence maxima are better co-located west of 170°W, but east of 170°W, the rain rate maximum is displaced 5° to 12° poleward of the surface convergence maximum. The weak, southeastward oriented convergence maximum found between 150°W and 100°W may be evidence of a region where fronts become

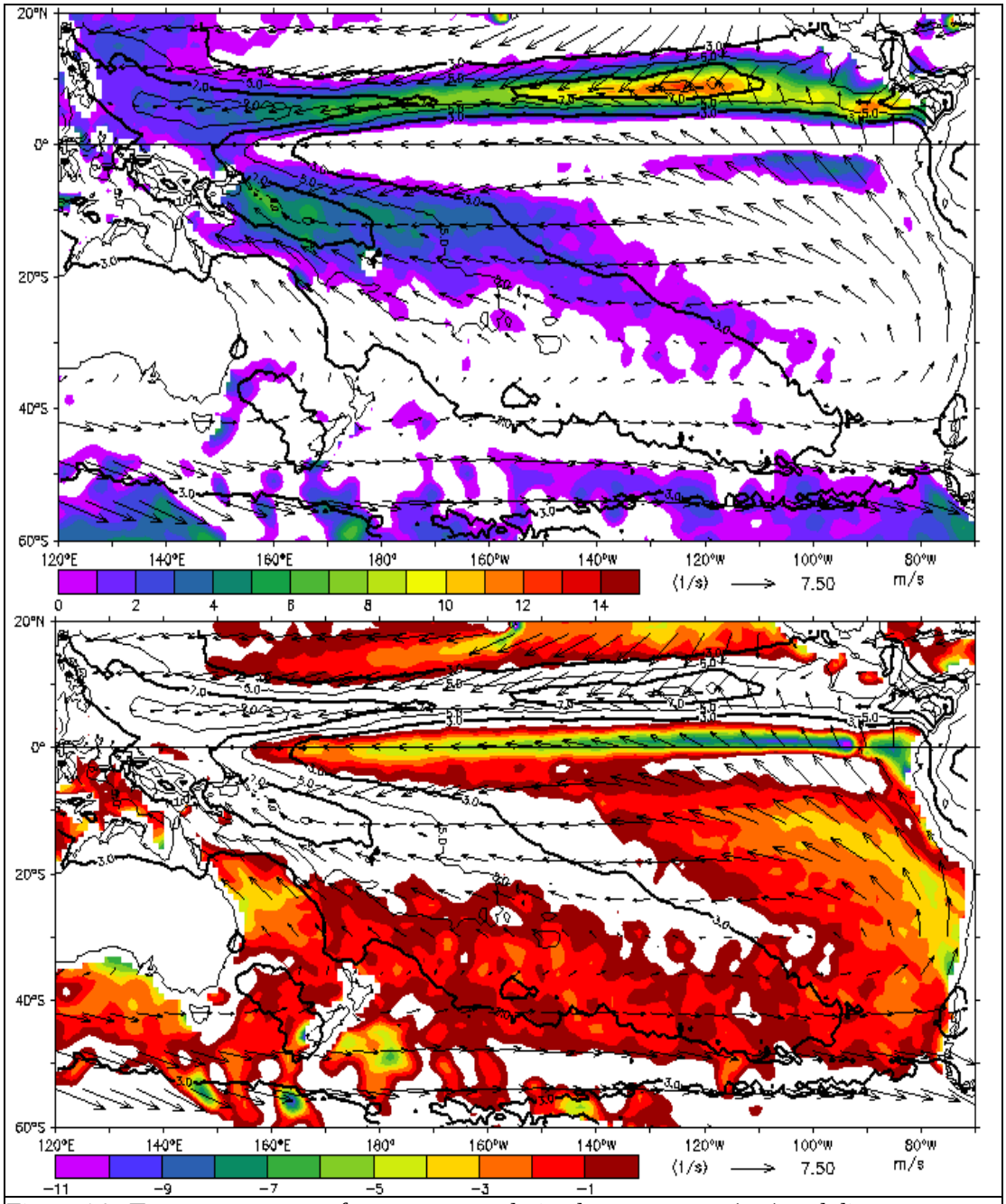

Figure 14: Two year average of scatterometer derived convergence (top) and divergence (bottom; shaded & in units * 10^6) and rain rates (contoured) over the tropical North and the South Pacific. Wind vectors are plotted as arrows. The period of record is 1 September 1999 to 31 August 2001.

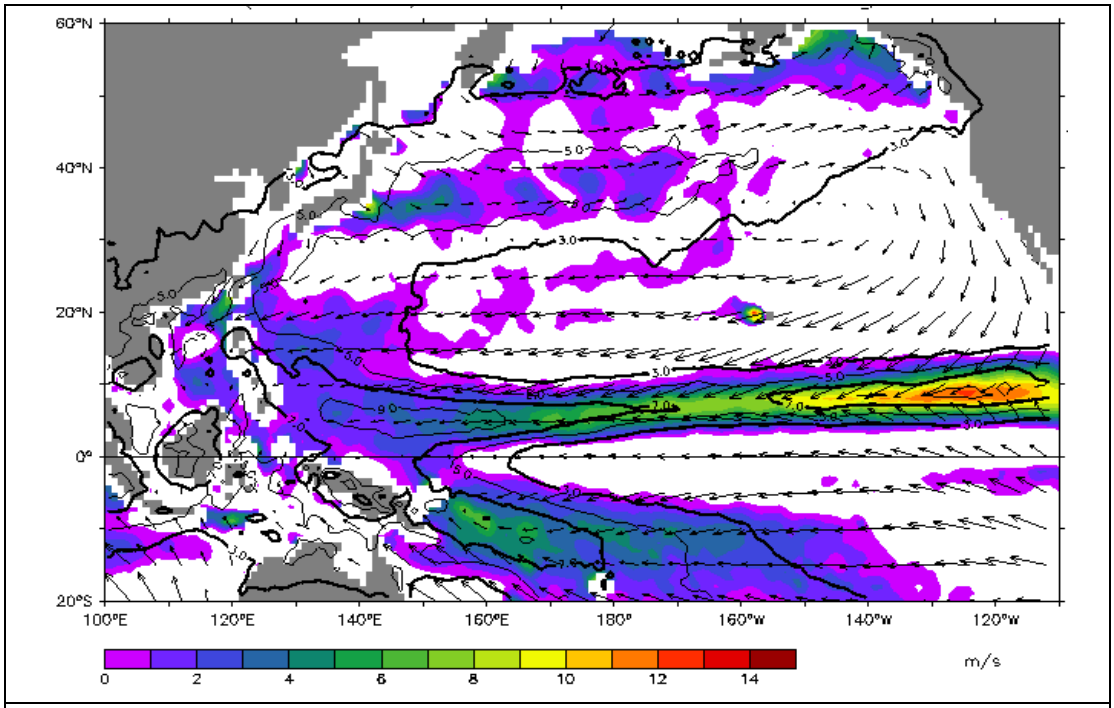

Figure 15: Two year average of scatterometer derived convergence only (shaded & in units * 10^6) and rain rates (contoured) over the tropical South and the North Pacific. Wind vectors are plotted as arrows. The period of record is 1 September 1999 to 31 August 2001.

quasi-stationary then dissipate along the western periphery of the Southeast Pacific High. This idea has been discussed by Trenberth (1976) as well as by Trenberth and Shea (1987); I will discuss this idea later in chapter IV.

To see if a rain rate/convergence pattern similar to that observed in the SPCZ is present elsewhere, convergence and rain rate distributions in the Northwest Pacific were examined and are shown in figure 15. The patterns in the Northwest Pacific are broader making clear relationships harder to pin down. Notwithstanding this, in the tropics the axes of maximum rain rates and convergence are co-located equatorward of 20°N. The rain rate distribution in the sub-tropical and higher latitudes is in the form of a broad west-southwest-to-east-northeast diagonal with a pair of convergence zones straddling the axis of maximum rain rates. These patterns are nowhere as distinct as that seen in the Southern Hemisphere and this may be

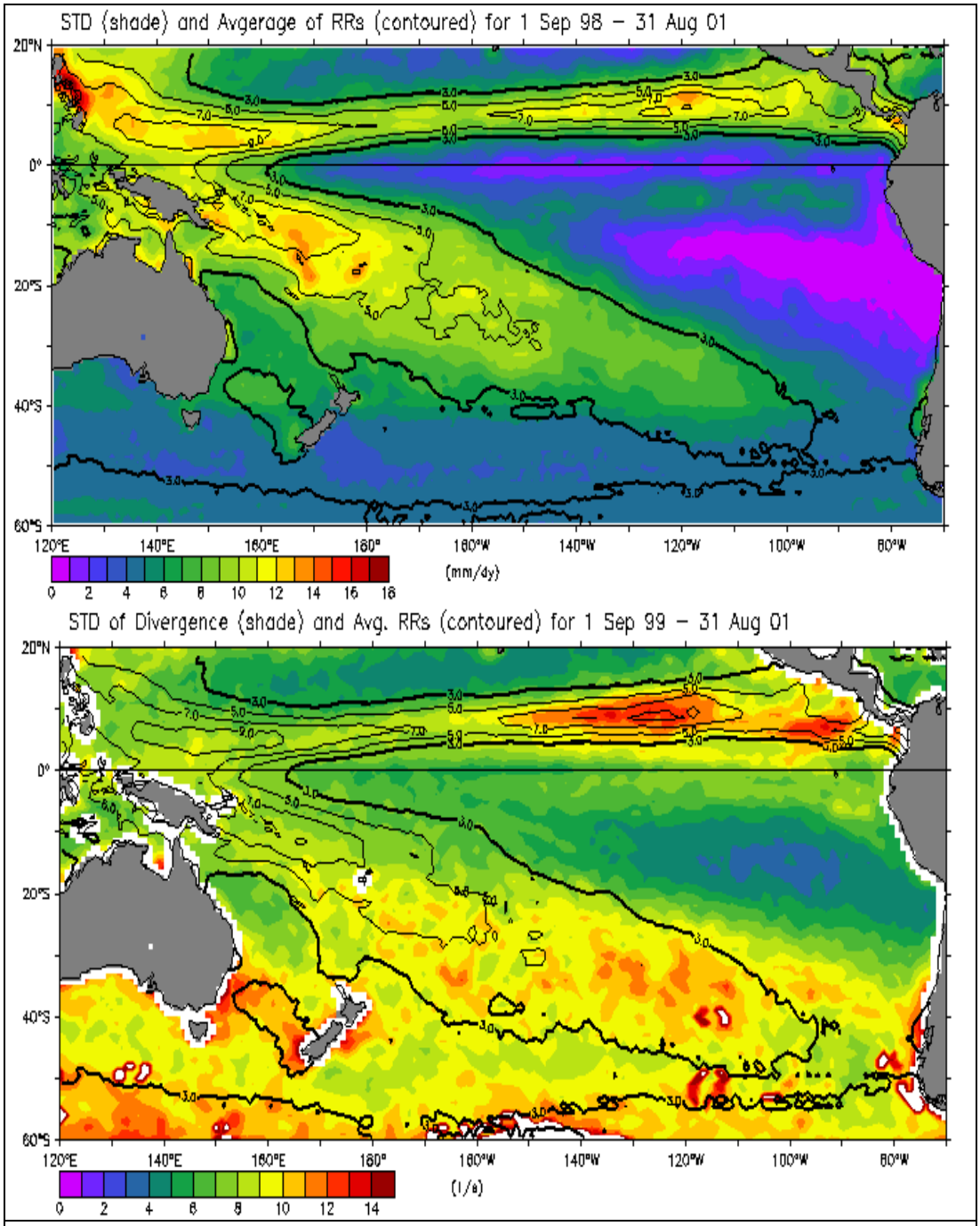

Figure 16: Mean square root and mean of rain rates (top), mean square root of convergence and mean of rain rates (bottom). Convergence in units* 10^6 and values greater than 16 are white.

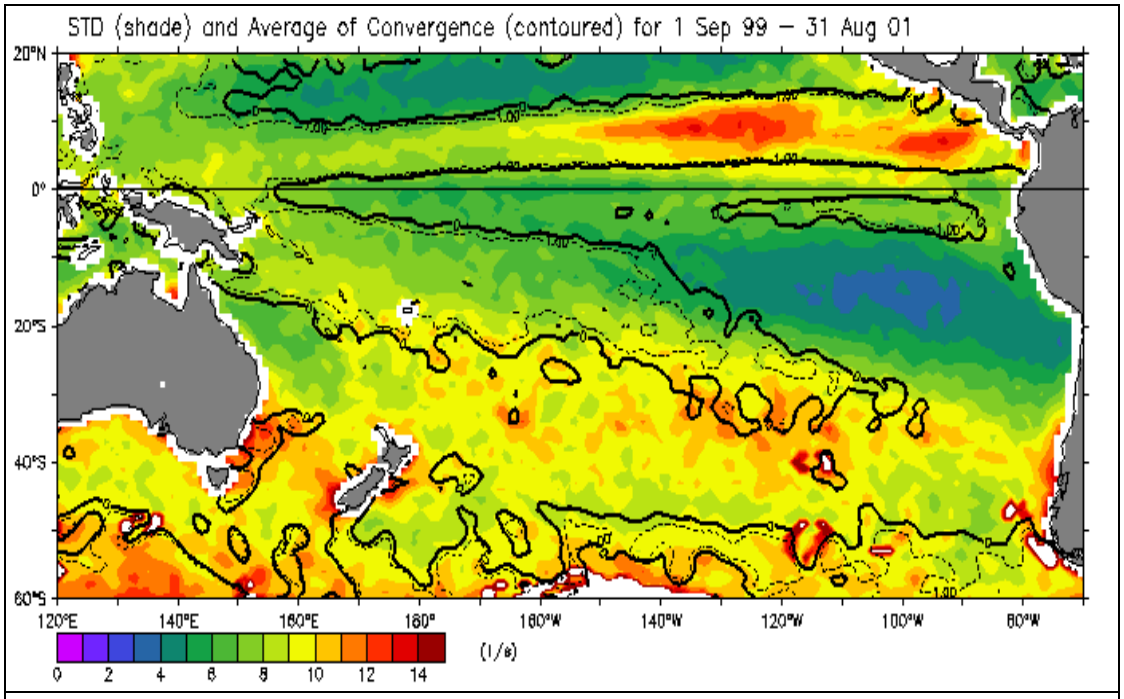

Figure 16 continued: Mean square root and mean of convergence. Convergence in units* 10^6 and values greater than 16 are white.

due to the much stronger seasonal cycle in the Northern Hemisphere, a topic beyond the scope of this study.

To better understand the peculiar rain rate/convergence pattern in the SPCZ region, the variability of the rain rate and convergence fields was examined. Figure 16 shows the root mean square (rms) of the rain rate and convergence (positive and negative values included) fields, with the means superimposed. The highest variability in the rain rates is in the NHITCZ and tropical sections of the SPCZ; variability decreases poleward along the SPCZ rain rate maximum. The convergence variability pattern is quite different from that of the rain rates with lower variability found in the tropical SPCZ and the western NHITCZ regions. Convergence exhibits higher variability in the eastern NHITCZ and over the sub-tropical and mid-latitude sections of the SPCZ. The higher variability over the sub-tropical and mid-latitude SPCZ is co-located with the area of weak surface divergence found in figure 14. An inspection of the convergence variability

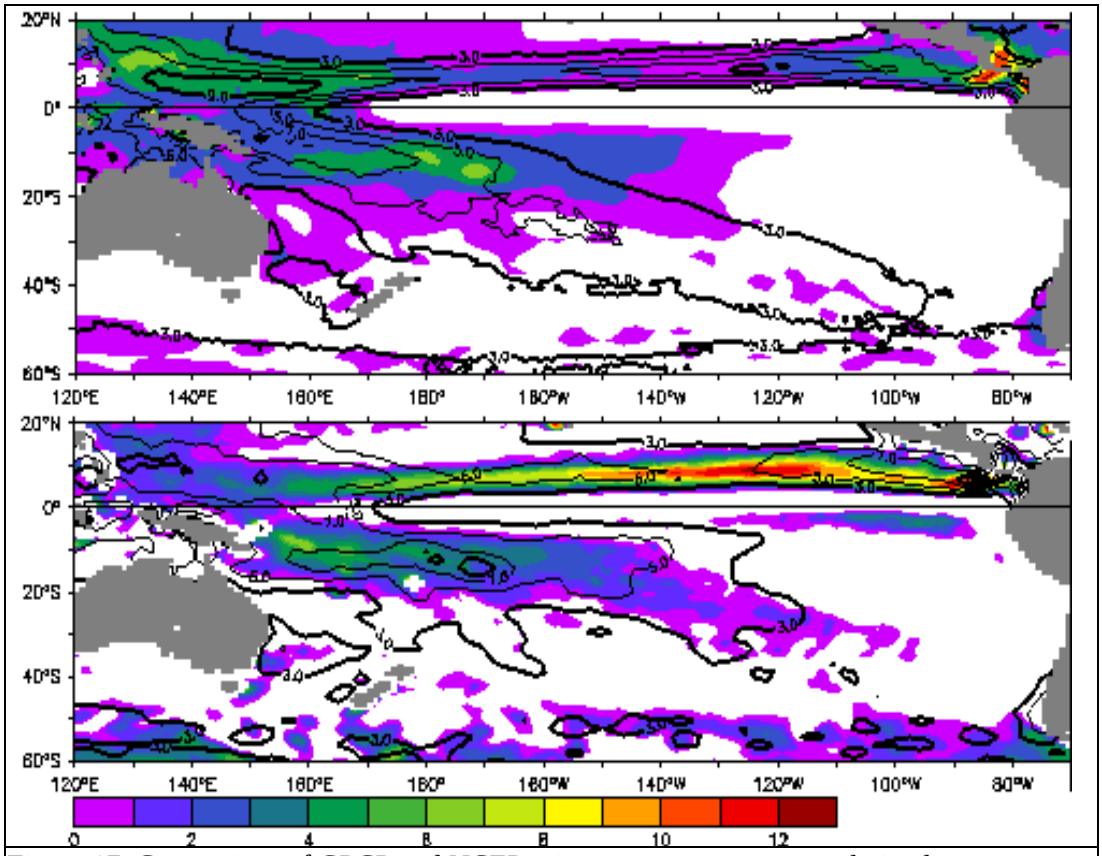

Figure 17: Comparison of GPCP and NCEP rain rates to scatterometer derived convergence (only) as follows: top, a three year average of GPCP (contoured) and NCEP (shade) rain rates; bottom, a two year average of NCEP rain rates (contoured) and convergence (shaded).

in figure 16 and the mean divergence as seen in figure 14 indicate convergence is present at shorter time scales. The convergence variability maxima are equatorward of the mean Southern Hemisphere storm track, located around 50°S (Trenberth, 1991; Sinclair, 1994).

An attempt to further clarify the relation between convergence and rain rates was made by examination of NCEP analysis data. In addition to estimates of surface convergence and rain rates, the NCEP data allow estimates of convergence throughout the atmospheric column. However, prior to this I wanted to compare some of the satellite derived rain rates and surface convergence with the same fields as derived by NCEP re-analysis data. Figure 17 shows a

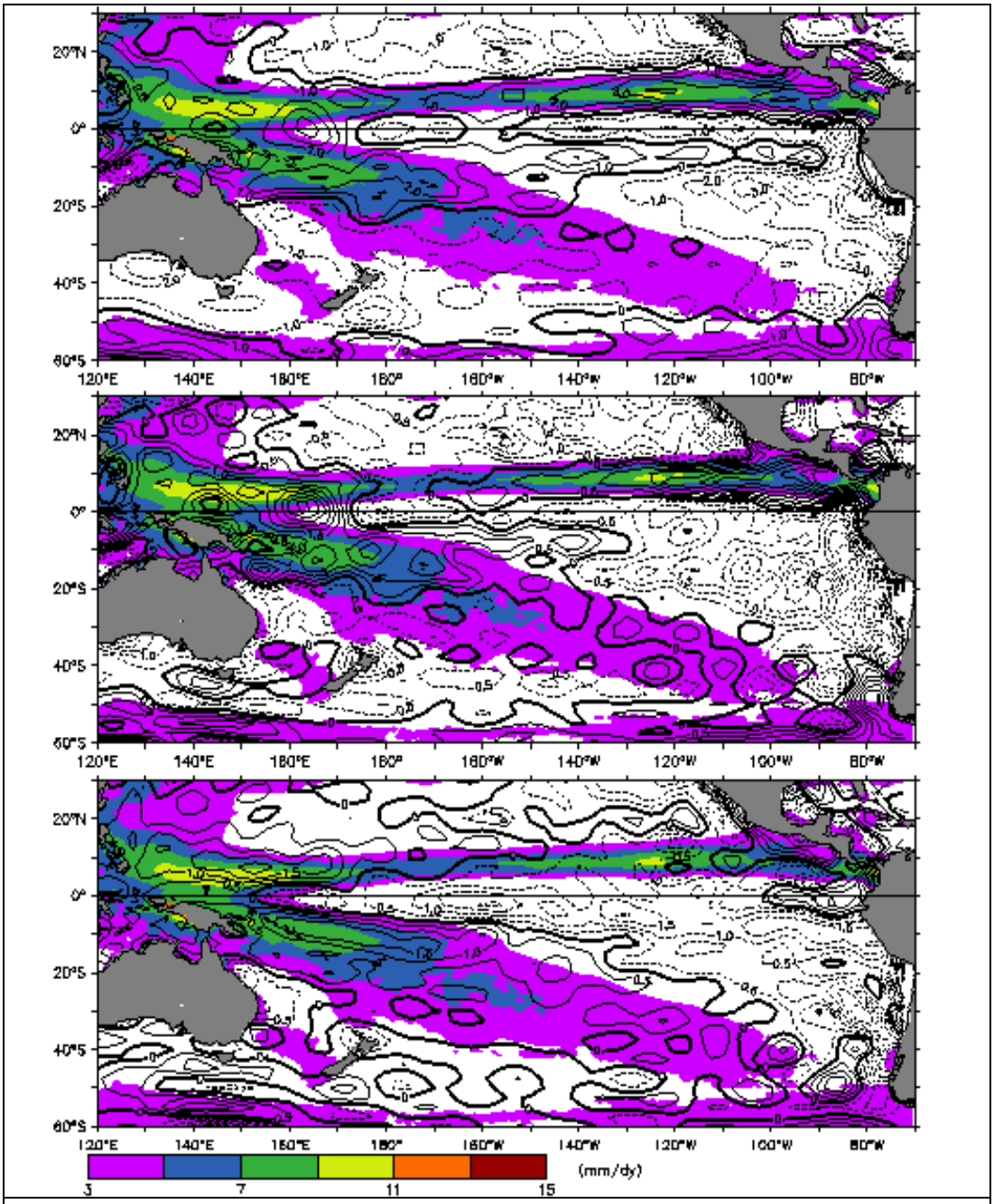

Figure 18: Three year average of GPCP rain rates (shade) and NCEP re-analysis derived convergence (contoured) over the tropical North and the South Pacific. Contour interval for 1000 (top) hPa is every $1*10^{-6}$ s^{-1}; for the 925 (middle) and 850 (bottom) hPa it is $0.5*10^{-6}$ s^{-1}.

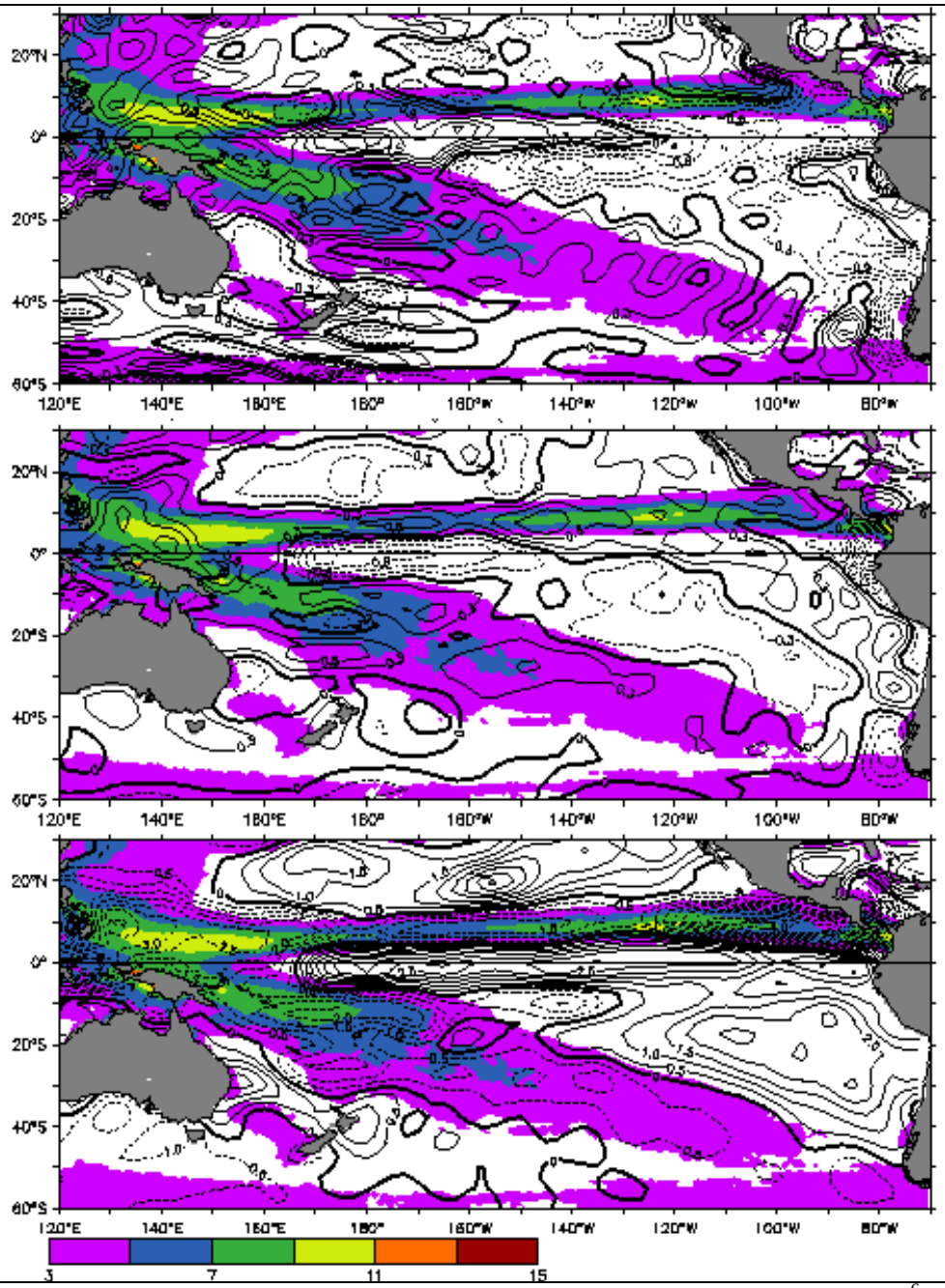

Figure 18 continued: Contour interval for 700 (top) and 500 (middle) hPa is $0.3*10^{-6}$ s^{-1}; for 200 (bottom) hPa it is $0.5*10^{-6}$ s^{-1}.

comparison between satellite derived rain rates and convergence with NCEP rain rates. The axis of maximum rain rates in the NCEP estimates is zonally oriented with rain rates > 3mm/dy

mainly confined to equatorward of 25°S; there is little evidence of the northwestward-to-southeastward oriented rain rate pattern found in the satellite data. On the other hand, NCEP 1000 hPa and satellite derived convergence maxima (not shown) agree well in the South Pacific. Furthermore, the NCEP rain rates appear well correlated with satellite derived surface convergence, which at first appearance seemed surprising.

This result became less puzzling when it was recognized that the NCEP surface convergence, satellite derived convergence and SST fields were all highly correlated in the tropics. The algorithms responsible for precipitation development in the NCEP analysis place maxima above the surface convergence, while satellite observations suggest a different orientation for rain rate maxima in the SPCZ. It is believed that this finding is related to the difficulty climate models have in simulating the proper orientation of the SPCZ, namely how to parameterize convection in a way that accurately depicts precipitation maxima. Kalnay et al. (1996) indicate that a simplified Arakawa-Schubert convective parameterization developed by Pan and Wu (1994) was used to create the NCEP re-analysis precipitation fields. Pan and Wu (1994) noted that the changes in the convective parameterization allowed for "a more realistic precipitation-SST correlation." Unfortunately, very little information was given concerning parameterization changes and their relationship to the SST fields. Therefore the present author is unable to conclude whether the reason for the difference between satellite and NCEP derived rain rates is solely related to the convective parameterization.

If it is assumed that the NCEP winds are more reliable than the NCEP precipitation fields, one may hope to find a convergence pattern in the NCEP data at some higher level which is better co-located with the SPCZ rain rate maxima shown in satellite data. Vertical analysis of satellite derived rain rates and NCEP convergence distributions are shown in figure 18. In a manner very similar to that seen in the scatterometer derived convergence, the NCEP 1000 hPa

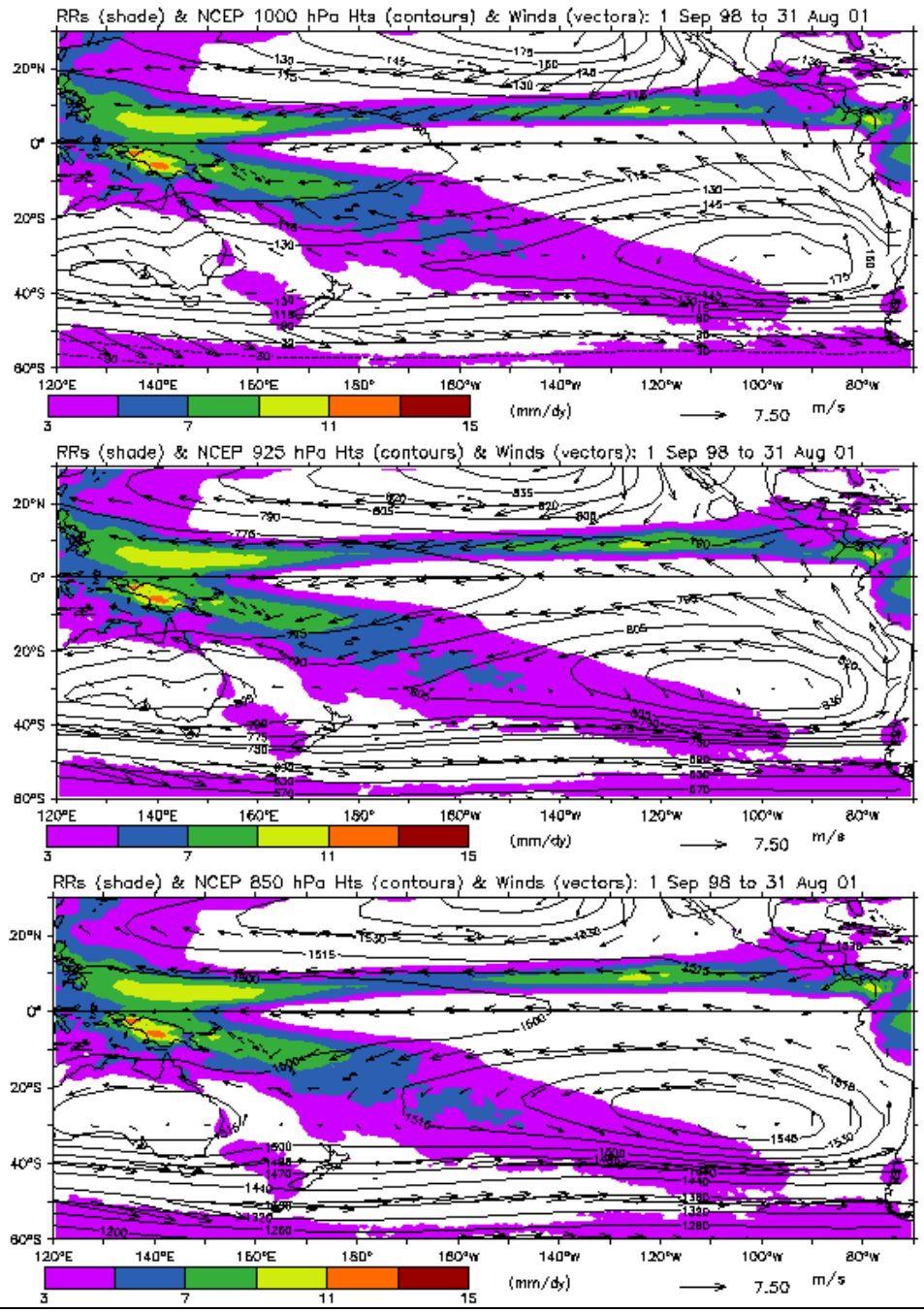

Figure 19: Three year average of GPCP rain rates (shade) and NCEP re-analysis heights (contoured) over the tropical North and the South Pacific. The contour interval is every 20 deca-meters for the 1000 (top), 925 (middle) and 850 (bottom) hPa levels.

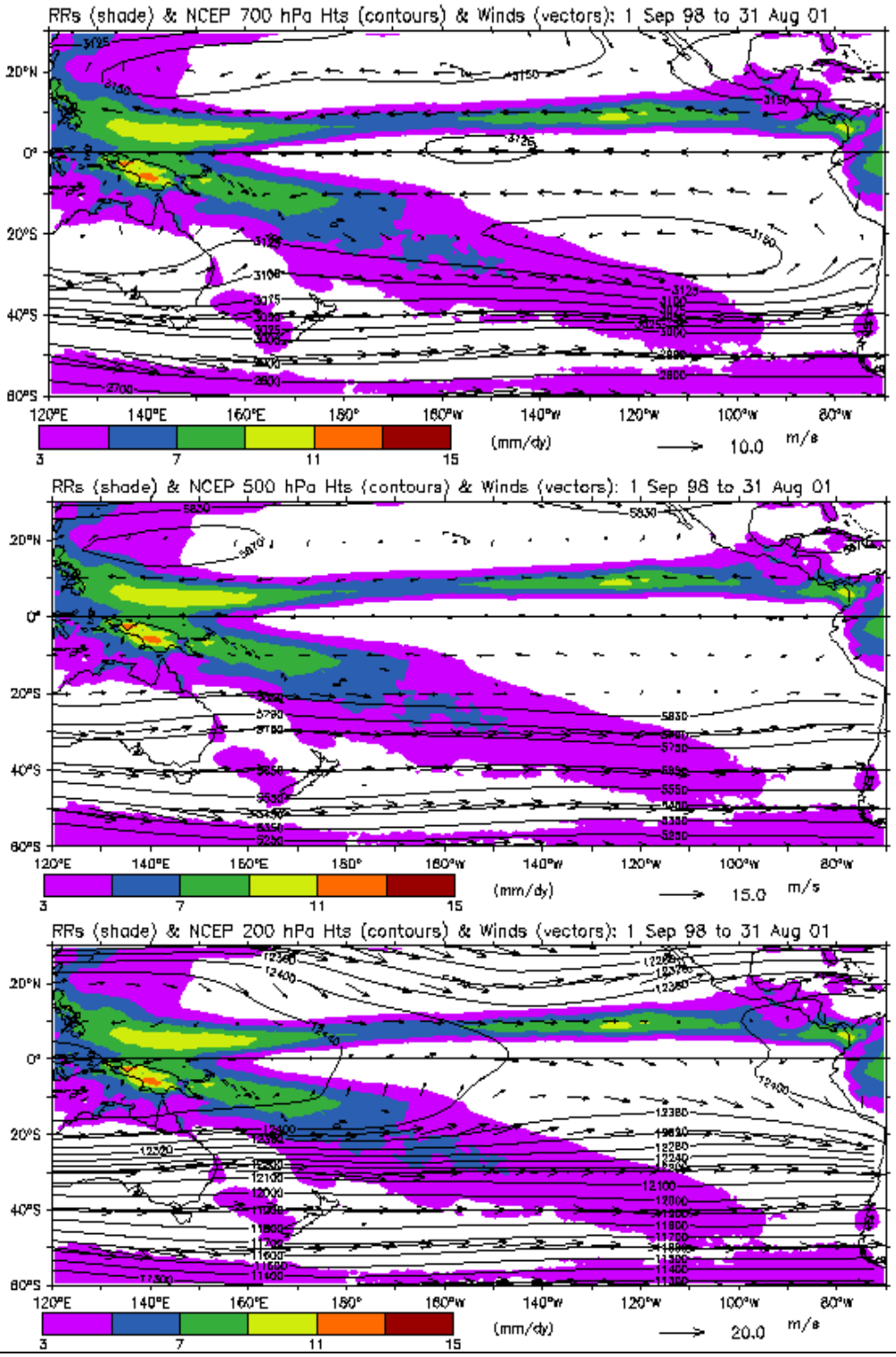

Figure 19 continued: The contour interval for 700 (top) hPa is every 20 deca-meters, 500 (middle) hPa is every 90 deca-meters and every 120 decameters for 200 (bottom) hPa.

level exhibits a zonally oriented convergence pattern with the slight suggestion of a southeastward oriented maximum east of 140°W. Over the sub-tropical and mid-latitude sections of the SPCZ rain rate maximum, divergence (not shown) predominates. Just above the surface region, the magnitude and distribution of convergence changes. More specifically, convergence maxima shift from a zonal orientation at 1000 hPa to a diagonal orientation at 850 hPa. The orientation of the convergence axis at 850 hPa is closely co-located with the satellite observed rain rate maximum although the magnitude is smaller than that observed at 1000 hPa. These results make good physical sense because there must be moisture convergence at some point within the atmospheric column for rain to occur. The same general orientation of the convergence pattern is also evident at 700 and 500 hPa, although the magnitudes decrease with height as the level of non-divergence is approached. At 200hPa, a diagonal like pattern remains except convergence has been displaced by divergence.

The mean height and wind fields are shown in figure 19. Note the strong 1000 hPa pressure gradients equatorward of the sub-tropical highs in the eastern Pacific Ocean. As mentioned previously, the stronger wind flow is likely the reason for the high magnitudes of convergence in eastern and central sections of the NHITCZ. At the 1000 and 850 hPa levels, the sub-tropical ridge axis, although weak in this region, extends across the SPCZ rain rate maximum between latitudes 20° and 40°S. The location of the rain rate and low level height maxima with respect to each other at first glance appears to not make much sense. After all, rainfall is usually associated with the passage of transient low pressure systems, not the passage of high pressure. However, I am only examining dataset means in this chapter; seasonal analysis, to be discussed in chapter IV, will shed more light on this structure. Until then, it should be noted that rain rates are lower in the region poleward of the 1000 hPa ridge axis and higher equatorward of it. Additionally, the rain rate maximum does not lie across the strongest ridging in the South Pacific Basin which is

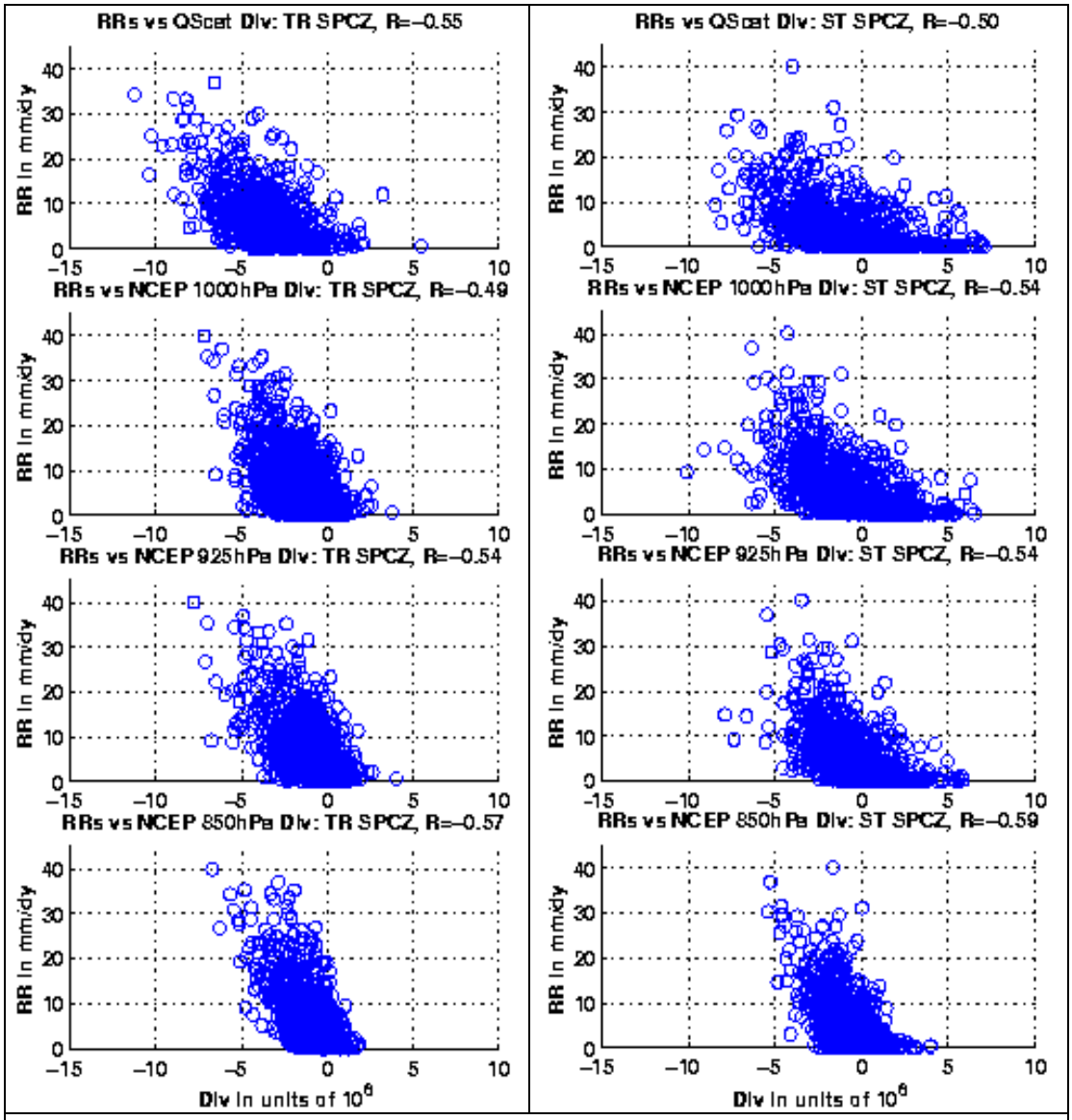

Figure 20: Scatter plots of rain rates and divergence for the surface through 850 hPa layers for the atmosphere: 'TR' denotes tropical, and 'ST' sub-tropical SPCZ. 'R' denotes the correlation coefficient for each plot. The scatter plot using scatterometer data utilizes a two year data record, while the NCEP utilizes a three year data record.

located near 100°W; instead, it lies across a weak ridge axis along the western periphery of the South Pacific High. The ridging across the SPCZ rain rate maximum weakens further with height and gives way to mid-latitude westerly flow at the 700 hPa level. Mid-latitude westerly

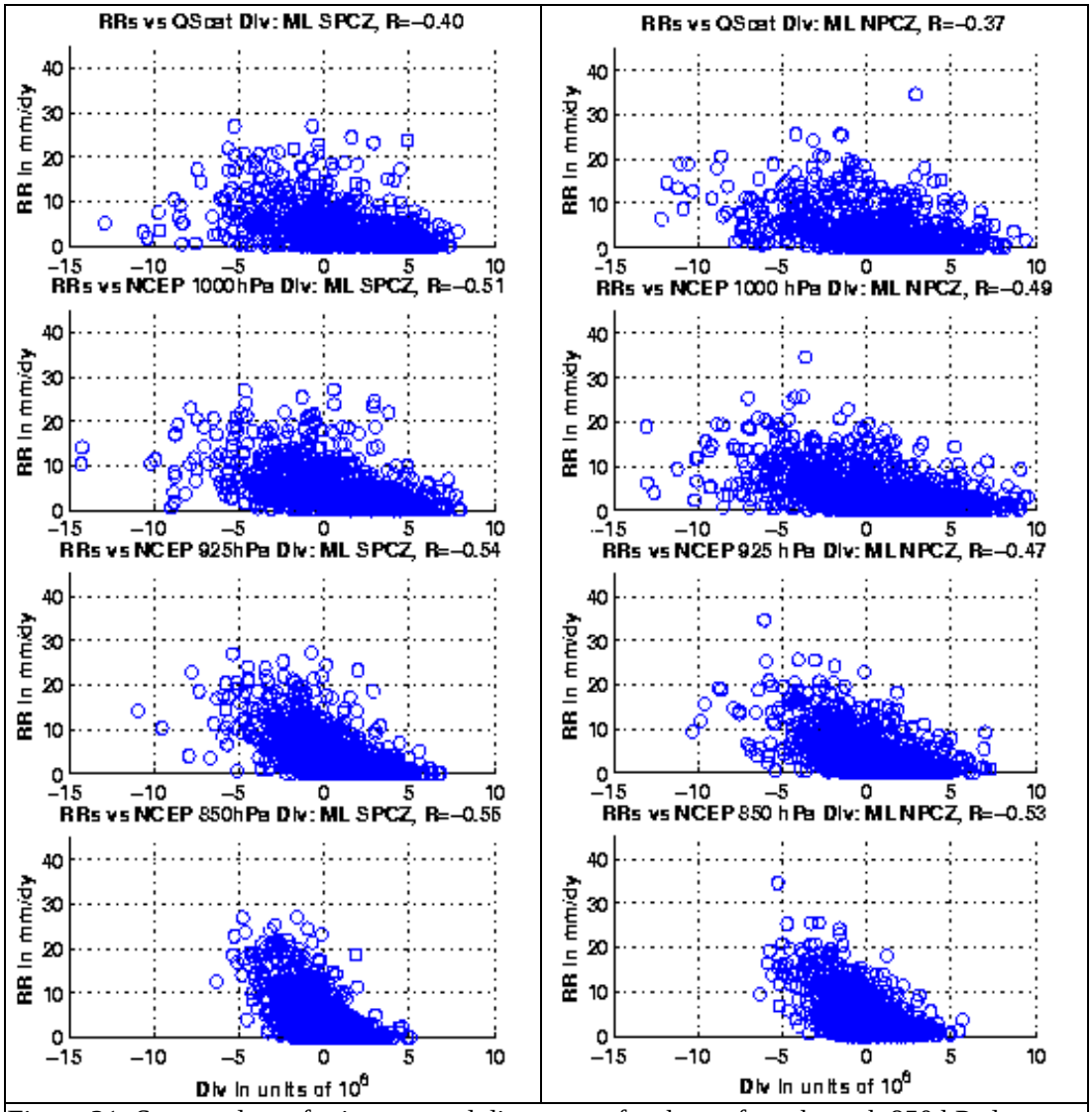

Figure 21: Scatter plots of rain rates and divergence for the surface through 850 hPa layers for the atmosphere: 'ML' denotes mid-latitude SPCZ, and 'NPCZ' a region located within the North Pacific storm track. 'R' denotes the correlation coefficient for each plot. The scatter plot using scatterometer data utilizes a two year data record, while the NCEP utilizes a three year data record.

flow at 500 and 200 hPa completely covers the sub-tropical and mid-latitude portions of the SPCZ; this is not unexpected as this is the same region where a tight SST gradient is present.

Scatter Plots of Rain Rates and Divergence

To further investigate the relationship between rainfall and divergence with height, daily rain rate and divergence data were area averaged over the three SPCZ test regions as discussed in chapter II. Additionally, a comparison was made between the ML SPCZ and a mid-latitude section (30° to 40°N; 150° to 165°E) of the North Pacific storm track. For each region, an average time series of rain rates and divergence was created. Scatter plots of this data for the surface, 1000, 925 and 850 hPa levels are shown in figures 20 and 21. Note that the surface convergence is satellite derived therefore there is only a two year record available. In the TR SPCZ, it is clear that surface through 850 hPa convergence is present for almost all the days that rain is present. It is also apparent satellite derived convergence has higher magnitudes than that observed in the NCEP 1000 hPa convergence. For the NCEP data, the relationship between rain rates and divergence improves with height in the boundary layer.

Over the ST SPCZ, the surface through 925 hPa layer exhibited a number of days where rain and divergence is present; this number decreases substantially at the 850 hPa level. For days where the averaged rain rate for the region was relatively high (> 10 mm/dy) convergence is present from the surface to 850 hPa. This suggests that deep convection, fed by moisture convergence near the surface, is mostly responsible for heavy rainfall days. A mixture of stratiform and elevated convective rain is likely the reason for the days where rain rates and divergence are present at the surface through 925 hPa layers. Further examination of this idea will be discussed in chapter IV.

The number of days where rain and divergence is present increases substantially over the ML SPCZ. In fact, the scatterometer data indicates a rather poor relationship between rain rates and divergence; the relationship is not that much better for the NCEP 1000 hPa level as a large number of days with rain occurred when divergence was present. The relationship between rain

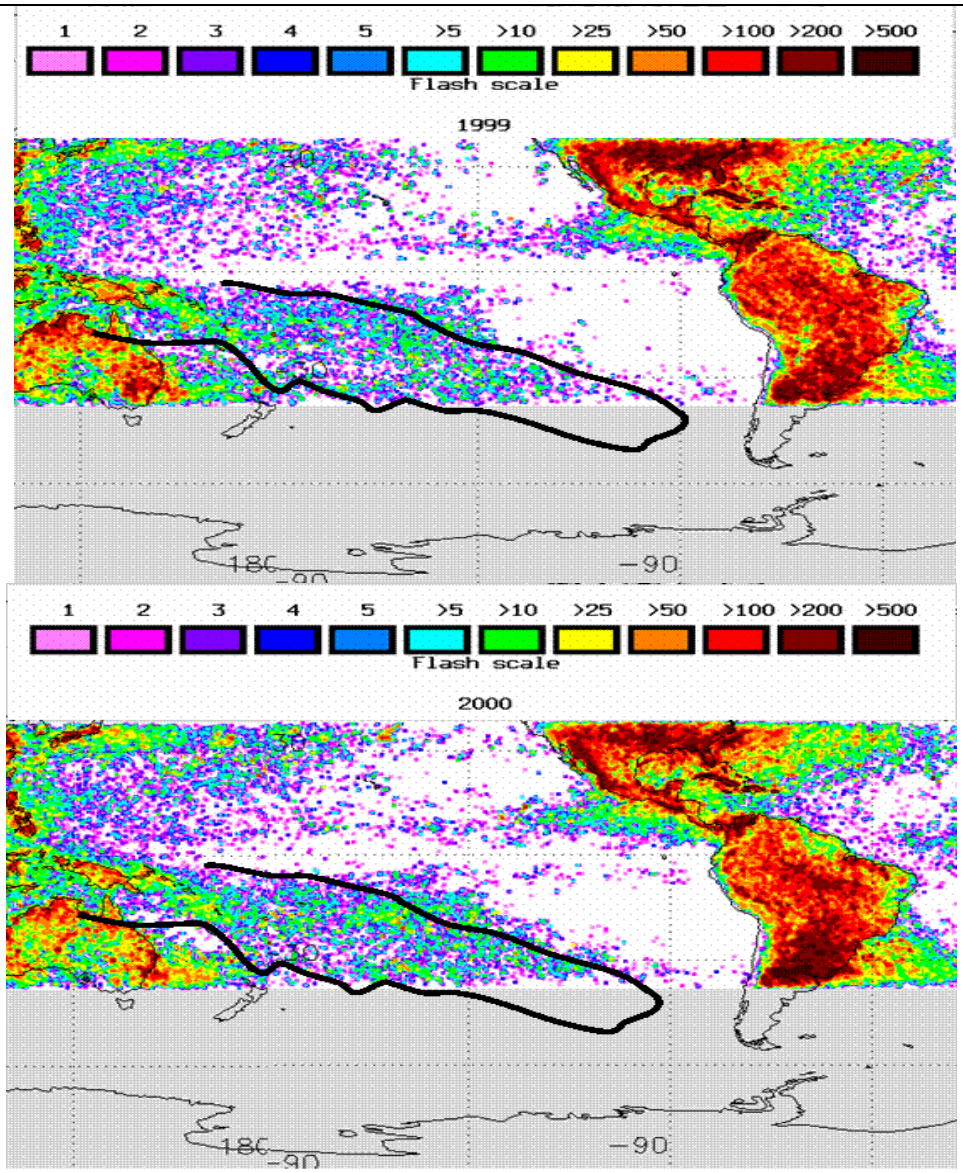

Figure 22: The number of lightning strikes (flashes) for a given portion of the South Pacific during 1999 and 2000.

rates and divergence improves with height in the boundary layer as the majority of the rain days are accompanied by 850 hPa convergence. A very similar behavior is noted in the mid-latitude portion of the North Pacific (shown in figure 21) and the North Atlantic (not shown) storm track. From these results, it is clear surface and 1000 hPa convergence is less important to the

development of rain in the ST and ML SPCZ. These results help us understand why divergence is present in this region of the SPCZ.

Lightning Characteristics in the SPCZ Region

As an aside, I was also interested to see if there were any differences in the lightning characteristics of the SPCZ with those of the NHITCZ region. For this I used images generated by the NASA/LIS/OTD Science team available from the web at http://thunder.msfc.nasa.gov. Figure 22 shows the average lightning flashes (both cloud-to-cloud and cloud-ground) for 1999 and 2000 as observed by the Lighting Imaging Sensor (LIS) on the TRMM satellite. The LIS is detects lightning by detecting momentary changes in the brightness of clouds illuminated by lightning. The data used in this study is data that has not been quality controlled but it does provide a quick look at the South Pacific and the tropical North Pacific. Outlined in black is the three year average of the SPCZ and much of the lightning in the South Pacific is concentrated within this region. Within the SPCZ region there are two lightning maxima: one is associated with the Solomon Islands and New Caledonia while the other appears to be associated with the Austral, Society and Tuamotu Islands. Lucas et al. (1994) documented that updraft velocities associated with cumulonimbus clouds over land are higher than those over the ocean. As strong updrafts and the presence of graupel and smaller ice particles appear to be important factors to the development of cloud electrification (Houze, 1993) it is not surprising that the lightning maxima are associated with these island regions. What is surprising is that tropical portions of the SPCZ have more lightning activity than in the NHITCZ region. The presence of the Marshall and Caroline Islands within the NHITCZ domain argues against the lack of land area being the reason for the regional differences in lighting. Why should there be such a difference between convection in these two regions such that lightning activity is more common in the tropical SPCZ? This question is an item that is left for additional research.

Summary

Mean spatial distributions of satellite derived SST, vertical wind shear, convergence and rain rate fields reveal a number of interesting features. Sub-tropical and mid-latitude portions of the SPCZ rain rate maximum are located above a strong gradient in SSTs, a characteristic that has been noted in other studies (Kiladis et al, 1989; Hurrell et al, 1998; Vincent, 1998). Examination of the vertical wind shear between 850 and 200 hPa revealed a maximum over sub-tropical and mid-latitude sections of the SPCZ, the same locale of the strong SST gradient. A strong sub-tropical jet has been previously connected with the SPCZ (Vincent, 1982; Kodama, 1992 and 1993) and this feature is the reason for the vertical shear maximum in this region.

The distributions of surface convergence and SST fields indicate a close relationship between the two in tropical regions. I believe the following physical factors are contributing to the development of this pattern. With the exception of the equatorial cold tongue, the SSTs of the tropical Pacific are quite warm (> 26°C). Since advection processes are weak in these areas surface air temperatures run about 1°C cooler than the local SST. Air over these warm water regions becomes positively buoyant resulting in upward vertical motion. By mass continuity, there must be mass inflow to replace that lost via upward motion through the atmosphere. Hence, the warmer waters lead to the development of weak low pressure and persistent convergence throughout the year.

Comparison of the satellite derived rain rate and near surface convergence distributions provided a surprising finding. Convergence and higher rain rates were, in general, co-located in the NHITCZ and tropical sections of the SPCZ. There is substantial divergence under the sub-tropical and mid-latitude sections of the SPCZ rain rate maximum, a region where convergence was expected. Instead, the axis of maximum convergence, which is zonally oriented in tropical and southeastward oriented in higher latitudes, is eastward and equatorward of the SPCZ rain

rate maximum at sub-tropical and mid-latitudes. The rms of the convergence field reveals the highest variability over the sub-tropical and mid-latitude sections of the SPCZ. The low mean divergence and high variability indicate this portion of the SPCZ experiences periods of convergence and divergence. It is likely these patterns are related to seasonal changes in the Southern Hemisphere storm track. As sub-tropical and higher latitudes of the SPCZ rain rate maximum is also a region of substantial vertical wind shear, the results suggest that baroclinic cyclones may be important in providing rainfall in this region. However, it should be noted that these results are from two and three year means while baroclinic cyclones have time scales of about a week. Therefore, an examination of seasonal and higher frequency data is appropriate before definite conclusions can be made.

The NCEP Re-analysis 1000 hPa rain rate and convergence fields were compared to those derived via satellite. Major differences exist between satellite derived and NCEP rain rate maxima. The result is the SPCZ in NCEP rain rate data is much more zonally oriented, a characteristic noted by other investigators as well (Janowiak, et al. 1998; Trenberth and Guillemot; 1996). Scatterometer derived and NCEP convergence fields were nearly co-located in the South Pacific, the major difference being the much higher magnitudes of the scatterometer convergence. Surprisingly, NCEP rain rate maxima in the tropical regions are quite closely co-located with the scatterometer derived convergence fields. Because the surface convergence fields are closely related to warm SSTs in the tropical regions, the result suggests the NCEP convective parameterization may be overly dependent on the SST field.

Examination of the vertical structure of convergence in the South Pacific showed that at 1000 hPa convergence maxima in the South Pacific are zonally oriented. However, convergence becomes more closely co-located with the southeastward oriented SPCZ rain rate maximum at the 850 hPa and 700 hPa levels. Height and wind distribution changes within the atmospheric

column show ridging, which in the lowest layers cuts across the SPCZ rain rate maximum. This seems unusual, but it should be remembered that the rain rate maximum lays across the weakness in the sub-tropical ridge axis and lies on the western periphery of the much stronger Southeast Pacific Sub-tropical High. An examination of seasonal and higher frequency data will likely shed more information on the development of this pattern.

Scatter plots of rain rates and divergence across selected regions of the SPCZ clearly reveal that convergence throughout the boundary layer is important to the development of rain in the tropics. Surface and 1000 hPa convergence are much less important to the development of rain at sub-tropical and mid-latitudes. This suggests precipitation processes, such as those associated with the development of stratiform rain or elevated convection, are more important in these regions. The presence of a vertical shear maximum and surface divergence within sub-tropical and mid-latitude sections of the SPCZ can be interpreted as evidence that mid-latitude cyclones may have a substantial impact on the rainfall in this region. Finally, I found that lightning was not uncommon within the SPCZ region with maxima closely associated with groups of islands. However, lightning activity in the tropical portions of the SPCZ are higher than that found in the NHITCZ. It is not understood why this is the case and it is certainly an area worthy of additional research.

CHAPTER IV

SEASONAL DISTRIBUTIONS OF SOME PHYSICAL PARAMETERS IN THE SPCZ

In the previous chapter, a strong SST gradient, substantial vertical wind shear and weak surface divergence characterized the mean conditions over the sub-tropical and mid-latitude portions of the SPCZ rain rate maximum. The distribution of convergence, however, changed substantially above the surface such that it was prevalent over the sub-tropical and mid-latitude portions of the SPCZ rain rate maximum at 850 hPa. For further understanding, I shift my attention to seasonal analysis to determine if the characteristics found in the mean analysis are observed. Therefore, seasonal analysis of SSTs, vertical wind shear, convergence, rain rates and NCEP re-analysis data are discussed in this chapter. In this study, all seasons will be assumed to be Austral unless explicitly stated otherwise. Seasons are defined by the following: December through February is summer; March through May is fall; April through June is winter; September through November is spring.

Seasonal Distribution of SSTs, Rain Rates and Vertical Wind Shear

Figure 23 shows the seasonal averages of SST and rain rates. During Austral winter, there are two distinct rain rate maxima in the South Pacific; one at tropical latitudes of the SPCZ and another at middle latitudes. The rain rate maximum at higher latitudes occurs in a region where a strong SST gradient is present while the tropical maximum is associated with SSTs > 27°C. The NHITCZ rain rate maxima remain broad in the Western Pacific and narrow in the Eastern Pacific. The broad rain rate maximum in the Western Pacific is associated with the broad region of warm SSTs commonly referred to as the Pacific Warm Pool. The cold SSTs off of the South

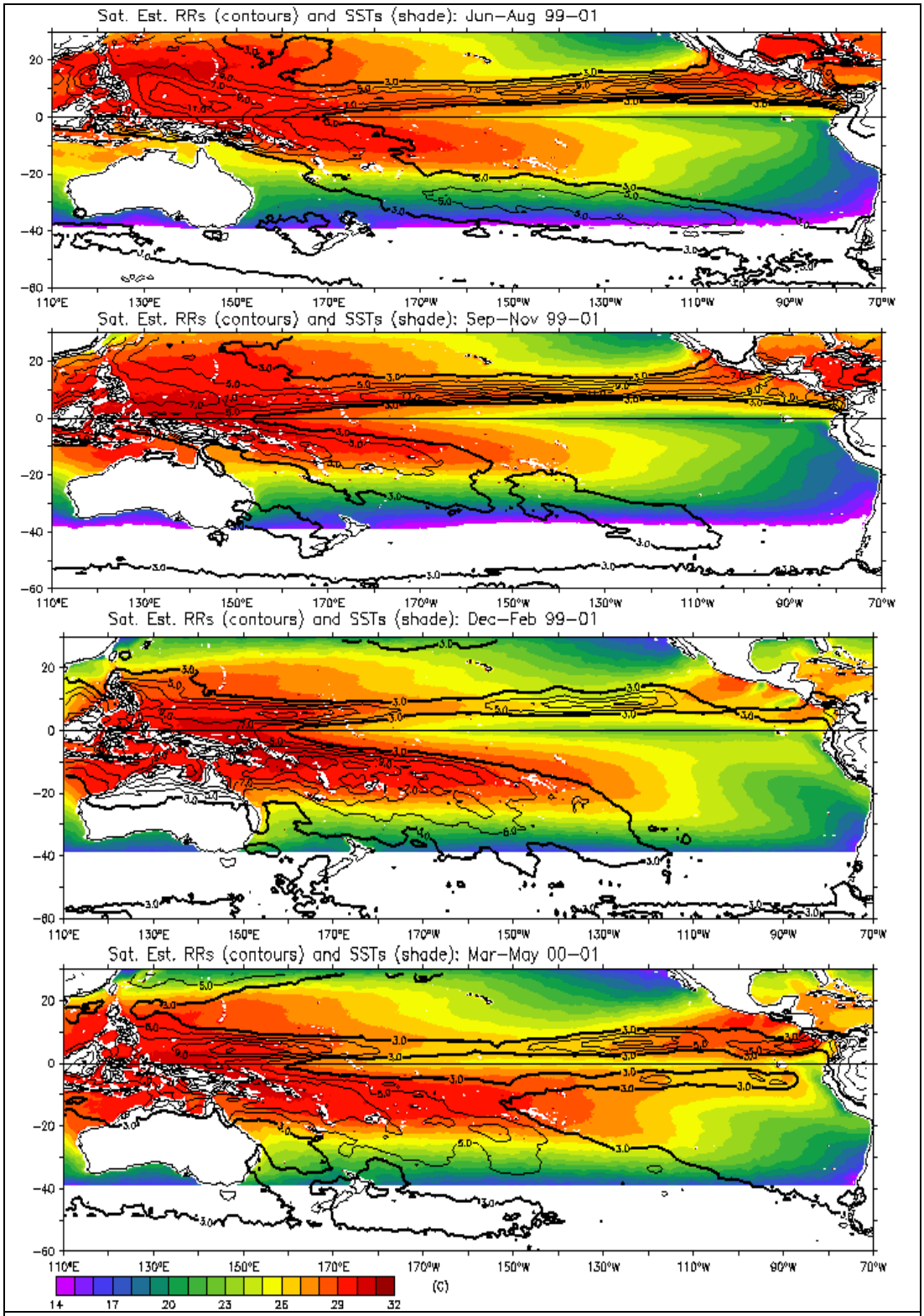

Figure 23: Seasonal averages of rain rates (contoured) and SSTs (shade). Seasons are from top to bottom: winter, spring, summer and fall.

American Coast are associated with coastal upwelling. Additionally, the equatorial cold tongue in the Eastern Pacific is clearly present during this season.

During spring, the two SPCZ rain rate maxima are still present although some changes have begun to occur. The tropical maximum exhibits higher rain rates and has begun to spread further southeastward into portions of the sub-tropics, the most poleward portion of this maximum lying over a tight SST gradient. The higher latitude maximum exhibits lower rain rates than those seen in winter, remains located over very cool SSTs and has decreased areal extent. The NHITCZ continues to remain broad in the West and narrow in the East Pacific. Upwelling off the coast of South America, as evidenced by the cold SSTs, remains substantial and the equatorial cold tongue exhibits the coldest SSTs during this season.

In summer, a single SPCZ rain rate maximum is present and is zonally oriented; most of the higher rain rates, values > 5mm/dy, are located over the warmer SSTs, values > 28°C, in the tropics. As the Pacific Warm Pool decreases in areal extent the NHITCZ becomes narrower in the West Pacific; rain rates in the East Pacific have decreased substantially, likely due to the cooling of regional SSTs. Along the western coast of South America and the equatorial cold tongue, the SSTs have begun to warm due to decreased upwelling. Note that a zonal band of SSTs > 24°C has developed in the Southeastern Pacific Ocean.

The SPCZ rain rate maximum during fall takes on a more northwest-to-southeast orientation. In equatorial latitudes, however, a branch of the rain rate maximum extends from New Guinea, where it is broad, to the eastern equatorial South Pacific, where it is very narrow. In the eastern equatorial South Pacific this rainfall maximum is called the Southeast Pacific ITCZ (SEITCZ) and it typically occurs from late February into April. Not surprisingly, the SEITCZ is located over the same zonal band of warm SSTs that developed in the Southeastern Pacific during the

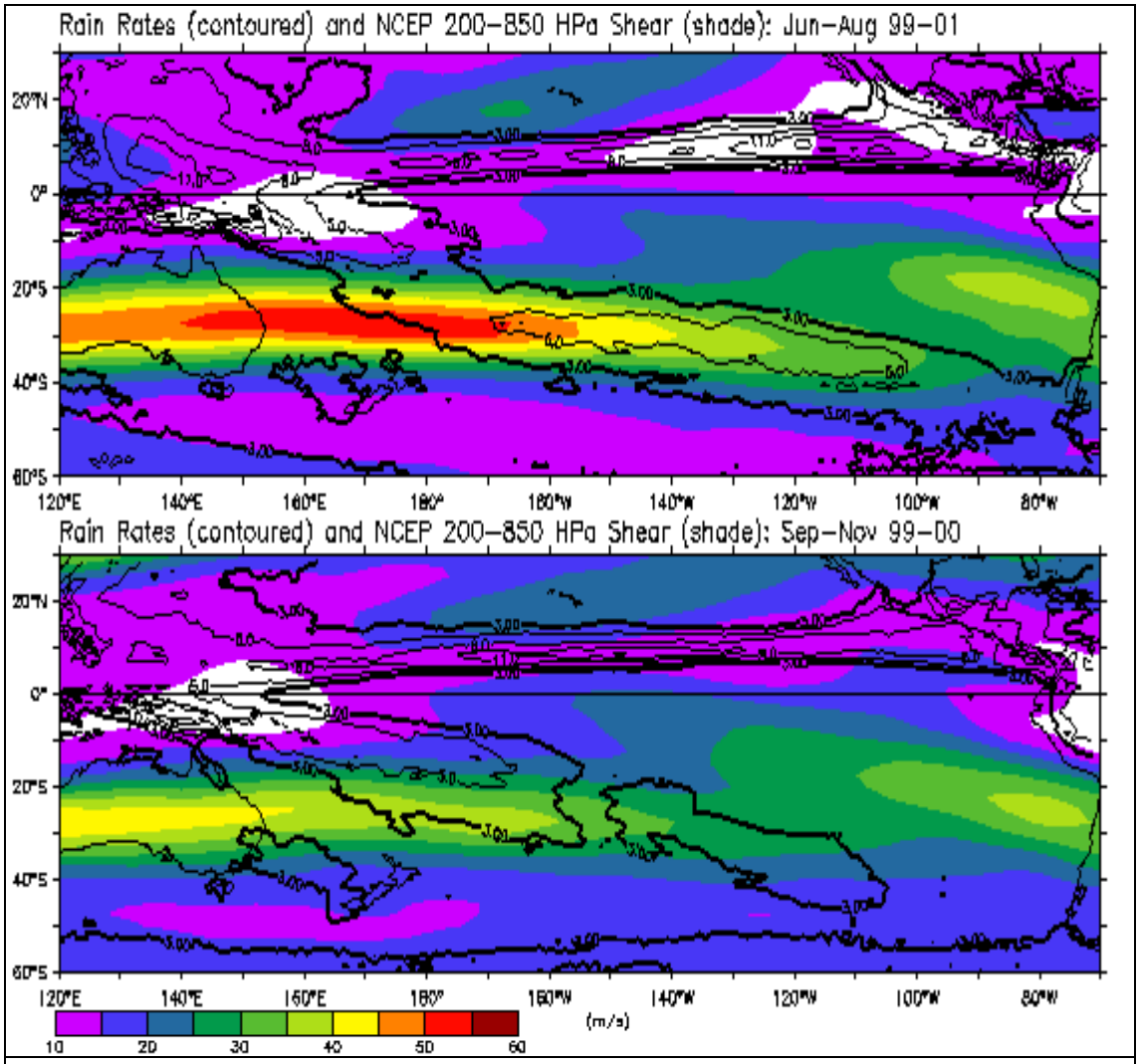

Figure 24: Seasonal averages of rain rates (contoured) and 850-200 hPa vertical wind shear (shade). Seasons are winter (top) and spring (bottom).

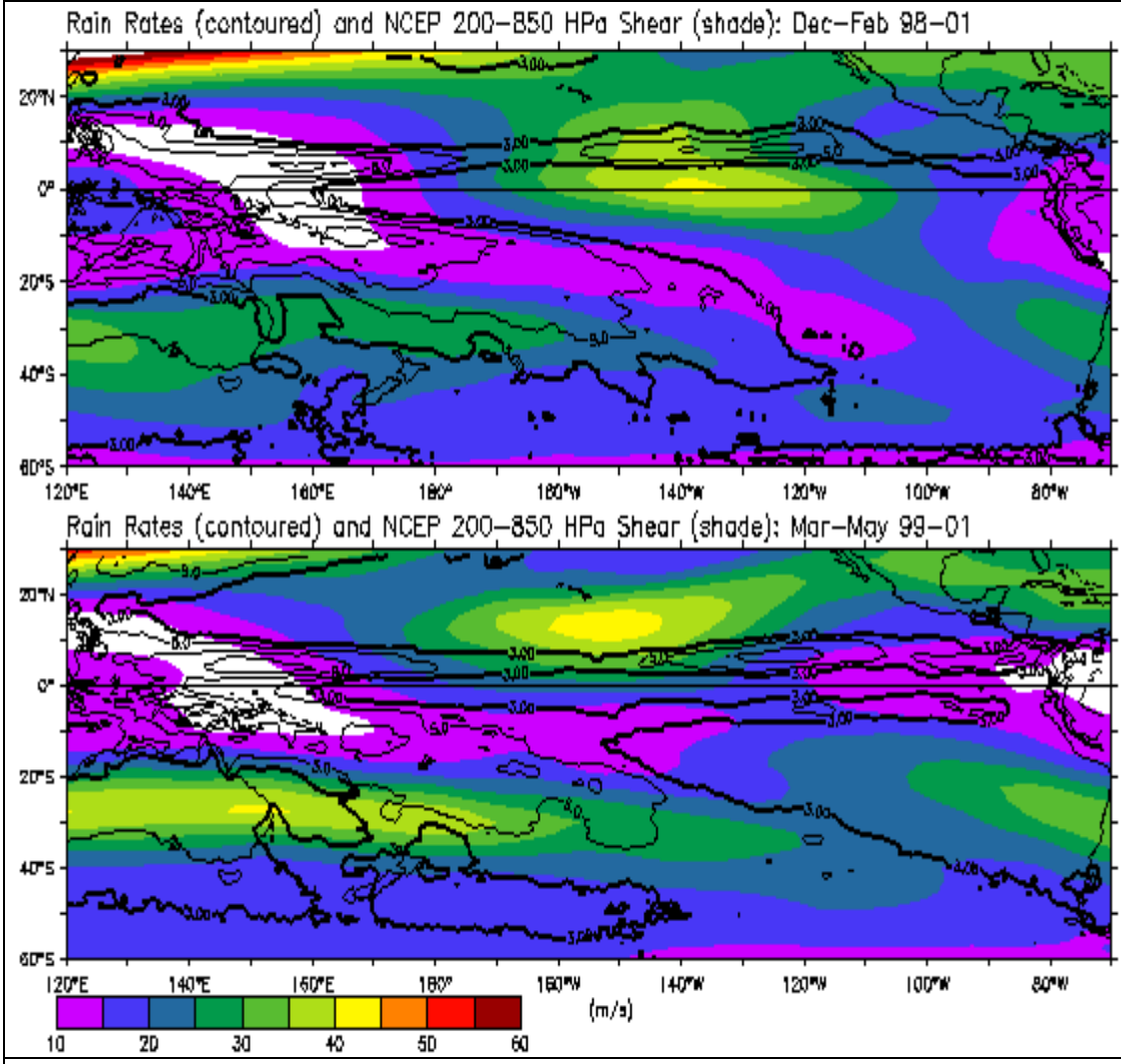

Figure 24 continued: Seasons are from summer (top) and fall (bottom).

previous season. In this analysis, the SEITCZ appears to be linked to the development of warmer SSTs off of the western South American Coast during the previous season and is still present during fall. In fall, the temperatures in this zonally oriented SST maximum are now in the 26° to 27°C range. The SEITCZ and the NHITCZ in the Northeastern Pacific are part of a double ITCZ system that is present for only a brief time in fall.

Next, seasonal analysis of the vertical wind shear and the variability of the meridional wind are examined. Large values of vertical wind shear are characteristic of a baroclinic atmosphere through the following relationship:

$$\partial V_g/\partial(\ln)P = -R/f\ \underline{\mathbf{k}}X(\nabla T)_p \qquad (7)$$

where 'V_g' is the geostrophic wind, 'P' pressure, 'R' the gas constant, 'f' the Coriolis parameter and '(∇T)' the horizontal pressure gradient. The 'bold' type represents vectors in this equation. In this equation vertical wind shear is directly related to the horizontal temperature gradient. It is also related to the maximum baroclinic growth possible within the Eady model of the atmosphere as outlined by Gill (1982) in the following:

$$\sigma_{max} \equiv 0.3098(f/N_*)d\,|U|/dz_* \qquad (8)$$

where 'f' is the Coriolis parameter, 'N*' the static stability and dU/dz* the vertical wind shear. Note that the maximum baroclinic growth is also dependent on the ratio of the Coriolis parameter and the static stability. The point I make here is vertical wind shear is related to the baroclinicity of a given portion of the atmosphere, and is important to the magnitude of the growth of baroclinic waves.

The storm track is a term used to denote the preferred track of cyclones over a given portion of the earth. Some investigators (Trenberth, 1991; Rao, et al. 2002) have used the variability of the meridional component of the upper level wind to denote the mid-latitude storm tracks. The reason for this is there is usually more variability found in the meridional wind, due to the passage of ridges and troughs, than is found in the zonal wind. In this paper, when I use the term "storm track" I am referring to the region of high variability in the 200 hPa wind. Figure 24 and 25 show the seasonal changes in the 850-200 hPa vertical wind shear and the storm track along with rain rates in the tropical North and South Pacific. Throughout each season, the portion of the SPCZ rain rate maximum equatorward of 15°S lies within a regime of low (15 m/s or less)

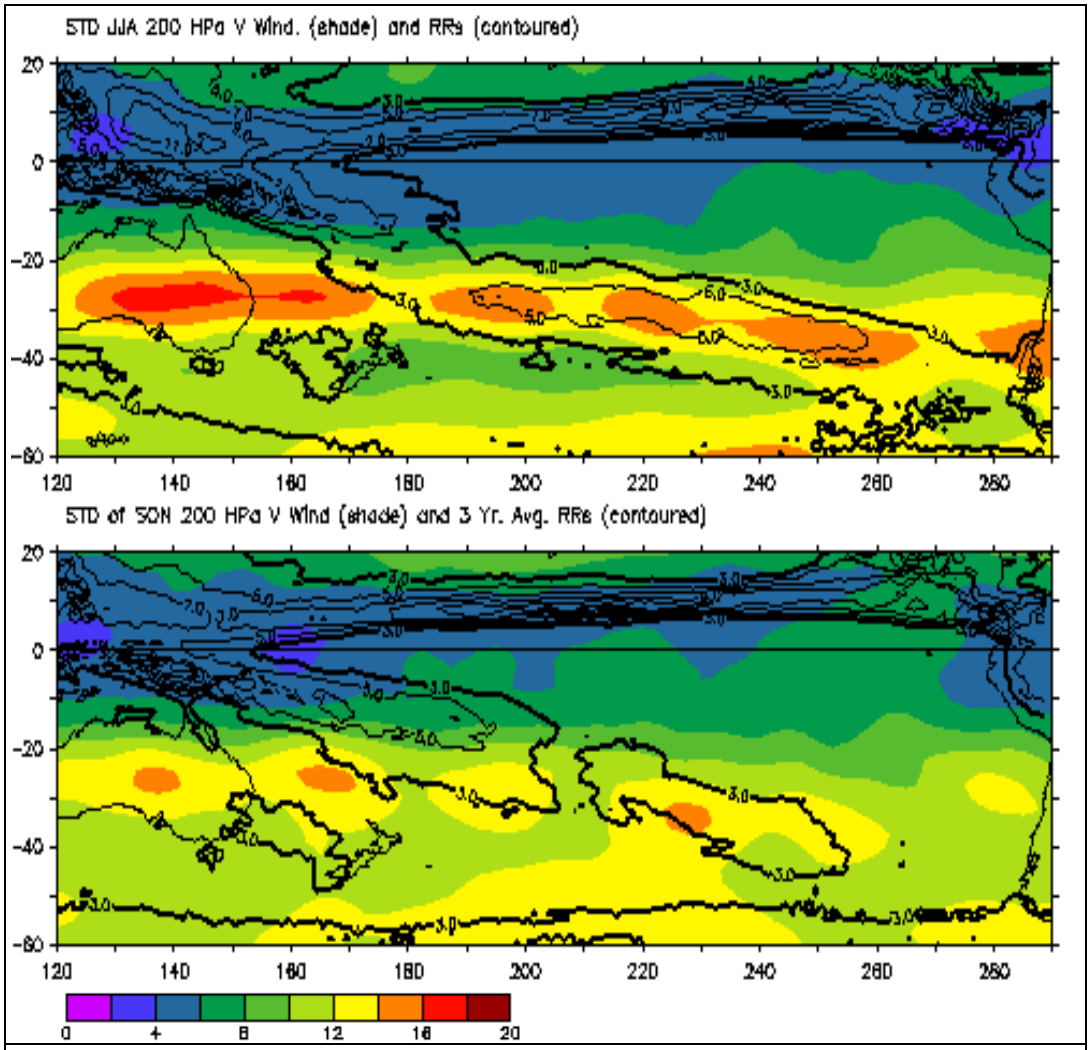

Figure 25: Seasonal averages of rain rates (contoured) and the standard deviation of the 200 hPa wind (shade). Seasons are winter (top) and spring (bottom).

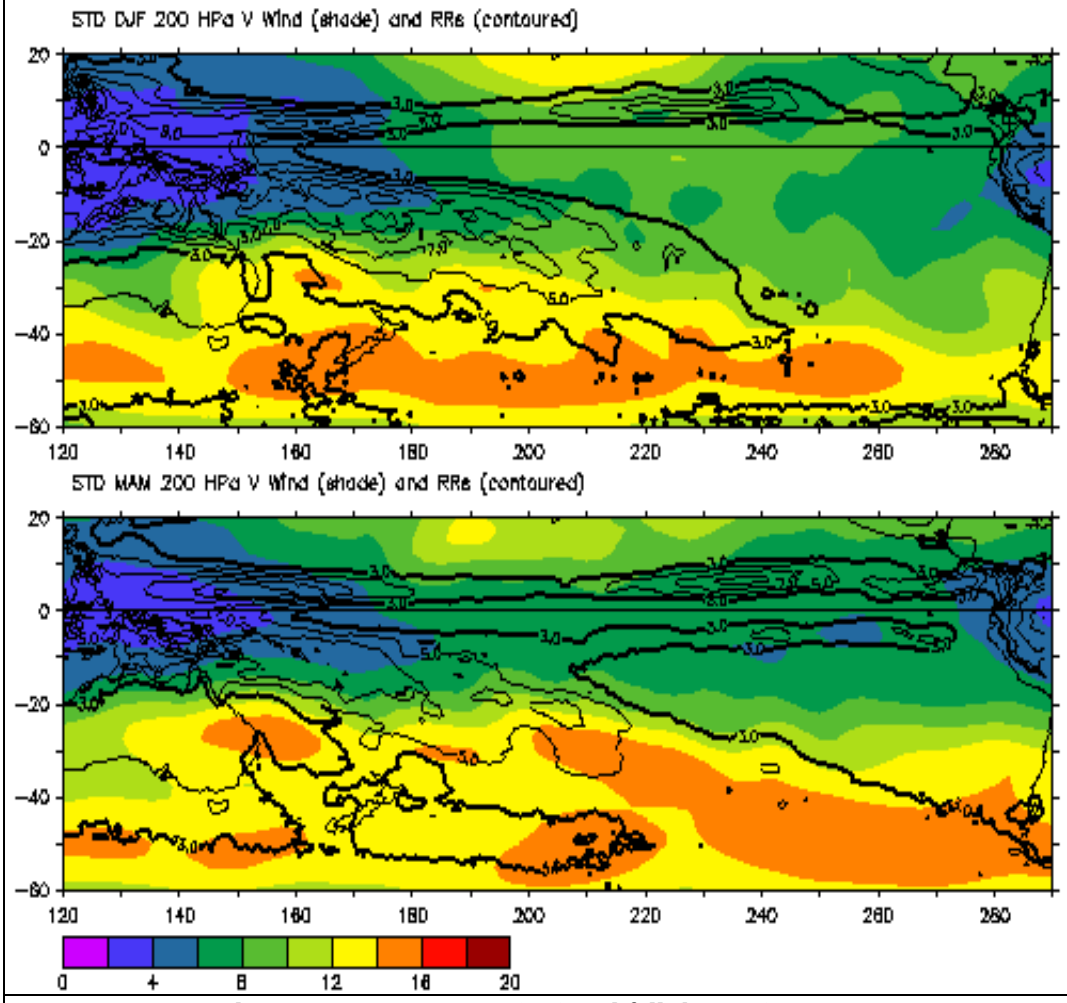

Figure 25 continued: Seasons are summer (top) and fall (bottom).

vertical wind shear. Poleward of this latitude, a maximum in vertical wind shear is present which is strongest during winter and weakest during summer. Notice that the wind shear maximum remains in the same approximate position throughout the four seasons, weakening or strengthening "in place." This is the same approximate location of the SST gradient during each season. During winter, a strong vertical shear maximum extends well into the higher latitude SPCZ rain rate maximum. This higher latitude rain rate maximum is in a location coinciding with the storm track for this time of the year as noted by Trenberth (1991) and Rao, et al. (2002).

During spring, the vertical shear decreases, reflecting a weaker jet stream, and the storm track, although still present, migrates poleward. Correspondingly, the higher latitude rain rate maximum weakens. There is still a significant amount of vertical wind shear, in the 15-25 m/s range, present over the SPCZ rain rate maximum poleward of approximately 17°S during the summer although clearly the storm track is placed well poleward. In fall, vertical shear increases again and a distinct maximum in the variability of the meridional wind is co-located with the SPCZ rain rate maximum. These findings confirm that the higher latitude sections of the SPCZ rain rate maximum is nothing more than a manifestation of the mid-latitude storm track during winter. Additionally, the potential for baroclinic cyclone activity in this same region exists during fall, spring and, in a limited sense, summer. Note that there are differences in the distributions of vertical wind shear and the storm track during summer. Specifically, the wind shear is not quite as strong at high latitudes although a secondary maximum is present. Here, it should be pointed out that baroclinic growth is dependent not only on the vertical wind shear but also on the ratio of the Coriolis parameter to the static stability; this ratio is larger at higher latitudes, hence the higher latitude storm track.

Seasonal Distribution of Convergence

Figure 26 shows the seasonal distribution of scatterometer derived convergence and TRMM SSTs for the Pacific basin. As I am particularly interested in the distribution of convergence with respect to the SSTs, I have shown positive values only. During the different seasons, surface convergence maxima tend to migrate with the SST maxima and are approximately co-located. In the Northern Hemisphere, the convergence maximum in the Eastern Pacific migrates meridionally during the different seasons, is rather narrow in width and is zonally oriented. The

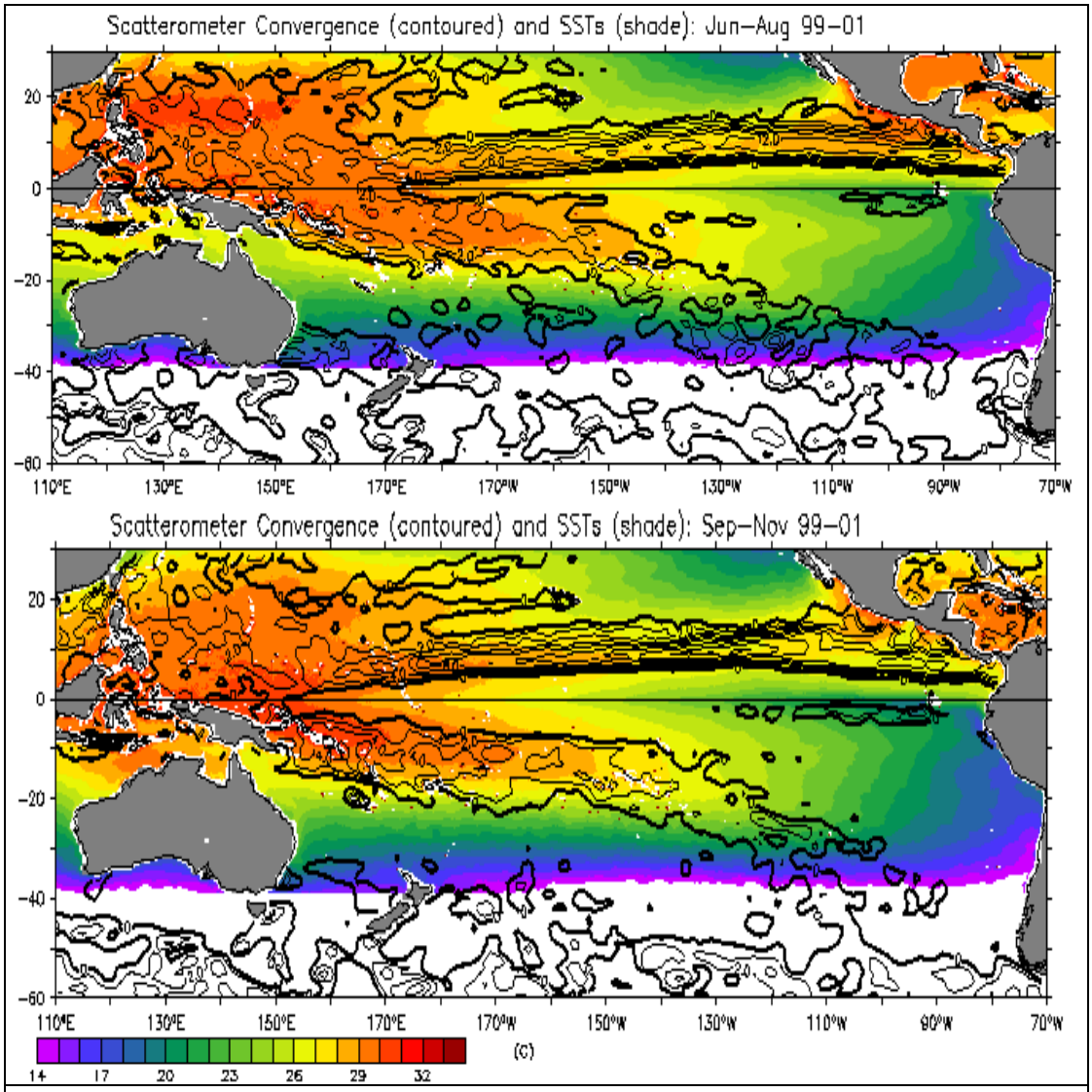

Figure 26: Seasonal averages of surface convergence (contoured) and SSTs (shade). Seasons are winter (top) and spring (bottom).

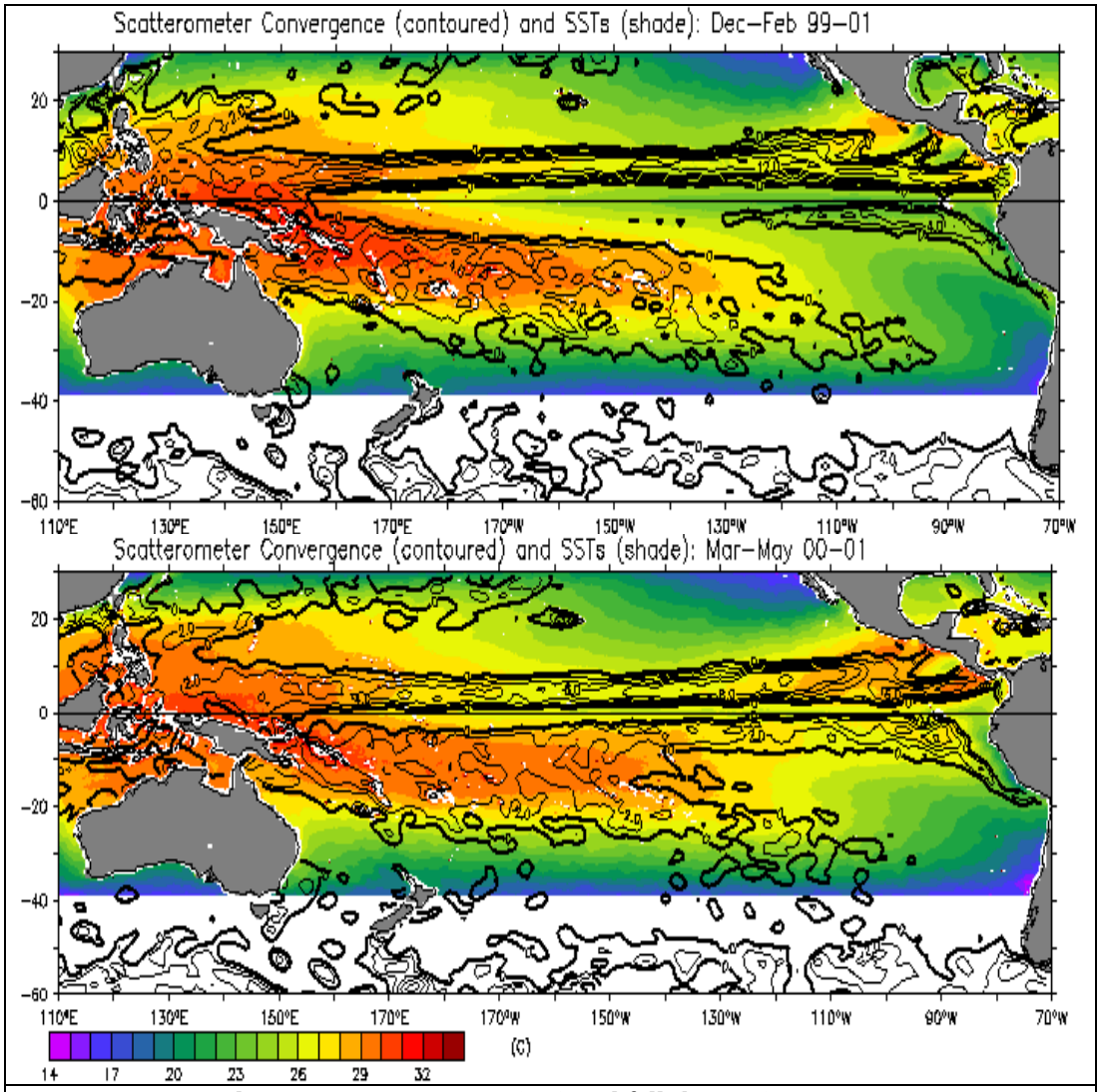

Figure 26 continued: Seasons are summer (top) and fall (bottom).

convergence pattern in the Western Pacific is also narrow during the Austral summer and fall seasons, but becomes broad during winter and spring as the Pacific Warm Pool increases in size.

During winter in the tropical South Pacific, the surface convergence maximum, part of which is associated with the tropical portion of the SPCZ rain rate maximum, extends zonally in a broad band to near 150°W. From there, the maximum takes a more southeastward orientation and extends into the mid-latitudes. In the far eastern South Pacific, between 110° and 90°W,

there is a small region of surface convergence at equatorial latitudes. There is an intense, zonal band of divergence (not shown) closely co-located with the equatorial cold tongue. Wallace et al. (1989) and Mitchell and Wallace (1992) have documented this phenomenon and postulated it is related to the equatorial cold tongue. Their argument starts with the observation that the boundary layer wind flow over this region remains approximately the same, yet the surface winds vary by as much as a factor of four across the equatorial cold tongue. They then argue that over the warmer waters low static stability is present, leading to more boundary layer mixing. This allows higher momentum air to mix toward the surface. Over the cooler waters, higher static stability leads to less boundary layer mixing; therefore higher momentum air does not reach the surface. The result is a couplet of convergence south of the cold tongue, and divergence north of it.

During spring, a broad surface convergence maximum in the western and central South Pacific has expanded eastward by approximately 15 degrees longitude before extending southeastward into the mid-latitudes. As during previous seasons, the surface convergence maximum remains nearly co-located with the warm SSTs. The southeastward extension of the convergence maximum is not as well defined as it was during winter. In the far eastern South Pacific, the small region of convergence has increased in magnitude and has increased in zonal length. Even now, there are indications of twin convergence zones developing in the South Pacific.

By summer twin surface convergence maxima have developed within the eastern Pacific Basin with warm SSTs stretching from the western to the eastern South Pacific. Likewise, a broad surface convergence maximum stretches into parts of the eastern South Pacific, as far east

as 120°W. The southeastward extension of the surface convergence zone into middle latitudes, previously seen during winter and spring, is barely discernible. In the far eastern South Pacific, a narrow convergence maximum stretches from the South American coast to near 130°W.

By fall, twin convergence maxima remain present in the eastern equatorial regions of the North and South Pacific. The broad, zonal surface convergence maximum in the tropical South Pacific stretches to 140°W where it splits into two maxima. The maximum at near equatorial latitudes is zonally oriented, narrow and closely associated with warm SSTs in the region. The second maximum is southeastward oriented, extending towards the mid-latitudes and is ill defined. It appears to be the re-development of the southeastward oriented surface convergence maximum previously observed during the winter and spring.

Figure 27 shows the seasonal distribution of surface convergence and rain rates for the Pacific basin. In each season, the SPCZ rain rate maximum in tropical latitudes is dominated by strong surface convergence that typically extends further east than the 3mm/dy rain rate contour. In sub-tropical and higher latitudes of the SPCZ, there are distinct seasonal changes in the position of the convergence and rain rate maxima with respect to each other. It appears the greatest difference between the location of convergence and rain rate maxima in the South Pacific is during the fall and spring. The portion of the SPCZ rain rate maximum equatorward of 25°S is characterized by strong surface convergence during fall and spring. Poleward of this latitude, where rain rates are in the 3-5 mm/dy range, weak divergence (not shown) dominates. During spring, there is also a distinct offset between surface convergence and rain rate maxima at sub-tropical and portions of the mid-latitudes of the SPCZ such that the axis of convergence is eastward and equatorward of the rain rate axis.

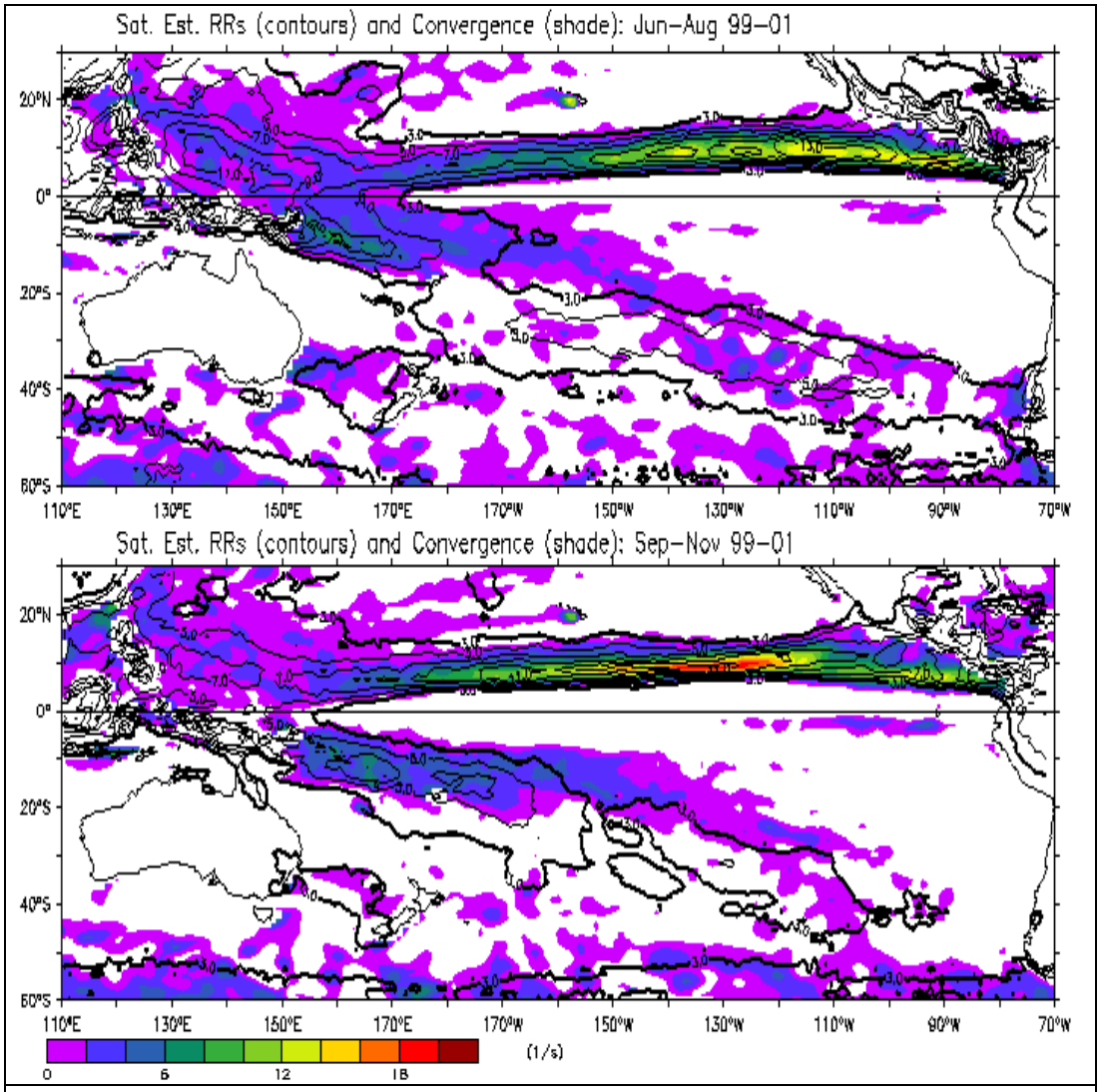

Figure 27: Seasonal averages of scatterometer derived surface convergence (shade) and rain rates (contours). Seasons are winter (top) and spring (bottom).

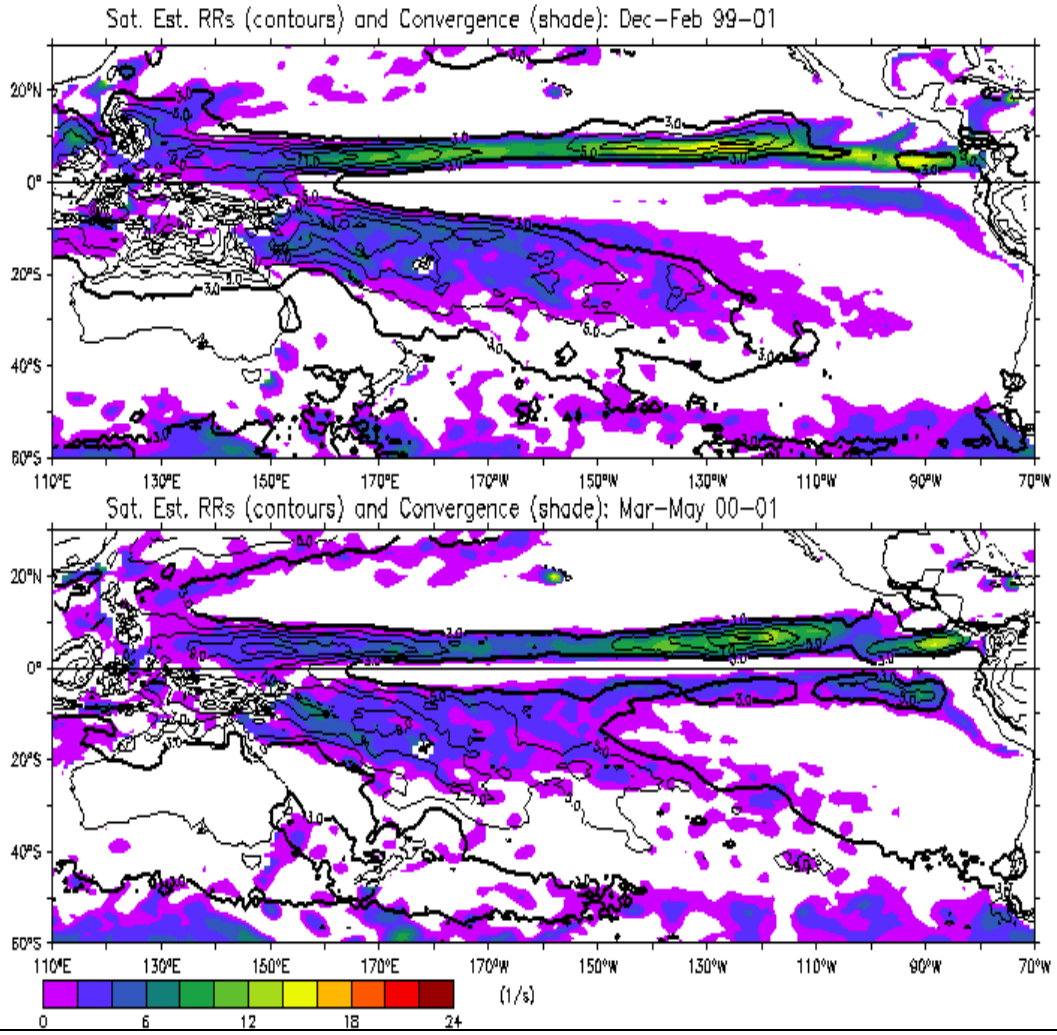

Figure 27 continued: Seasons are summer (top) and fall (bottom).

The convergence and rain rate maxima are more clearly co-located during summer than in all of the other seasons. However, it is still noteworthy that the rain rate maximum poleward of approximately 30°S is dominated by weak divergence. During winter, a good portion of the high latitude rain rate maximum is associated with westerly surface flow (not shown) and convergence. This information, as with previous findings, continues to confirm that the high latitude rain rate maximum is part of the winter mid-latitude storm track. The southeastward

oriented “diagonal” of weak surface convergence noted during fall, winter and spring extends toward the higher latitude portions of the SPCZ rain rate maximum and lends further evidence to the idea that this is a region where frontal systems weaken, stall and slowly dissipate. Hence, what is left behind is a persistent region of weak surface convergence. As mentioned in chapter III, this idea was one first espoused by Trenberth (1976). Further research using animation of rain rate, height and convergence data would be needed to either confirm or dis-prove this hypothesis and is left for another research project.

Although twin convergence maxima are visible during summer, it is only during fall that rain rates > 3mm/dy have developed to form the SEITCZ. During each season, the basic west-northwest-to-east-southeast orientation of the SPCZ rain rate maximum does not change although it does vary in how far it extends into sub-tropical and mid-latitudes. It appears that the convergence zone in the Eastern South Pacific shifts eastward as the seasons precede from winter through fall. Zonal changes in the SST distribution may be preceding changes in the convergence distribution within the equatorial Southeast Pacific, hence leading to the development of the SEITCZ. As there is a large seasonal cycle in the distribution of SSTs and convergence in the Southeast Pacific, it would be very interesting to document how these changes occur in conjunction with scatterometer wind and rain rate data. This is also left as an item for additional research.

The Vertical Distribution of Convergence and Heights

Figures 28 through 31 show the seasonal distribution of rain rates and NCEP convergence for the 1000 and 850 hPa levels. In general, each season exhibits a zonal convergence pattern at tropical latitudes. At sub-tropical latitudes a belt of divergence lays squarely across the SPCZ rain rate maximum at the 1000 hPa level during fall, winter and spring. At higher latitudes

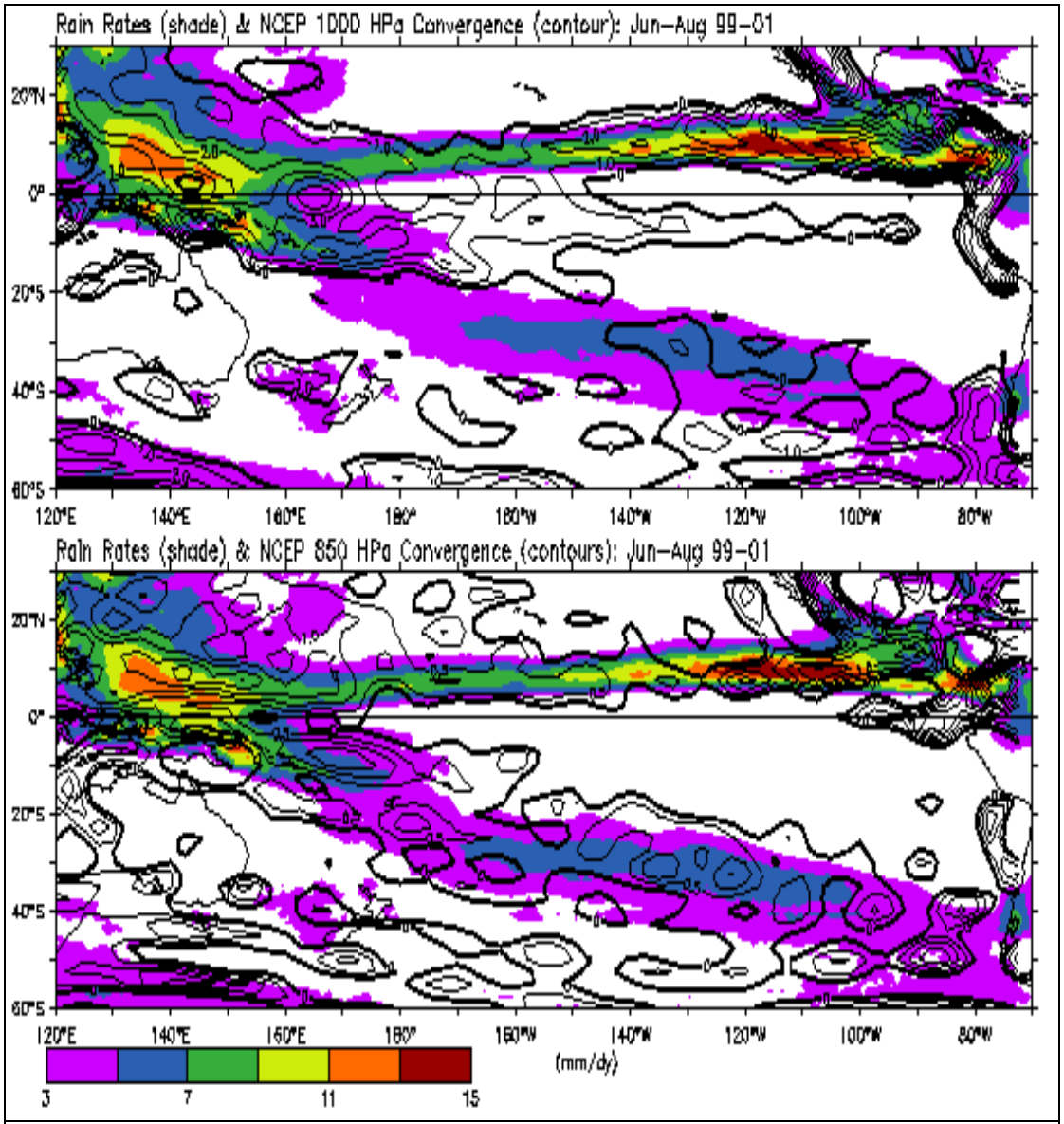

Figure 28: Three year average of 1000 and 850 hPa convergence (contours) and rain rates (shade) during Austral winter.

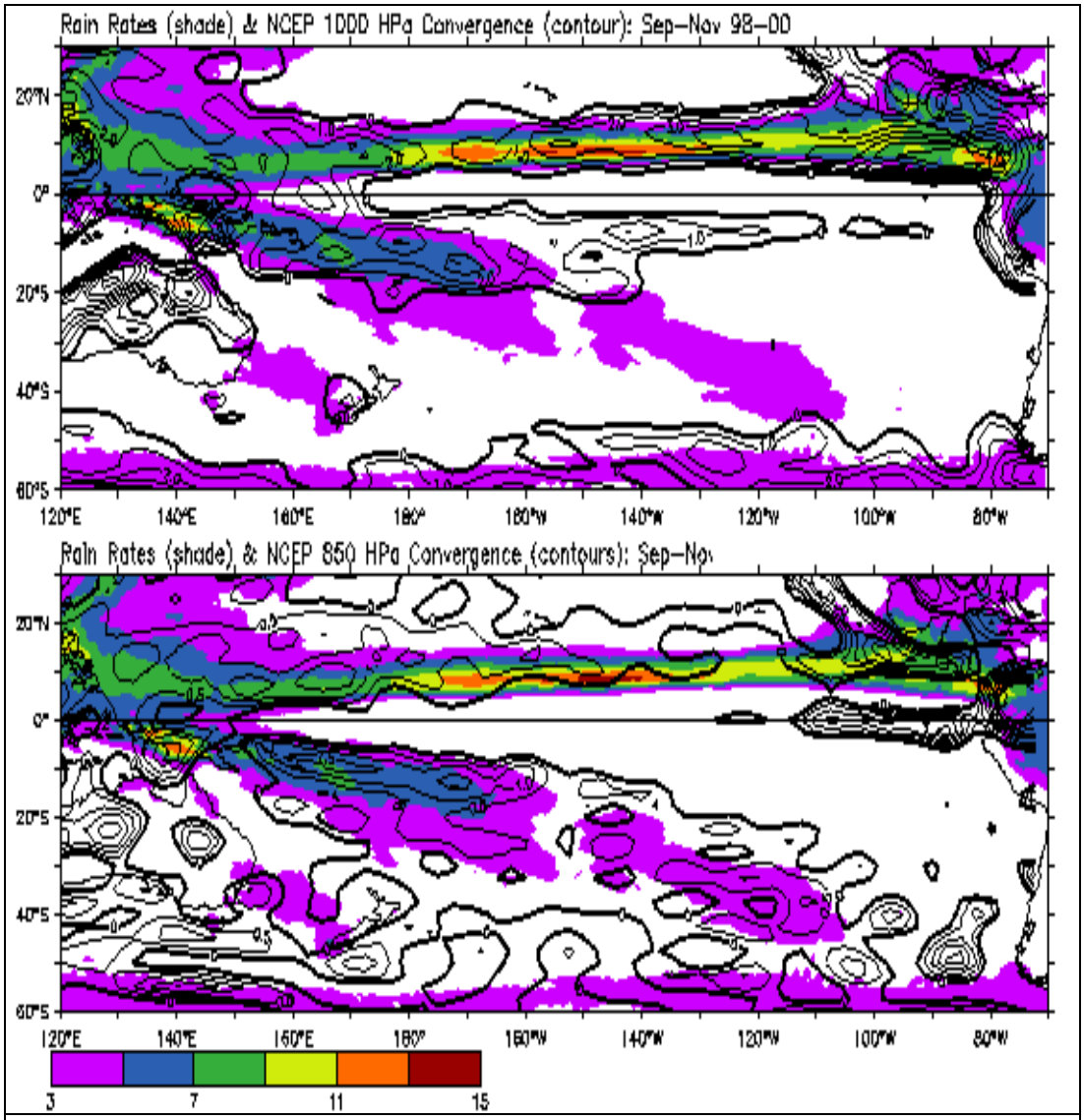

Figure 29: Same as figure 28 except for September through November.

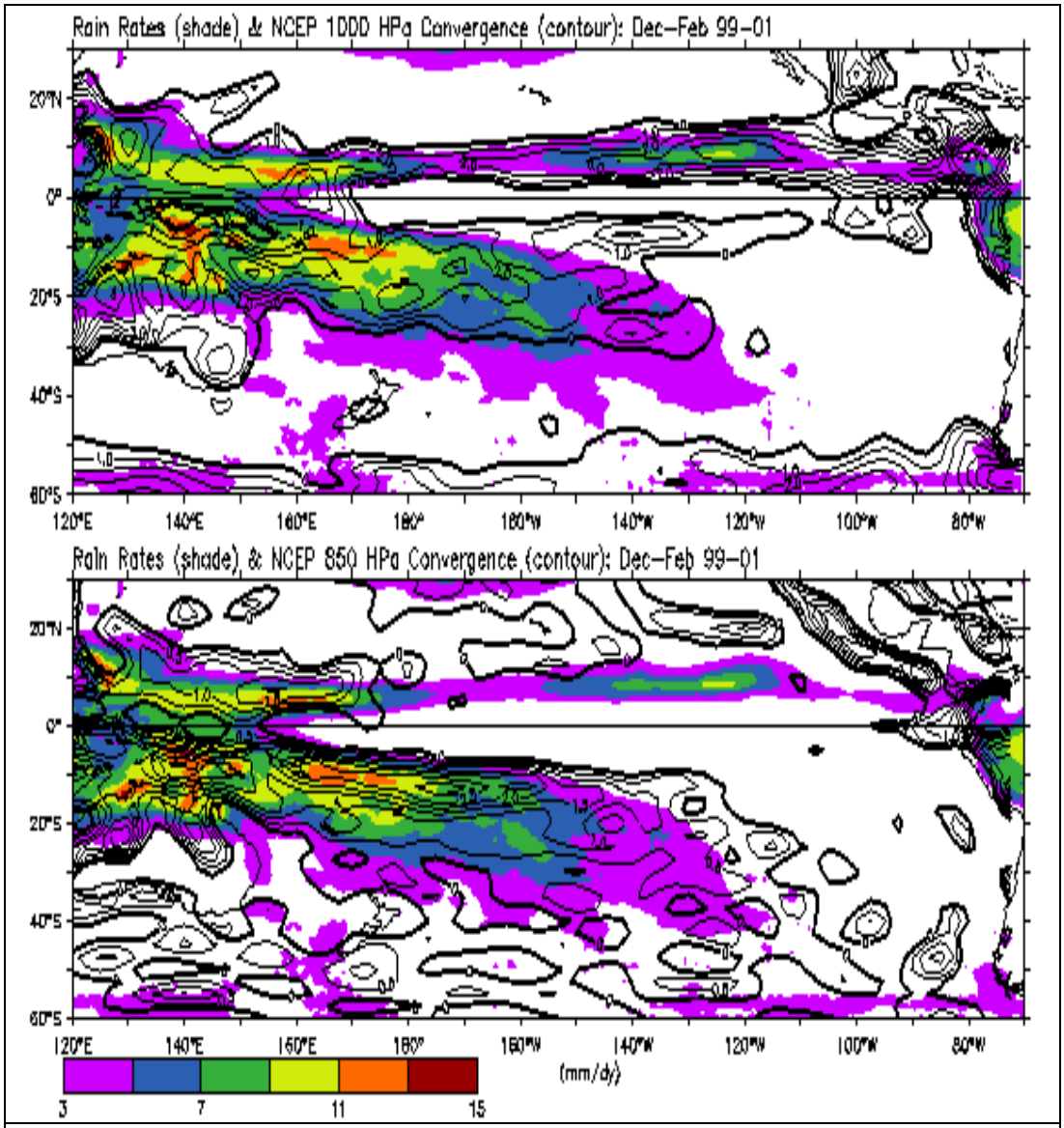

Figure 30: Same as figure 28 except for December through February.

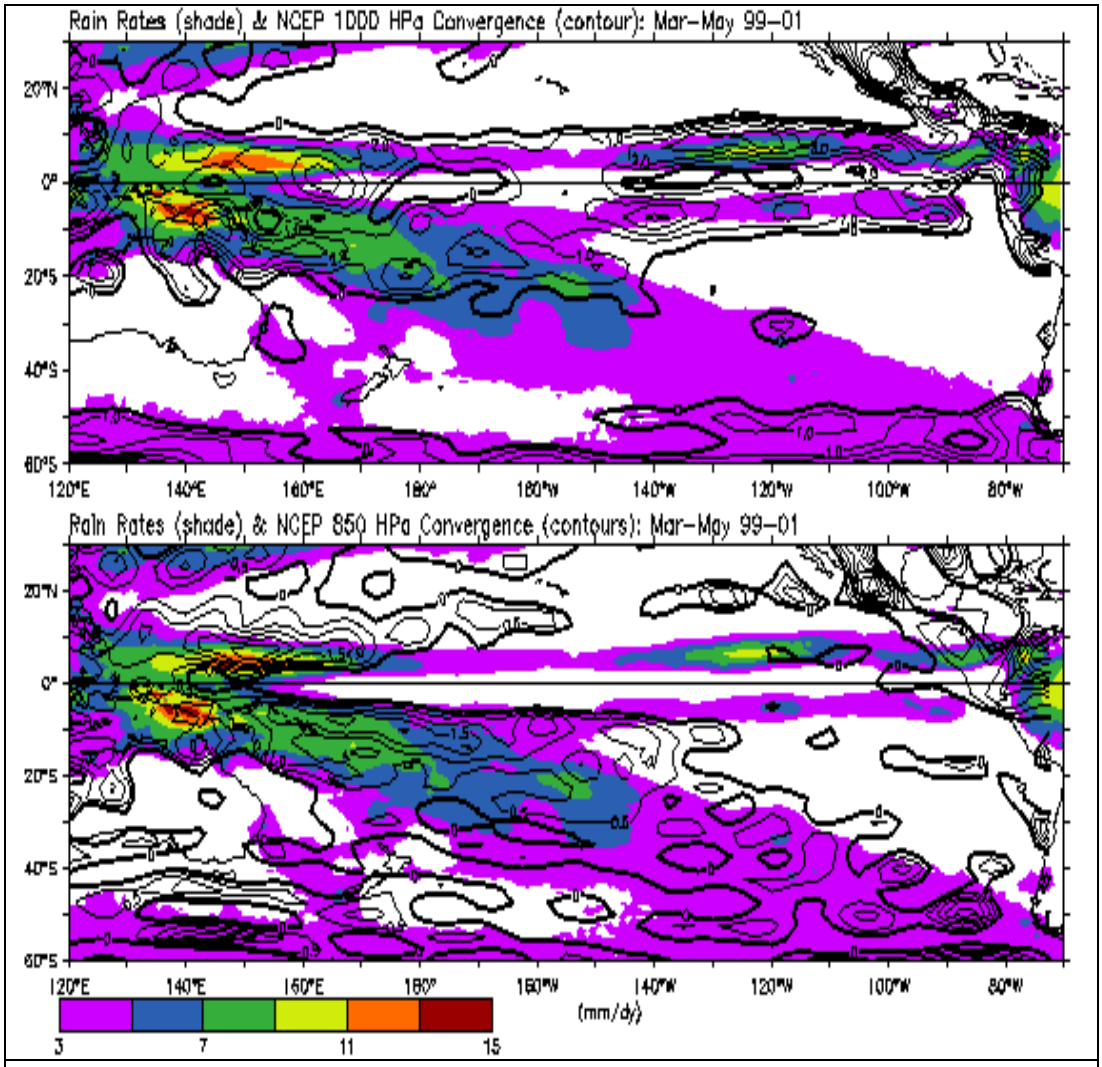

Figure 31: Same as figure 28 except for March through May.

(< 50°S) a persistent belt of convergence is present. The zonal pattern transitions to a northwest-to-southeast oriented pattern at 850 hPa that is closely co-located over the rain rate maximum. The greatest differences between the horizontal distribution of convergence at 1000 and that at 850 hPa occur at sub-tropical and middle latitudes during the fall and spring seasons while the smallest differences occur during summer. At tropical latitudes, the SPCZ rain rate maximum was characterized by convergence present throughout the boundary layer where the highest rain

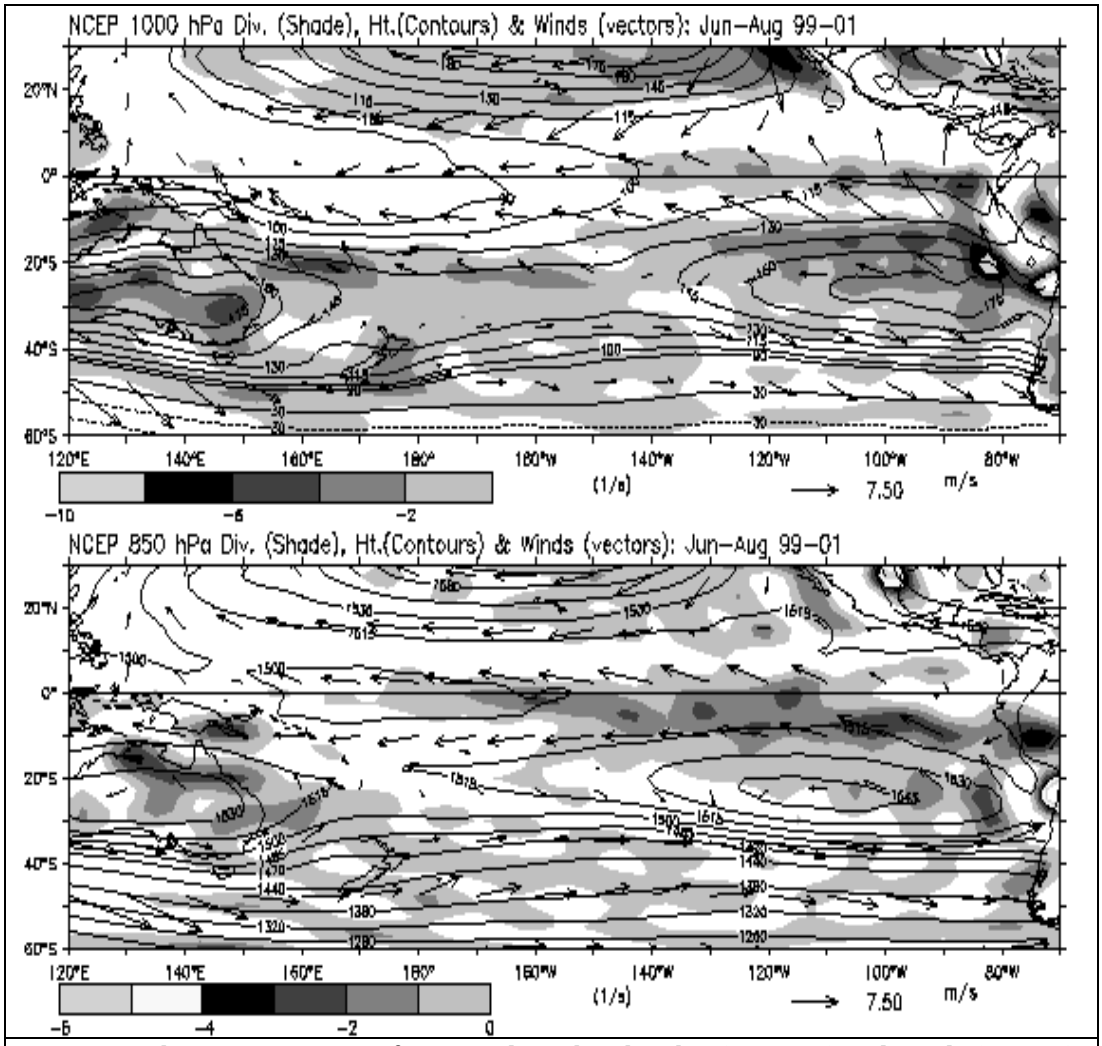

Figure 32: Three year average of 1000 and 850 hPa heights (contours) and winds (vectors) along with rain rates (shade) during Austral winter.

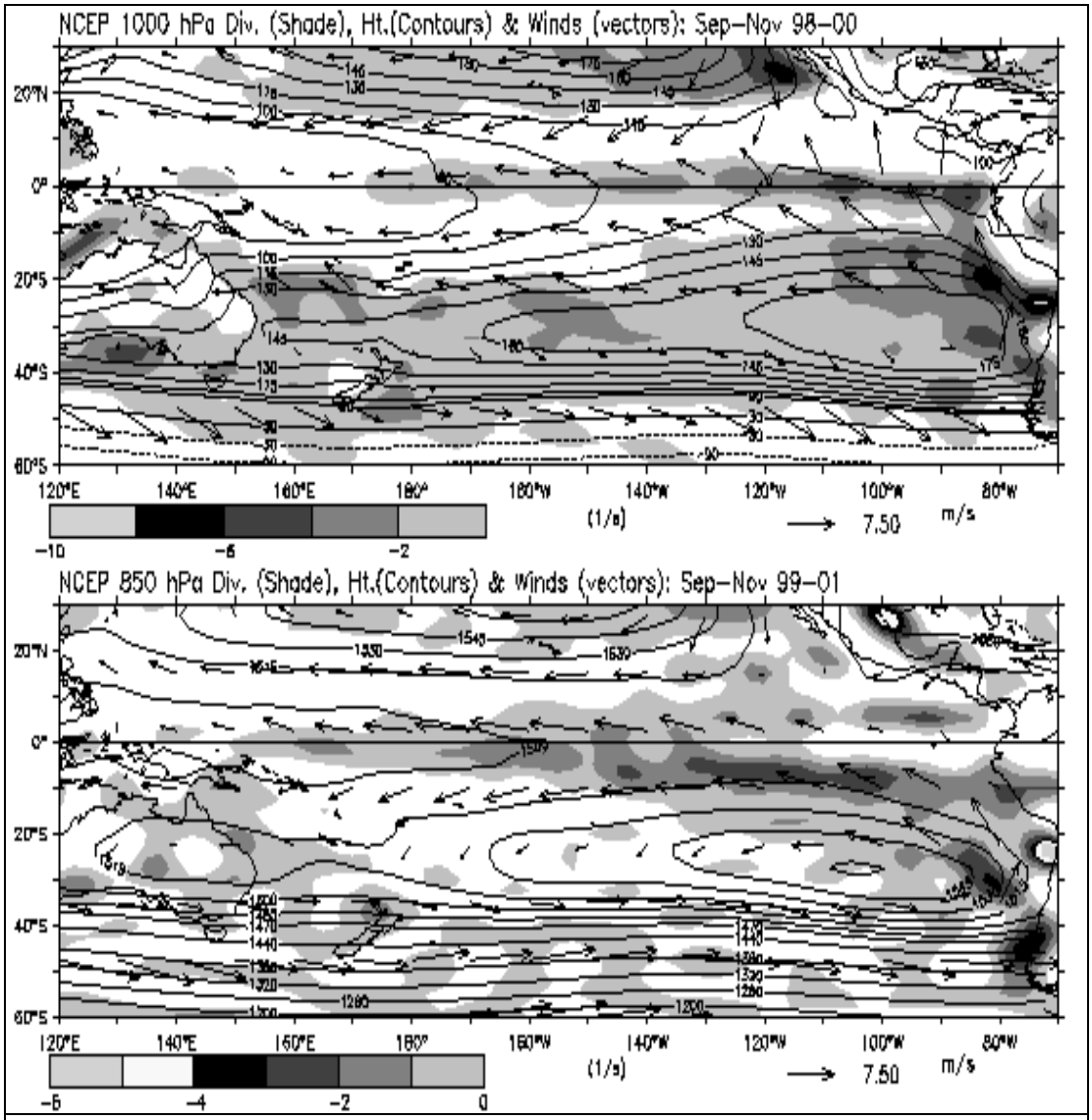

Figure 33: Same as figure 32 except for September through November.

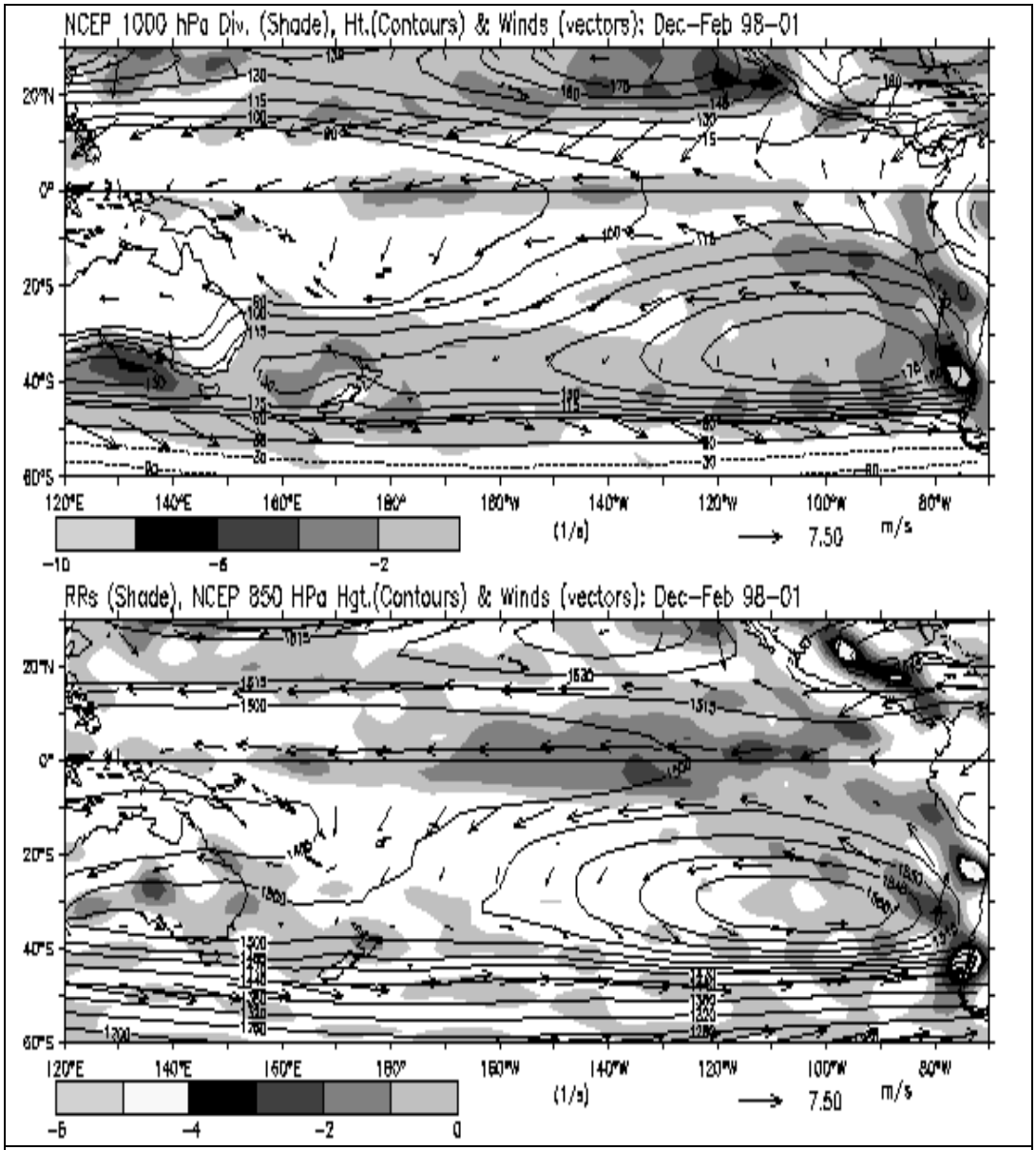

Figure 34: Same as figure 32 except for December through February.

rates (> 5mm/dy) are present. In the equatorial eastern South Pacific, convergence remains shallow and does not extend above 925 hPa throughout the seasons. Figures 32 through 35 show the seasonal distribution of NCEP height and divergence fields for the 1000 and 850 hPa levels.

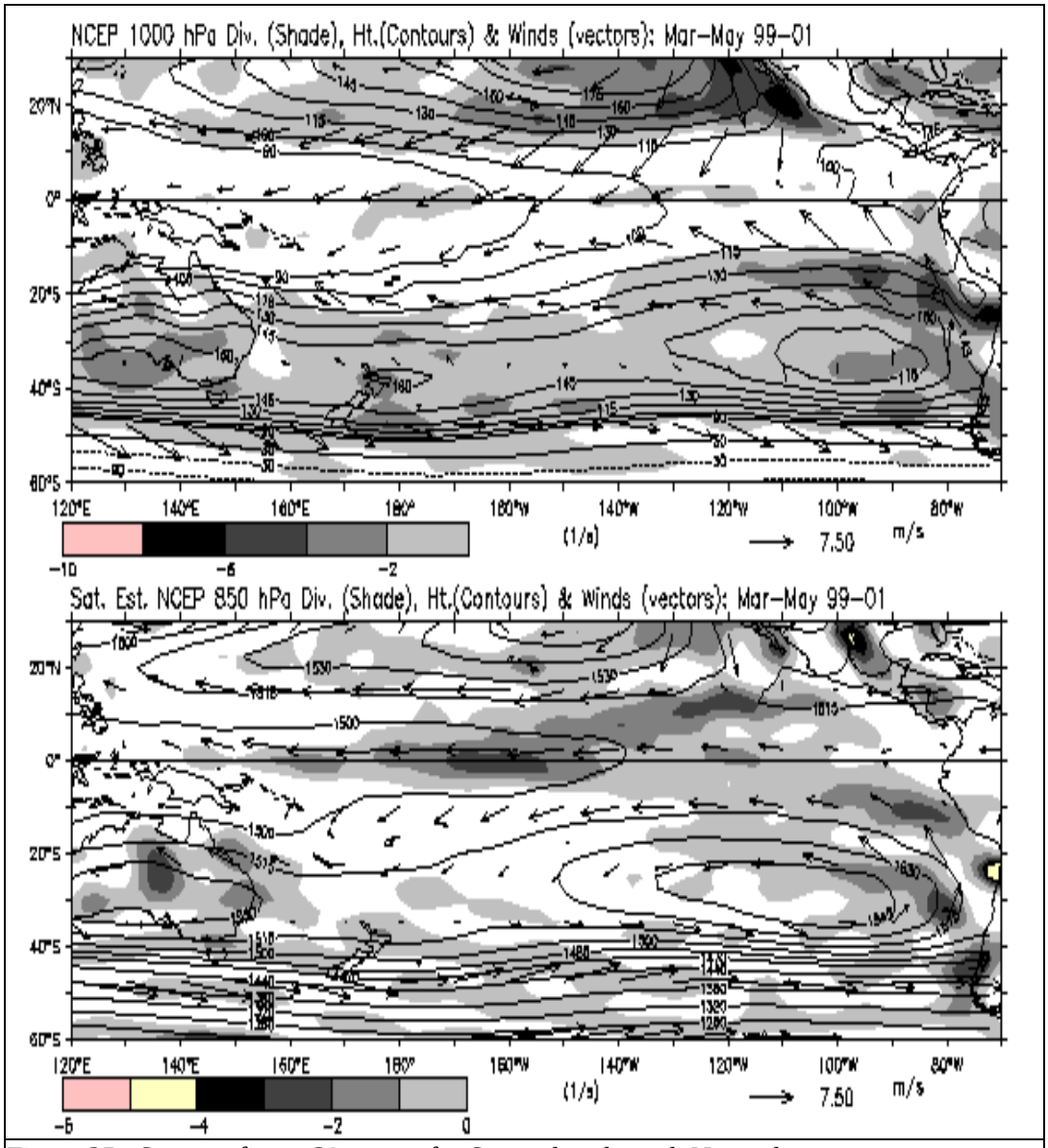

Figure 35: Same as figure 32 except for September through November.

Clearly, a large part of the 1000 hPa divergence at sub-tropical latitudes is associated with the sub-tropical ridge axis; at 850 hPa, the divergence becomes limited to the equatorward and poleward flanks of the ridge.

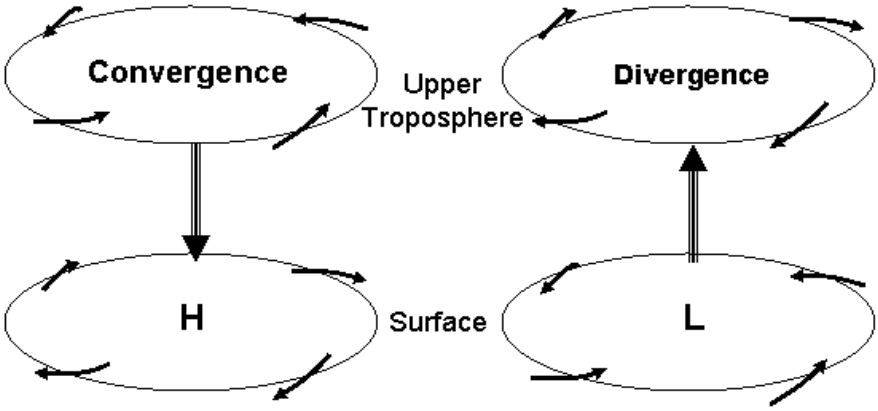

Figure 36: Schematic illustrating the effect of the surface on wind flow around high and low pressure areas. Large arrows denote vertical motion; small arrows denote horizontal flow.

There is a simple explanation for the difference in the distribution of convergence/divergence within the 1000 and 850 hPa layers. High pressure regions are formed by converging winds at upper levels; the convergence leads to sinking air. As it sinks towards the surface, the affect of the ground is to cause the air to blow across height lines as shown in figure 36. Therefore, divergence should be stronger along the ridge axis at the surface than at 850 hPa. This does not, of course, fully explain why low level ridging and divergence is present across the sub-tropical and mid-latitude portions of the SPCZ rain rate maximum during the various seasons. It is at this point where I must look at higher frequency data to better understand this phenomenon.

Seasonal Scatter Plots of Rain Rates and Divergence

In the previous section, I learned that the differences in the location of convergence axis at 1000 and at 850 hPa and the rain rate maximum are greatest during fall and smallest during summer. To better understand this observation seasonal analysis of scatter plots were examined using the same SPCZ test regions defined in chapter II. Summer and fall scatter plots of rain rate

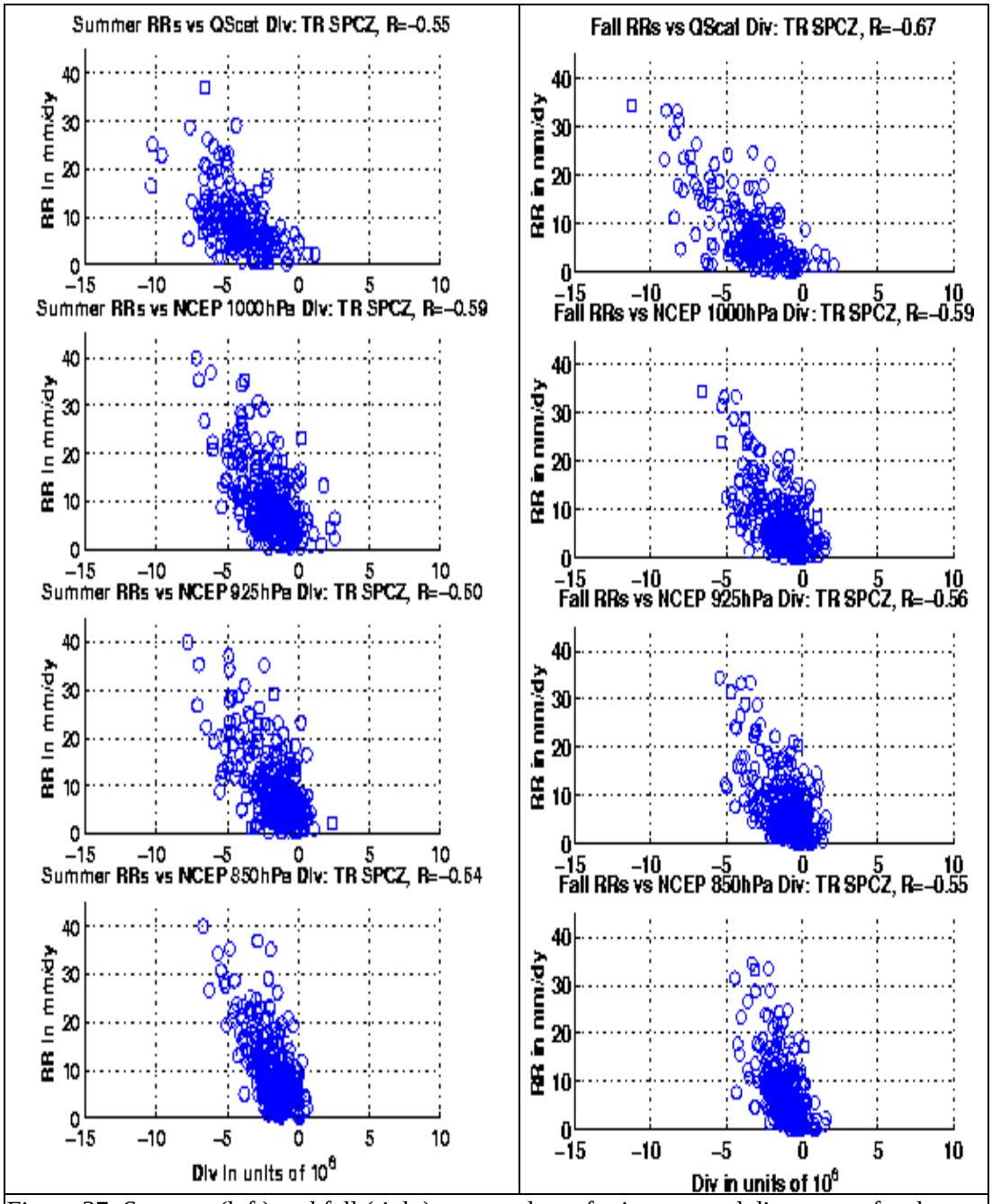

Figure 37: Summer (left) and fall (right) scatter plots of rain rates and divergence for the surface through 850 hPa layers of the TR SPCZ. 'R' denotes the correlation coefficient for each plot. The scatter plot using scatterometer data utilizes a two year data record, while the NCEP utilizes a three year data record.

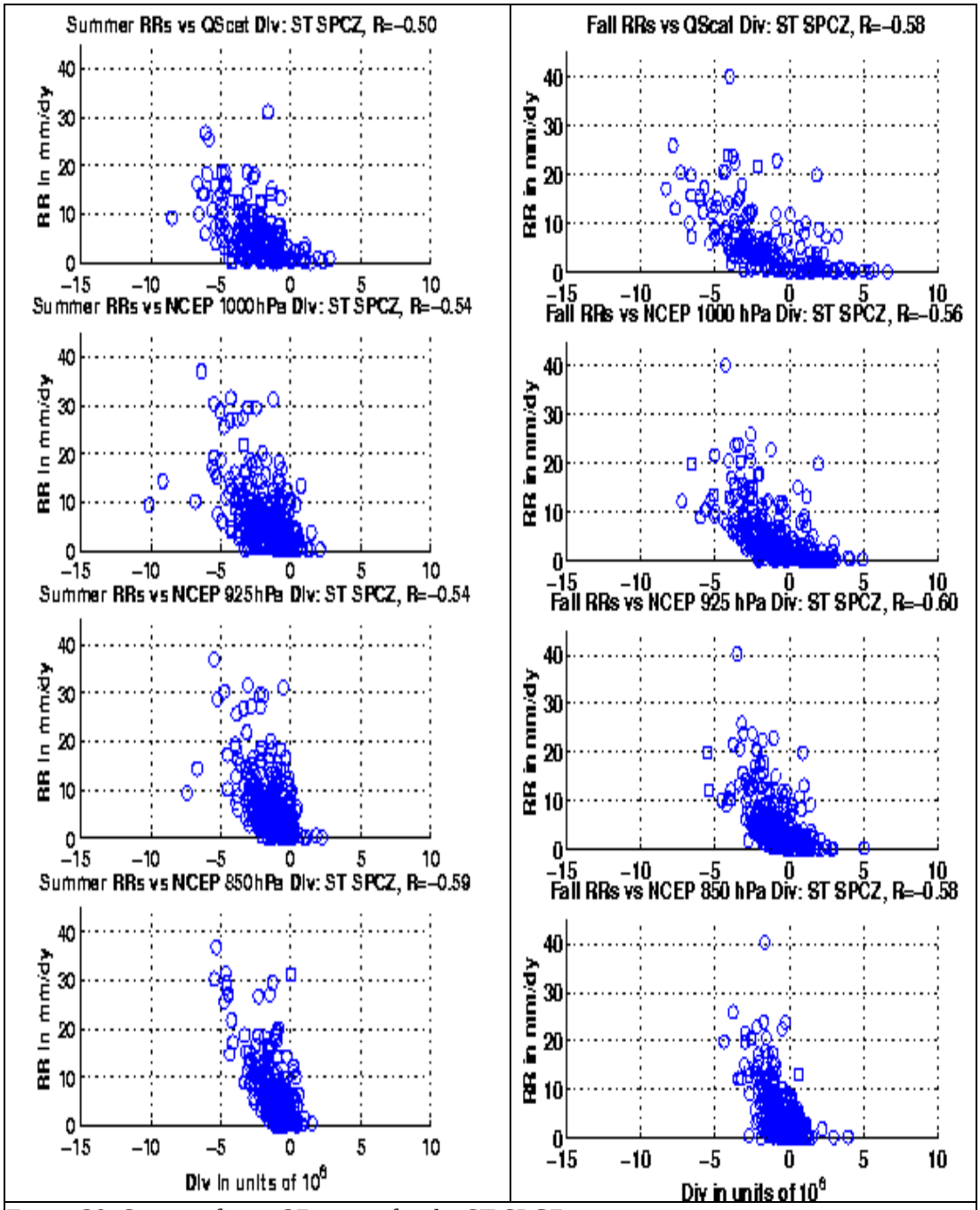

Figure 38: Same as figure 37 except for the ST SPCZ.

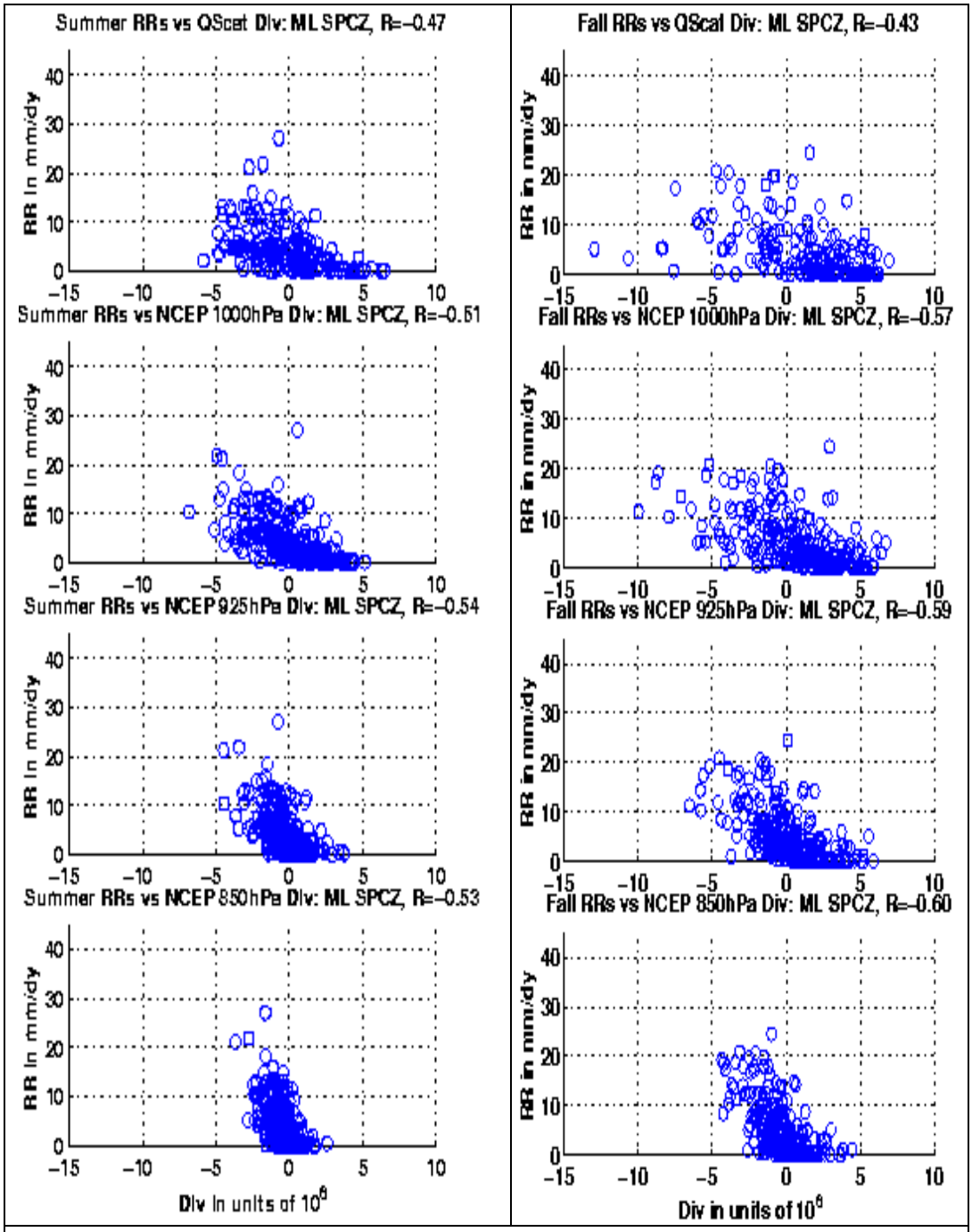

Figure 39: Same as figure 37 except for the ML SPCZ.

and divergence are shown in figures 37 through 39. Aside from the fact that the scatterometer data shows a higher correlation coefficient in fall, there is not much difference in the summer/fall

scatter plots over the TR SPCZ; whenever rain was present, convergence from the surface to 850 hPa was also present the vast majority of the time. The scatter plots over the ST SPCZ indicated a shift from rain days with surface convergence present throughout the boundary layer during summer to rain days with either surface convergence or divergence present in the fall. In the ML SPCZ, there are a number of rain days where divergence is present in both summer and fall. This shows that in the South Pacific, the higher in latitude one goes, the more often one finds rainfall where surface divergence is present at the surface. In most of the cases, rain days with surface divergence transitions to convergence at 850 hPa. Winter scatter plots (not shown) of the ST and ML SPCZ are similar to those seen in fall. It should be noted that the higher rain rate days in the ST and ML SPCZ, where values > 10mm/dy, were associated with convergence throughout the boundary layer.

These observations can be explained within the context of stratiform and convective rain associated with transient cyclones. To do this I need to briefly summarize the differences between convective and stratiform rain. Stratiform rain is defined as a precipitation process where vertical air motion is small compared to the fall rate of ice crystals, snow and small liquid drops; droplet growth via vapor diffusion, a slow process, is important for the development of this type of rain (Houze, 1997). Stratiform rain, as seen by radar, tends to take on a more layered, sheet-like appearance and is frequently accompanied by a bright band, a layer where melting ice/snow greatly increases radar reflectivity returns. On the other hand, convective rain is defined as a precipitation process where the vertical air motion is greater than or equal to the fall speed of ice, snow or drops. Strong updrafts cause rapid vapor condensation creating large concentrations of cloud liquid water (Houze, 1997). Growth of precipitation particles (liquid drops and/or ice) is dominated by collision and coalescence as well as by riming (Houghton, 1968), and rain typically develops very quickly within a cloud. Because of the high cloud liquid

water concentrations in concert with the vigorous updrafts within convective clouds and hence the rapid development of precipitation, convective rain typically has higher rain rates than stratiform rain. On radar, convective rain takes on an appearance of intense regions of rainfall whose vertical scale is larger than its horizontal scale.

Nearly all precipitation within the tropics is the product of atmospheric convection (Houze, 1997). Warm SSTs induce weak, but persistent low pressure and low level convergence and this combined with a conditionally unstable atmosphere results in the development of deep convection throughout the year. Cumuliform clouds tend to develop into distinct clusters of deep convection appropriately called “cloud clusters” (Frank, 1970; Mapes and Houze, 1993) where convective and stratiform rain is present. In mid-latitudes, precipitation is produced chiefly via extra-tropical cyclones (Houze, 1993) and is also stratiform and convective in nature. However, there are a variety of ways for precipitation to occur which do not necessitate near surface convergence. It is true that surface convergence, and hence convective rain, is often present along the surface boundaries of extra-tropical cyclones. However, large regions of stratiform with embedded meso-scale bands of convective rain may form behind or ahead of the frontal zones as shown by Houze (1993; his figure 11.22). These rain areas can develop in a variety of ways that are not related to localized surface convergence. For instance, aircraft observations of wide cold frontal rain bands along the western U.S. coast showed an absence of low level convergence; instead, rain clouds developed in regions of convergence two kilometers above the surface (Matejka, 1980). Therefore, surface convergence maxima may or may not coincide with rain rate maxima in the mid-latitudes. Surface convergence and rain rate maxima are more likely to coincide in intense cyclones, where large regions of strong low level convergence may be present for a number of days. This certainly applies to the few cases where

the area average rain rate for a test region was relatively high (> 10mm/dy) and therefore associated with convergence throughout the boundary layer.

Given the location of the storm track and the vertical wind shear maximum during fall and winter (as discussed in previous sections), it is likely that rainfall associated with extra-tropical cyclones is making a substantial contribution to the rain rate pattern in the mid-latitude portions of the SPCZ. It is also likely that the convergence and divergence distribution associated with extra-tropical cyclones is contributing to the peculiar convergence distribution at 1000 and 850 hPa. This idea can be extended into the ST SPCZ as well for scatter plots indicate this region to be a transition zone between the tropics and mid-latitudes in terms of the type of cyclones, tropical or extra-tropical, producing rain.

Summary

Seasonal analysis of NCEP re-analysis and satellite derived data during La Nina and neutral conditions yielded a number of interesting observations. One is that physical parameters such as SST, vertical wind shear, rain rates and convergence undergo different seasonal changes in the tropical as opposed to the sub-tropical/mid-latitude sections of the SPCZ rain rate maximum with some overlap occurring in-between at sub-tropical latitudes. Additionally, some of the seasonal changes that occur over the entire tropical South Pacific seem, at least circumstantially, related to the development of the SEITCZ in the eastern South Pacific. In light of this, I will summarize the seasonal evolution of the aforementioned physical parameters in the tropics, with an added emphasis on the development of the SEITCZ, and the sub-tropical/mid-latitudes of the SPCZ separately.

During winter in the Southern Hemisphere tropics, zonally oriented SST and convergence maxima are present and essentially co-located west of 145°W. In contrast, the tropical rain rate maximum extends eastward to 170°W and is closely associated with boundary layer

convergence and SST maxima in the region. In the eastern equatorial Pacific, a couplet of convergence and divergence straddles the equatorial cold tongue. The importance of this region to the development of the SEITCZ will become apparent in later seasons. Baroclinicity, as measured by the magnitude of the 200-850 hPa vertical wind shear, and the storm track, as measured by the variability in the meridional wind, is weak west of 160°W and slightly stronger to the east. This implies, as expected, that baroclinic systems are rare in the tropical, western South Pacific and only slightly more probable in the eastern longitudes.

During spring, the SPCZ tropical rain rate maximum has extended farther east and slightly southward with a portion of it extending into the sub-tropics. As in winter, the rain rate maximum does not extend as far east as the SST maximum and remains slightly poleward of the warmest waters. The SST and convergence maxima remain zonally oriented and are co-located a further distance eastward than in winter. As in the previous season, convergence is strong and present throughout the boundary layer west of 170°W. In the eastern equatorial South Pacific, the region of surface convergence has increased in value and spread further eastward and westward during this season. With the exception of the western coastal regions off of South America, baroclinicity is not significant.

Much of the SPCZ approximately zonally oriented rain rate maximum is located in the tropics (equatorward of 20°S) during summer. Much of this rain rate maximum continues to be characterized by strong convergence throughout the boundary layer of the atmosphere. Rain rate, surface convergence and SST maxima are all nearly co-located west of 170°W. East of this longitude, co-located surface convergence and SST maxima extend to near 130°W. In equatorial latitudes of the eastern South Pacific SSTs have warmed substantially and surface convergence stretched from the Western South American Coast to longitude 130°W. It is clear twin convergence maxima have developed in the tropical North and South Pacific. There is a region

of baroclinicity located along the equator in the central part of the Pacific Basin, although little rain is associated with it. Elsewhere, the baroclinicity and the position of the storm track indicate that baroclinic activity is not very important to the development of significant rain for the tropical rain rate maximum.

During fall, the highest rain rates are still located within the tropical regions. Zonally oriented rain rate, SST and surface convergence maxima are present and stretch across the entire South Pacific Basin. The result is twin ITCZ regions in the Northern and Southern Hemisphere tropics. The convergence in the eastern South Pacific remains shallow and confined below 850 hPa indicating the convection that occurs during this season is likely shallow. Baroclinicity in the tropical regions remain weak during fall.

The seasonal evolution of SSTs, rain rates, baroclinicity and convergence is substantially different at sub-tropical and middle latitude portions of the SPCZ. During winter and spring at these latitudes, an approximately zonally oriented rain rate maximum is present and is located over much cooler SSTs as compared to the tropical rain rate maximum. In winter, a northwest-to-southeast oriented zone of surface convergence extends from the western most end of the tropical convergence maximum into the eastern portion (east of 140°W) of the rain rate maximum at mid-latitudes. In this portion of the rain rate maximum, convergence is weakly present throughout the boundary layer; western sections of the rain rate maximum are characterized by surface divergence and 850 hPa convergence. During winter, baroclinicity is closely co-located with the storm track and both are directly located over the higher latitude SPCZ rain rate maximum. Clearly, this portion of the rain rate maximum is nothing more than the reflection of the Southern Hemisphere storm track during winter. In spring these patterns are still present, but in a weakened form. The mid-latitude rain rate maximum is weaker and equatorward of the surface convergence maximum. In turn, the surface convergence maximum

is narrower and weaker although it continues to extend into mid-latitudes; convergence at 850 hPa is also weaker. Baroclinicity weakens during spring as the storm track begins to shift poleward again; this coincides with the weakening of the higher latitude SPCZ rain rate maximum.

Only a small portion of the SPCZ rain rate maximum is present at sub-tropical and middle latitudes during summer. The portion that is present is located over a tight gradient in SSTs, and is characterized by surface divergence that transitions to convergence at 850 hPa. The northwest-to-southeast oriented diagonal of convergence that was present during winter and spring appears to have shifted equatorward into sub-tropical latitudes. Some baroclinicity is present over the sub-tropical and middle latitude portions of the rain rate maximum but it is substantially weaker than values found in winter and spring. The storm track is at high latitudes during summer.

During fall, the entire SPCZ rain rate maximum extends from the tropics to the mid-latitudes in a northwest-to-southeast direction. The portion of the rain rate maximum over the sub-tropical and middle latitudes are characterized by a tight gradient in SSTs and by surface divergence which transitions to 850 hPa convergence. Baroclinicity is stronger during fall and is located directly over the sub-tropical and mid-latitude portions of the SPCZ rain rate maximum. The storm track has shifted equatorward into the sub-tropical and mid-latitude portions of the SPCZ rain rate maximum. This suggests that baroclinic cyclones may be important to this region of the SPCZ during fall.

All of the results from this chapter strongly suggest that the SPCZ is actually composed of two distinct dynamical regions: a tropical section dominated by low vertical wind shear and a higher latitude section where strong vertical wind shear and surface divergence that transitions to convergence at 850 hPa are dominate. The strong vertical wind shear is indicative of baroclinic

activity while the surface divergence in the rain rate maximum is indicative of rain being created by convergence above the surface. It is well documented that extra-tropical cyclones produce rainfall that is associated with both surface and above surface moisture convergence (Matejka, 1980).

To better understand the relationship between rain rates and divergence, scatter plots of these parameters were examined for summer and fall, the two seasons where the greatest differences between surface and 850 hPa convergence distributions were present. In tropical sections of the SPCZ, rain days with convergence from the surface to 850 hPa were common in both summer and fall. Only in the sub-tropical and mid-latitude parts of the SPCZ were seasonal differences noted. In both regions, there is a significant increase in the number of days with rain and low level divergence is present. This finding implies that during fall extra-tropical cyclones, with regions of rain related to both surface and above surface convergence, are providing a large amount of the rainfall in this region of the SPCZ.

Finally, there appears to be a circumstantial link between the tropical sections of the SPCZ and the development of the SEITCZ. The band of rain that developed over the equatorial Southeast Pacific during fall is the SEITCZ, and its development coincided with the equatorward and eastward extension of the surface convergence and SST maxima from the tropical sections of the SPCZ into the eastern equatorial South Pacific.

CHAPTER V

LAG CORRELATION ANALYSIS

Introduction

In the last chapter, seasonal analysis indicated the rain rate maxima in the tropical and mid-latitude sections of the SPCZ peak at different times of the year. This suggests the two regions maybe dynamically independent of each other. Low vertical wind shear over the tropical SPCZ suggests an equivalent barotropic type of atmosphere while stronger shear in the mid-latitude sections suggests a baroclinic atmosphere. Seasonal scatter plots of rain rate vs. surface divergence suggest the ST SPCZ to be a transition point between the TR and ML SPCZ. In this case, I use the word 'transition' to indicate that cyclones producing rain in this region may have a mixture of tropical and extra-tropical characteristics. Therefore, the climatological SPCZ rain rate pattern, which stretches from the tropics to the middle latitudes, is partly due to changes in the position of the mid-latitude storm track during the different seasons and to atmospheric heating caused by off-equatorial tropical convection as suggested by observations and numerical simulations from Gill (1982), Vincent (1982) and Kodama (1992, 1993 and 1999). There are still a number of questions that need to be answered. How related are different sections of the SPCZ to each other at higher frequencies, that is on time scales of synoptic weather phenomena? Does convection tend to develop within a given section of the SPCZ and propagate southeastward into other sections, or does it tend to dissipate in place? In other words, is the rain rate pattern better characterized as repeated, short lived rain events over different sections of the SPCZ or as rain events that stretch over great distances and last for a number of days? Additionally, what is the role of upper level mid-latitude troughs towards the development of the SPCZ rain rate maximum? Figure 40 is a schematic used to illustrate these questions; to

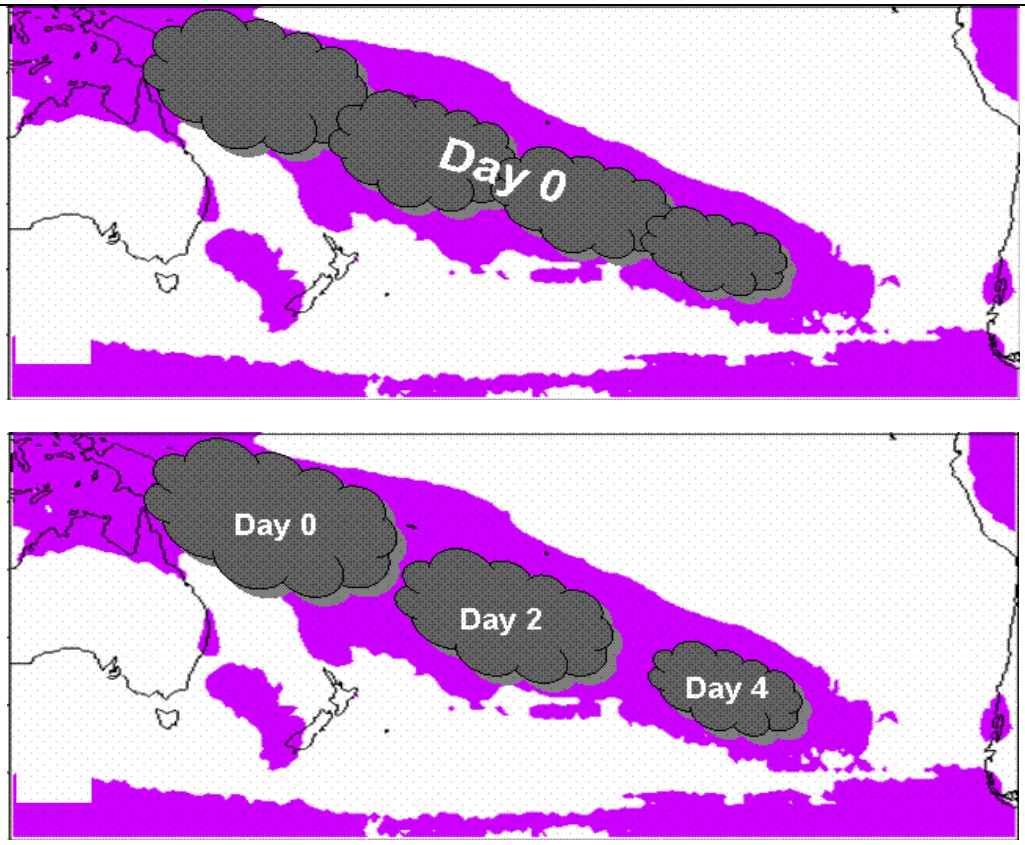

Figure 40: Two conceptual ideas illustrating how the SPCZ becomes convectively active for a given time period. Top is scenario where convection develops along a band stretching from the tropics to the mid-latitudes; "Day 0" is used to indicate the near simultaneity of the band. Bottom scenario illustrates that only portions of the SPCZ become convectively active at a given time. Dark clouds represent convection while shade is the three year average of rain rates ≥ 3mm/dy.

examine them will require looking at filtered data with periods of approximately one month. Lag correlation analysis can give information on the spatial and temporal scale of the rainfall in the SPCZ, as well as the importance of upper level troughs and jet streaks to the development of rain. Lag correlation analysis is used to help answer the aforementioned questions and is discussed in this chapter.

Correlation Analysis Methods

The correlation coefficient can be calculated using the relation:

$$R = \Sigma(X_i - X_{avg})(Y_i - Y_{avg})/(\sigma_x * \sigma_y) \quad (9)$$

where the 'avg' sub-script denotes the variable average, 'i' the ith observation and σ the standard deviation. Almost all practical methods for testing the significance of a correlation coefficient require data to be normally distributed. As discussed in chapter II, wind and height anomalies are not strictly normal but the deviations are such that the assumption of normality is not seriously affected. However, daily rain rate data is highly non-normal and remains so even after attempts are made to convert it to a normal distribution. This presents a problem with determining the significance of a correlation. However, if the signal is strong, a coherent pattern exists and there is some physical justification for the results, I can have some confidence that the correlation is correctly capturing the relationship between the two variables. With this in mind, cross-correlation analysis was accomplished using satellite derived rain rates and NCEP 200 hPa height and wind fields. Test regions used are the same ones described in chapter II.

A simple correlation test can be accomplished by creating an average value for a physical parameter (such as rain rates) over a test region, and, using equation 9, correlate it with the values of the same or another parameter for gridpoints across a given domain. This would give the instantaneous correlation coefficient between the two physical parameters. However, I am interested in understanding if a relationship exists between these parameters over both a spatial and temporal domain. This requires adjustments to equation 9:

$$R = \Sigma(X_t - X_{tavg})(Y_{t+1} - Y_{tavg})/(\sigma_{xt} * \sigma_{yt}) \quad (10)$$

$$R = \Sigma(X_t - X_{tavg})(Y_{t-1} - Y_{tavg})/(\sigma_{xt} * \sigma_{yt}) \quad (11)$$

where the '$\mathbf{X_t}$' denotes the variable X at time 't', '$\mathbf{Y_{t+1}}$' and '$\mathbf{Y_{t-1}}$' the variable 'Y' at time 't+1' or 't-1', '$\mathbf{X_{tavg}}$' and ' $\mathbf{Y_{tavg}}$' the time averages, '$\boldsymbol{\sigma_{xt}}$' and '$\boldsymbol{\sigma_{yt}}$' the standard deviation of variables 'X' and 'Y.' Equation 10 is used to determine the correlation coefficients at forward time lags while 11 is used to determine the correlation coefficients at backward time lags. In order to use

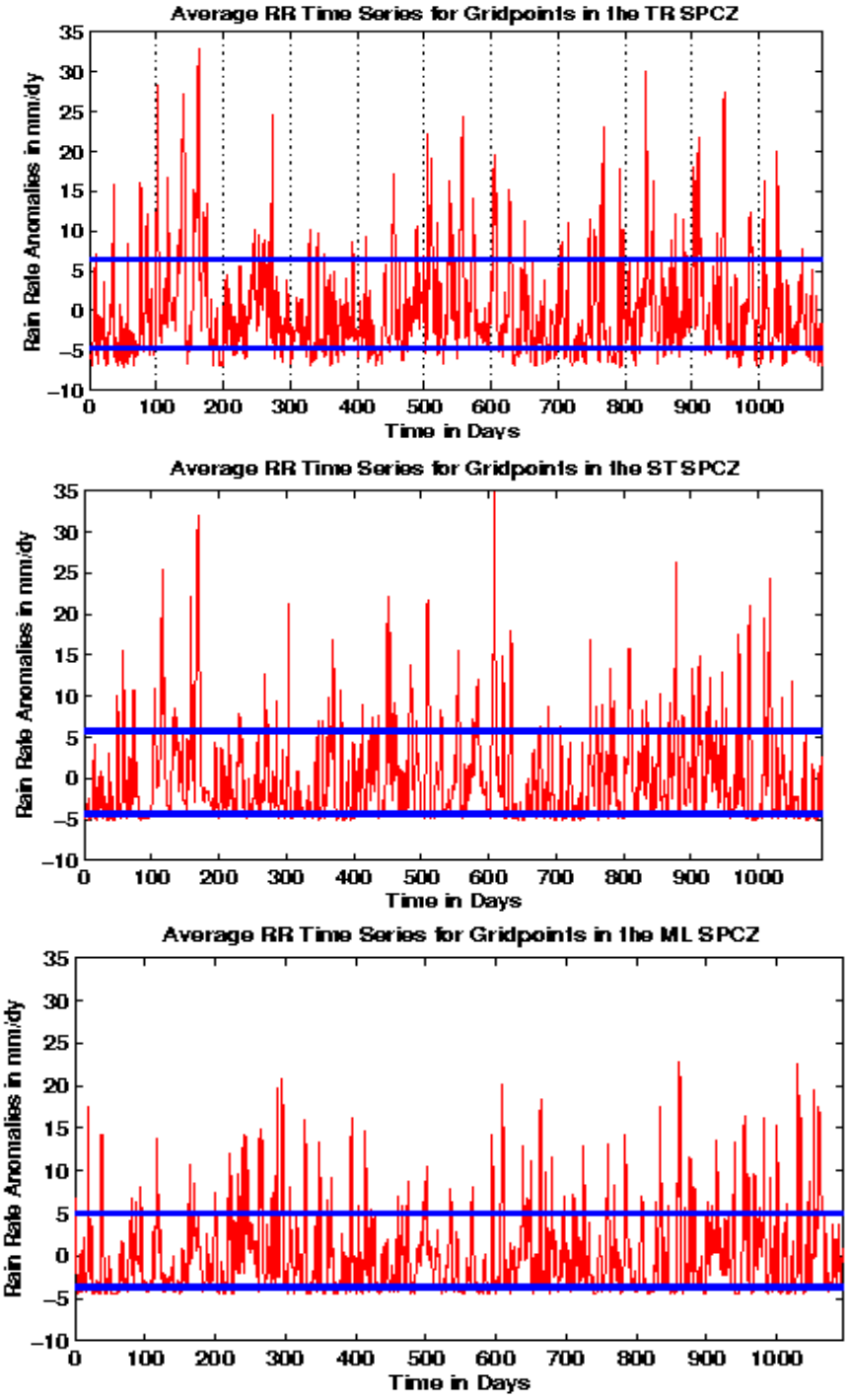

Figure 41: Average rain rate time series for gridpoints in the TR, ST and ML SPCZ test regions. The blue lines denote the first standard deviation (top) and the 0.75 of the first standard deviation (bottom). As noted previously, the distributions are skewed toward positive anomalies, a common characteristic of daily rainfall data.

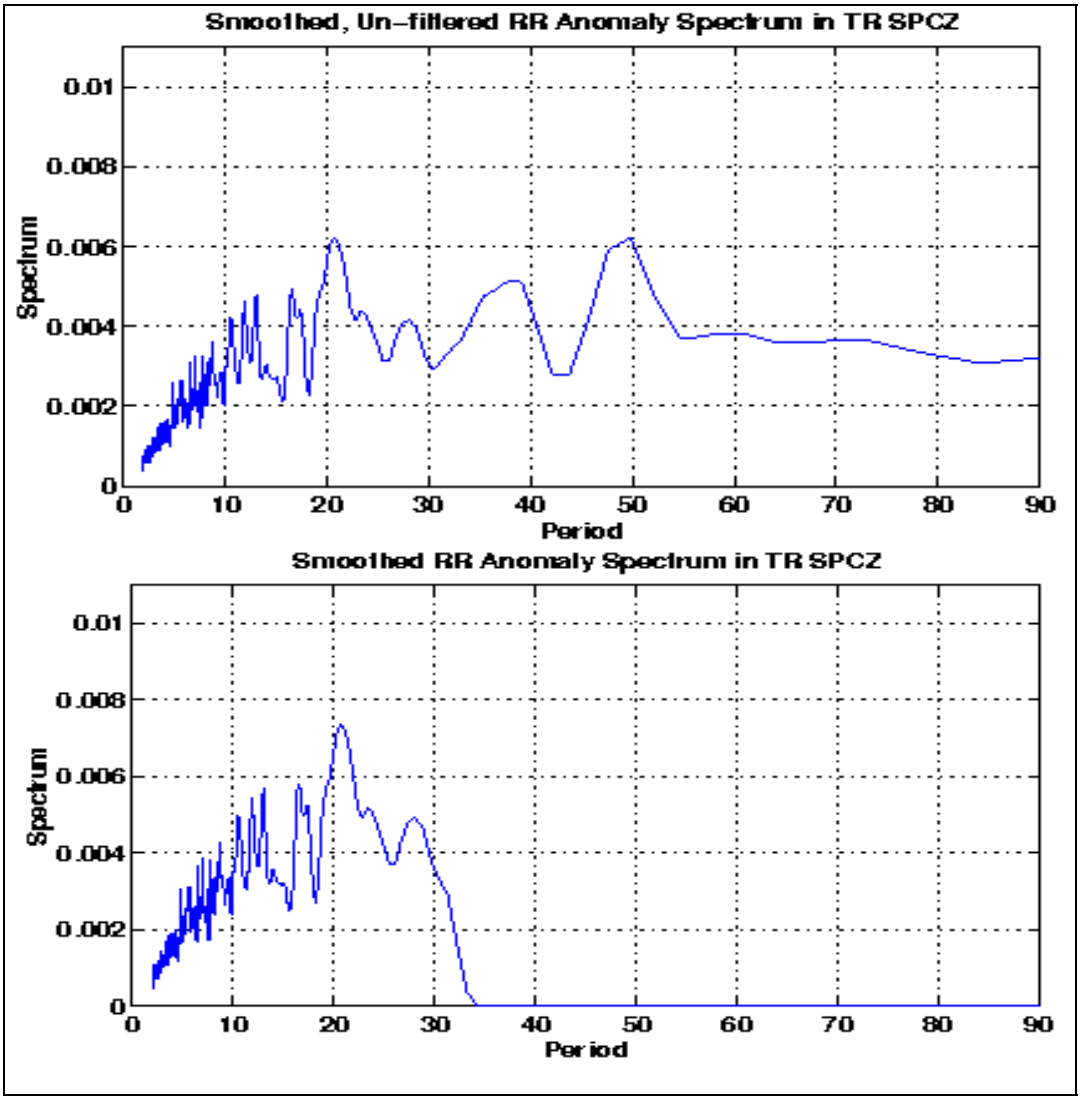

Figure 42: Normalized spectra of satellite derived rain rates for the TR SPCZ region. Note there are slight differences in the magnitudes of peaks in the two graphs due to differences in the normalization by variance of the unfiltered, whose variance is the sum of all oscillations, and that of the filtered data, whose variance is the sum of oscillations < 34 days.

equations 10 and 11, an averaged time series for a given variable must be created for all of the gridpoints within a given SPCZ test region and examples of this are shown in figure 41. Next, time series must be created for each gridpoint within the domain of the correlation test. However, using equations 10 and 11 to determine correlation coefficients for large data sets can

be very computer intensive. Additionally, I wish to remove annual, semi-annual, seasonal and intra-seasonal oscillations. To do this, I will use Fourier analysis to remove low frequency oscillations from the data followed by the calculation of the correlation coefficients at different time lags. A complete discussion of the Fourier analysis is included in the appendix at the end of the dissertation. Once correlation vectors are calculated, computer programs are used to compare different autocorrelation functions and to isopleth the spatial distribution of correlation coefficients between a pair of variables for a given time lag.

Spectra and Auto/Cross Correlation of Rain, Height and Div. within the SPCZ

An example of a spectrum is shown in figure 42 for rain rates in the TR SPCZ region. The top figure shows the normalized (by variance), unfiltered spectrum after it had been smoothed by a weighting function. The bottom figure shows the same smoothed spectrum after lower frequency oscillations, with periods > than ~ 1 month filtered out. It is clear that there is much information at seasonal and intra-seasonal time scales. However, we have already examined seasonal time scales in chapter IV and now we wish to view information pertaining to the development of the SPCZ rain rate maximum at higher frequencies.

Figure 43 contains the smoothed and filtered rain rate spectra for the TR, ST and ML SPCZ. Much of the power of the spectra is concentrated in oscillations of 15 to 30 days; there are many oscillations with periods less than 10 days but they contain little power. Some of the strongest peaks in power are found in frequencies with periods of 20 to 25 days. Kiladis and Wieckmann (1992a) and Schrage and Dayton (1996) also noted peaks in the power spectra of OLR data, a proxy for convection, for frequencies with periods in the 21- 24 day range in the tropical and sub-tropical portions of the SPCZ. The reader may ask why study the high frequency oscillations, for example, phenomenon at synoptic time scales, should be examined when more power lies between 15 and 30 days? First, investigators have already conducted studies on this

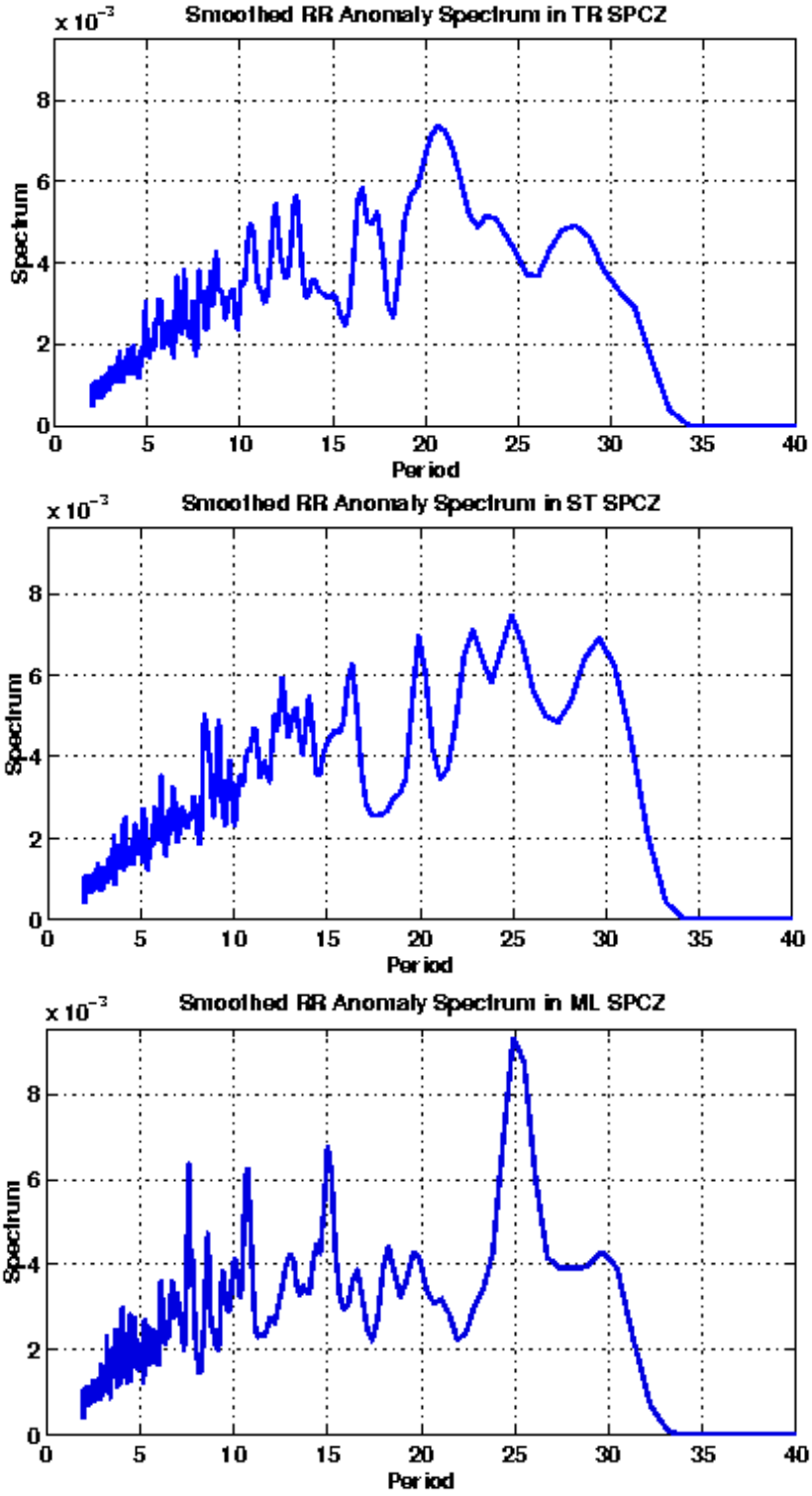

Figure 43: Normalized, smoothed spectra of satellite derived rain rates for the TR, ST and ML SPCZ.

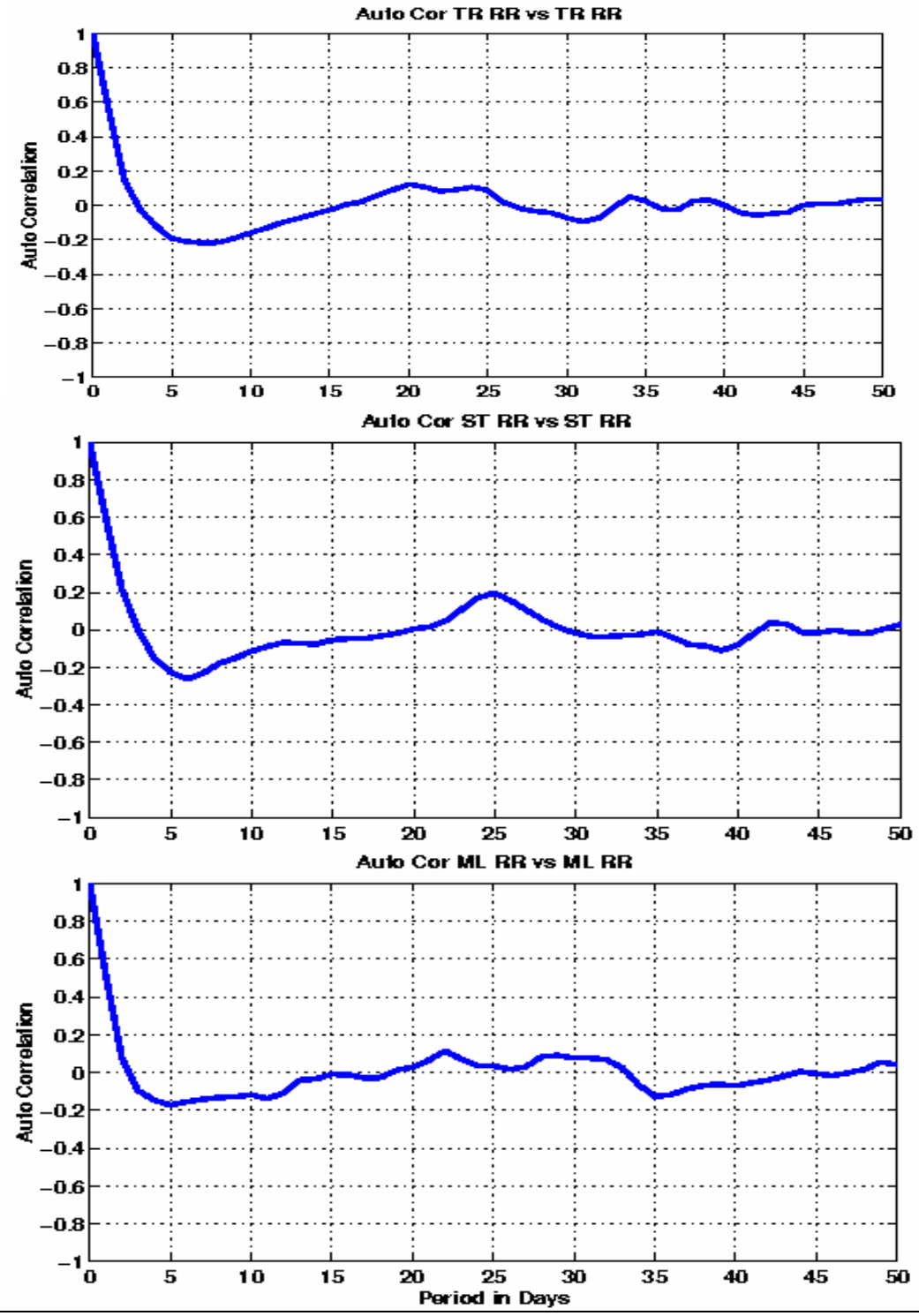

Figure 44: Auto-correlation functions for rain rate anomalies in the TR, ST and ML SPCZ.

and other lower frequency bands (Kiladis and Wieckmann (1992a) and Schrage and Dayton (1996)). I am interested in the day to day synoptic scale phenomenon. It is true that the low frequency oscillations will either act to amplify or suppress the potential for rain associated with the higher frequency synoptic scale waves. Nonetheless, I still want to investigate higher frequency phenomenon for it is these events that produce the rain which, in the aggregate, leads to the climatological SPCZ rain rate maximum. For the rest of this chapter, all data will have low frequency oscillations, with periods > ~ one month, filtered out prior to analysis.

Figure 44 shows the auto-correlation functions for the average rain rate in the TR, ST and ML SPCZ. In each case, the auto-correlations go to zero rather quickly and thereafter maximum values are less than 0.25. This means the time scale for rainfall within a given section of the SPCZ is short and generally less than three days. Figure 45 shows the cross-correlation between rain rates in one section of the SPCZ to other sections and coefficient magnitudes are even smaller with values ≤ 0.20. This indicates that rainfall in the different sections of the SPCZ, at least for three years of data, is not well related. Figure 46 shows the auto-correlation functions for 200 hPa height anomalies and as is very similar to figure 44 as coefficient values drop to zero fairly quickly. The zero crossings indicate the time scale for 200 hPa heights are around four days in the SPCZ. It should be noted, however, that some of the correlation coefficient magnitudes after the zero crossing are higher than those observed in the rain rate auto-correlation functions. In the TR SPCZ, for example, the correlation coefficient reaches a minimum of 0.38 at lag day 10. This means that there is a distinct oscillation with a period of ten days in the 200 hPa heights within this SPCZ region. Generally, correlation coefficient magnitudes are ≤ 0.25 after the zero crossing. The cross correlation coefficients for 200 hPa heights in one part of

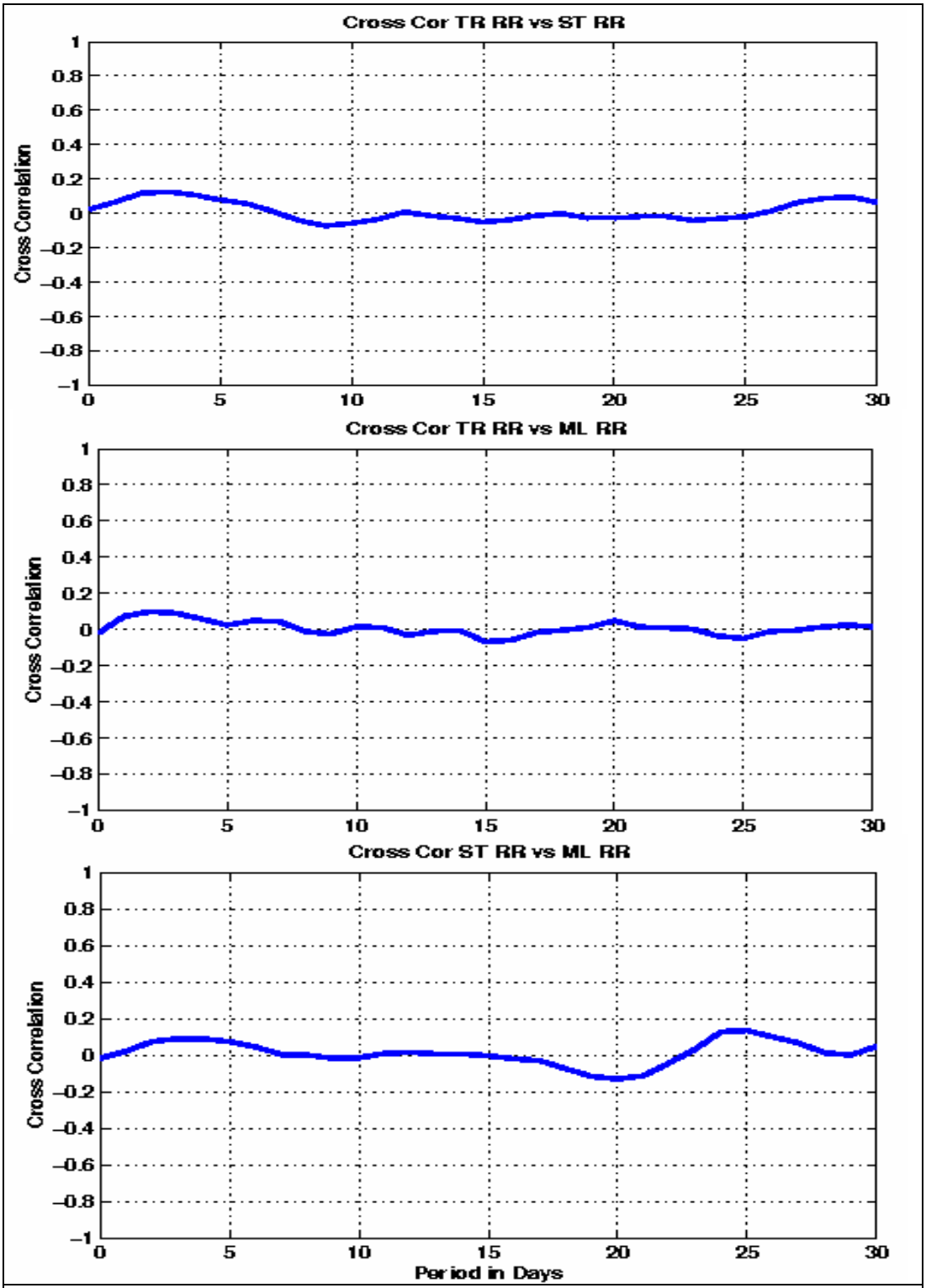

Figure 45: Cross-correlation functions between rain rate anomalies in one section of the SPCZ with rain rates in another SPCZ section.

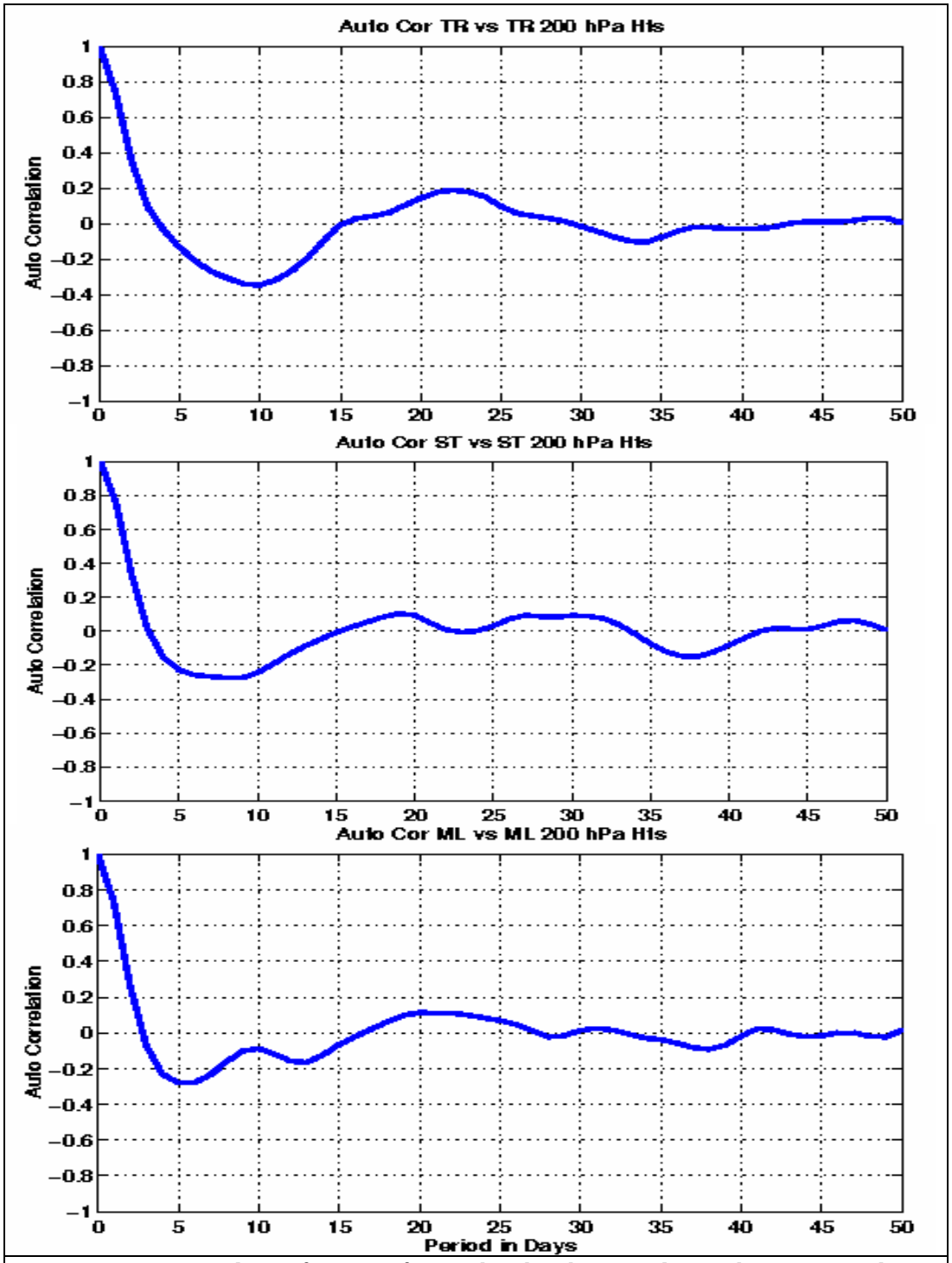

Figure 46: Auto-correlation functions for 200 hPa height anomalies in the TR, ST and ML SPCZ.

the SPCZ to another is very similar to figure 45 and are not shown for brevity. This means that, on average, 200 hPa height anomalies in one section of the SPCZ are poorly related to those in other SPCZ regions. As a further check, cross correlations of rain rates in one section of the SPCZ to 200 hPa divergence in another were examined and are shown in Table 1. There is a good relationship between rain rates and 200 hPa divergence in the same section of the SPCZ with correlation coefficients > 0.60. However, the correlation drops off dramatically, to zero in some cases, when rain rates in one SPCZ section were correlated to upper level divergence in another. Clearly, for the majority of the time the different SPCZ regions are only poorly related to each other.

Table 1: Correlation of rain rates vs. 200 hPa divergence for different combinations of the TR, ST and ML SPCZ using a three year period.

Corr. RRs vs 200 hPa Div	TR SPCZ Div.	ST SPCZ Div.	ML SPCZ Div.
TR SPCZ RRs	0.63	~0	~0
ST SPCZ RRs	~0	0.66	-0.15
ML SPCZ RRs	~0	-0.15	0.68

Lag Correlation Using Rain Rate Anomalies

Using the time scales derived from auto-correlation functions, I can conduct lag correlation analysis to see how correlation maxima and minima propagate with time in the SPCZ region. Lag correlation analysis using daily rain rates were completed for each test region at lag days -5 through +5. However, coherent patterns, in general, were visible only for lags -2 through +2 days and these are shown in figures 47 through 49. For each SPCZ region, positive, elliptically shaped correlation patterns are present, the strongest occurring, as expected, at lag day 0. There are only weak negative correlations in the analysis and this is likely due to the skewed data distribution. It is noted that for the TR SPCZ correlation maps, there is a very weak (~0.10) pattern that is reminiscent of the climatological SPCZ rain rate maximum at lag day +2. This

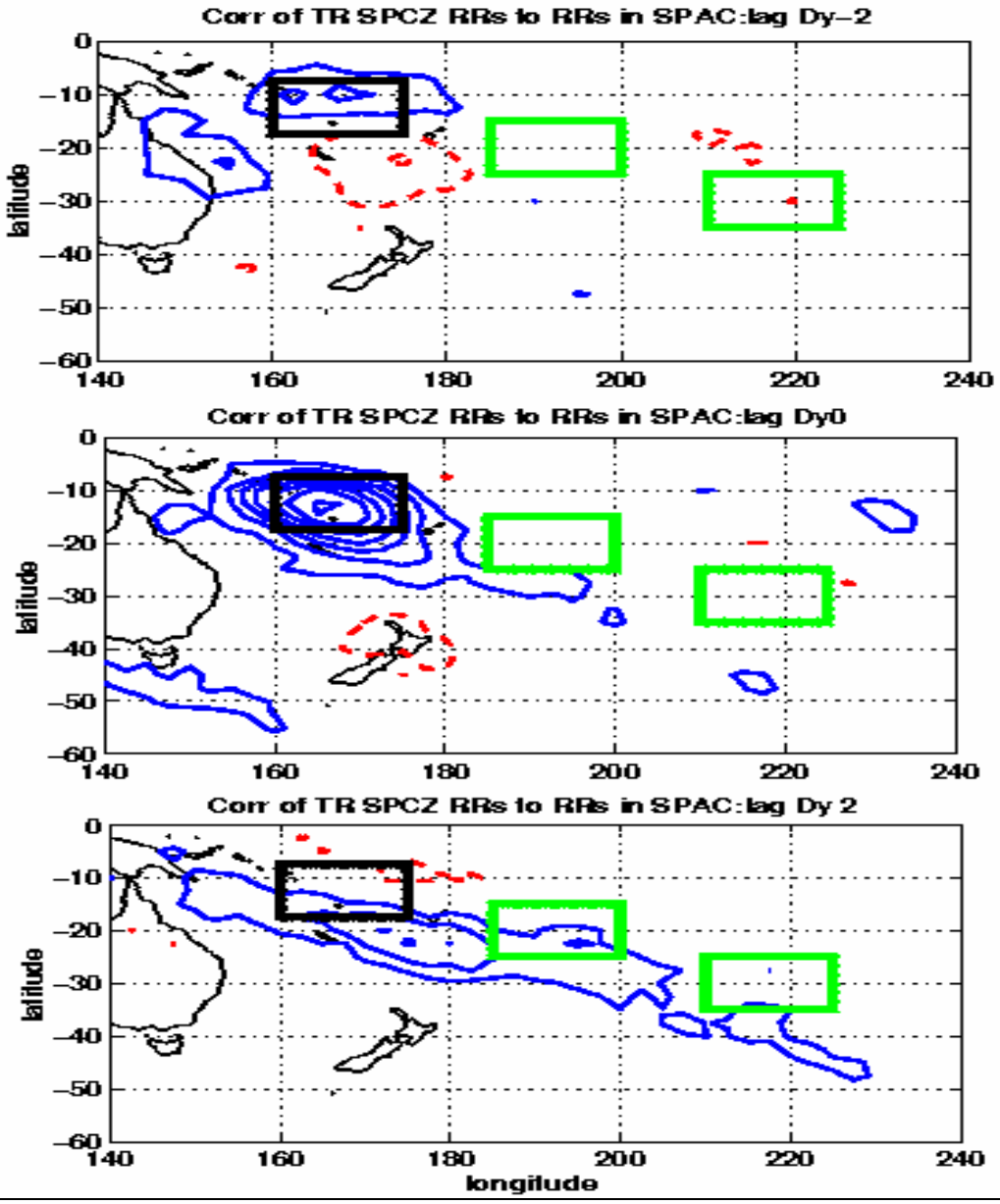

Figure 47: Backward and forward lag correlation results of rain rates within the TR SPCZ test region (black box) with the rest of the South Pacific. Each solid and dotted contour begins with the value 0.1 and is incremented by 0.1. The base region is denoted by the black rectangle and the zero contour has been omitted.

pattern does extend into portions of the ST and just south of the ML SPCZ regions at lag day +2. However, the strongest correlations, values ≥ 0.3, remain closest to the TR SPCZ. For the ST SPCZ maps, some positive correlations are seen entering the western portion of the ML SPCZ at

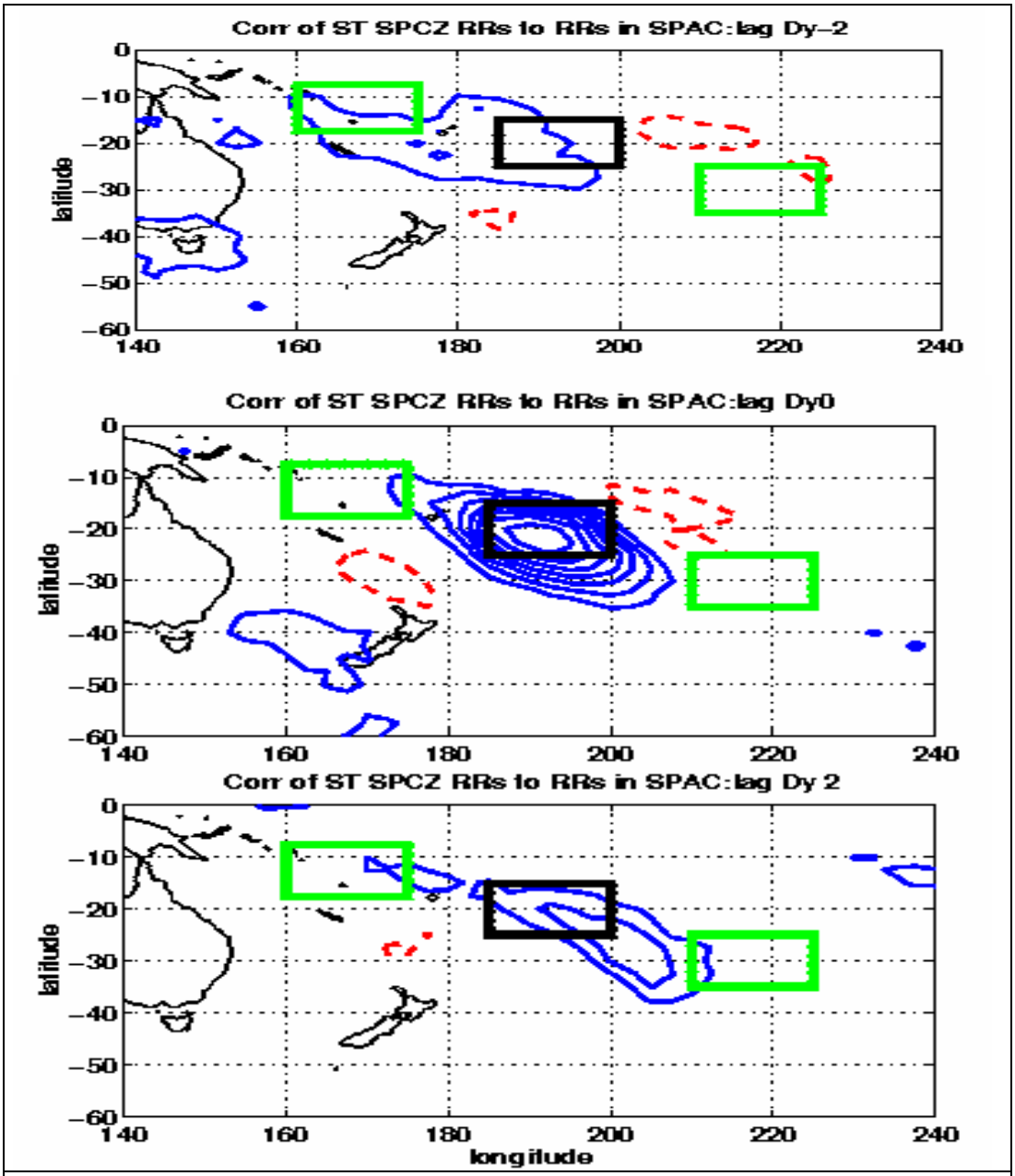

Figure 48: Same as figure 47 except for the ST SPCZ.

lag day +2; but at lag day +3 (not shown) the correlation pattern has dissipated. For the ML SPCZ correlation maps, a correlation maximum can be seen leaving the eastern edge of the ST SPCZ region on lag day -2. This maximum does move into the ML SPCZ region on lag day 0. These results indicate that there is a weak relationship between rain rates in adjacent

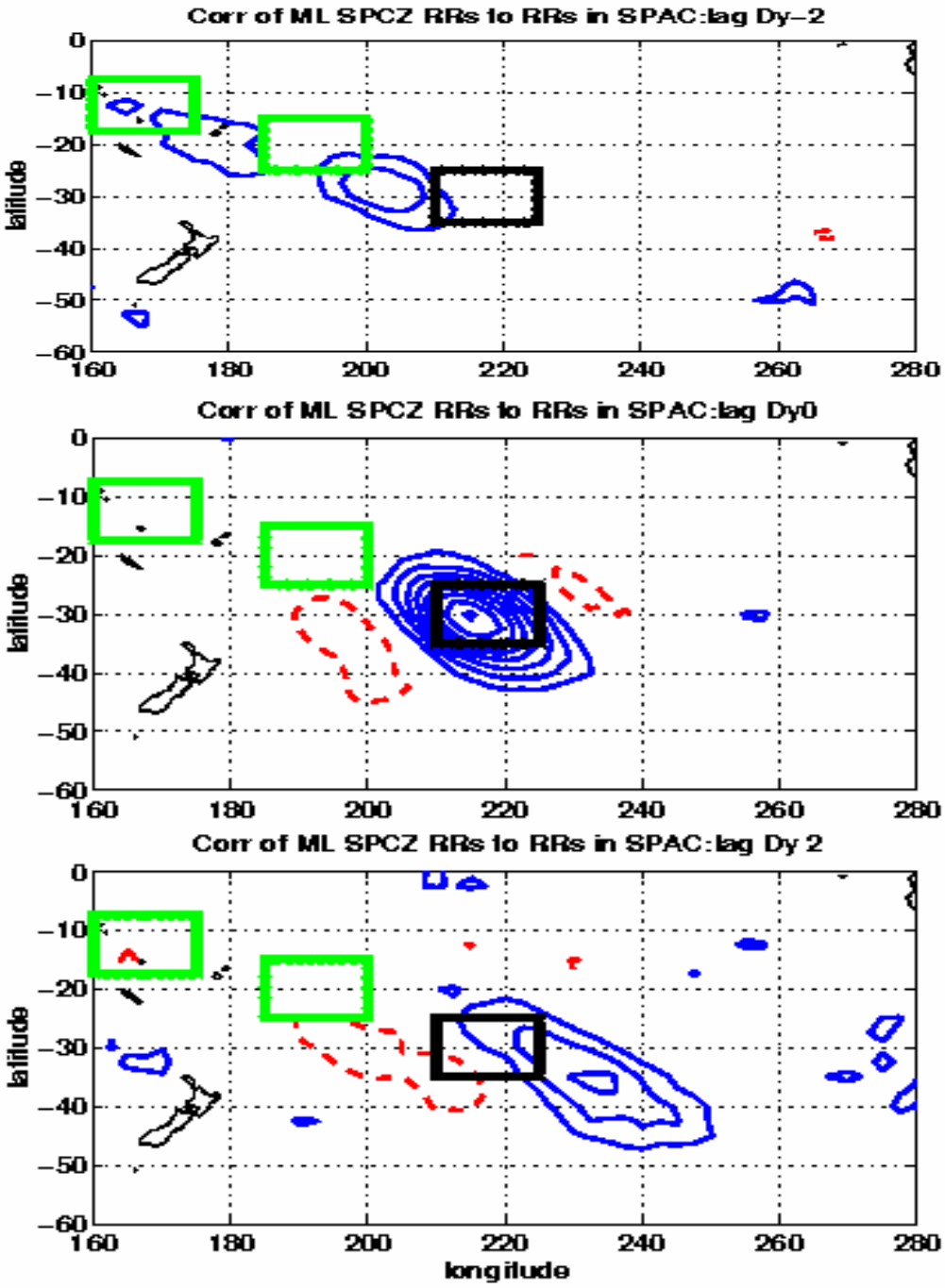

Figure 49: Same as figure 47 except for the ML SPCZ.

sections of the SPCZ and this confirms what was seen in the cross correlations from figure 45. On the other hand, rain rates in the TR and ML SPCZ are almost completely independent of each

other in terms of the statistics. This may not be the case for high rain rate events which is left for discussion in the next chapter.

The size of the semi-major axis for the dominant (i.e., the strongest) correlation maximum at lag day 0 ranged from 3500 km in the ML SPCZ to 4800 km in the ST. The phase speed of the dominant maximum in the TR and ST SPCZ for lag day 0 was ~ 5.4 m/s in a east-southeastward direction. In the ML SPCZ, the dominant maximum moved in an east-southeastward direction at 8 m/s. The distance traversed ranged from 600 km in the TR and ST to 850 km in the ML SPCZ. Assuming the skewed rain rate distribution has not prevented stronger patterns from appearing, the results suggest that convection tends to develop close to or within a given section of the SPCZ and does not propagate far from it.

Lag Correlation Using Rain Rate and Divergence Anomalies

Next, rain rates in a given region of the SPCZ were correlated with middle to upper level divergence in the South Pacific. I evaluated a number of middle and upper pressure levels because the location of the tropopause and therefore the level of maximum divergence is, in general, a function of latitude and season. For example, the tropopause may be around 100 hPa while in Antarctica it may be as low as 500 hPa. Obviously, the maximum divergence is located below the level of the tropopause; therefore I correlated rain rates in the TR, ST and ML SPCZ with divergence at 200, 300, 400 and 500 hPa in the South Pacific. In each case the strongest correlation signals are found using the 200 hPa pressure level in the TR and ST SPCZ and the 200 and 300 hPa levels in the ML SPCZ. Therefore, I show only the correlation results using the 200 hPa divergence in figures 50 through 52. Here, I note that positive maxima may be due to positive rain rate anomalies correlated with divergence or negative rain rate anomalies correlated with convergence. Negative correlation minima may be due to positive rain rate anomalies correlated with convergence or negative rain rate anomalies correlated with divergence. The

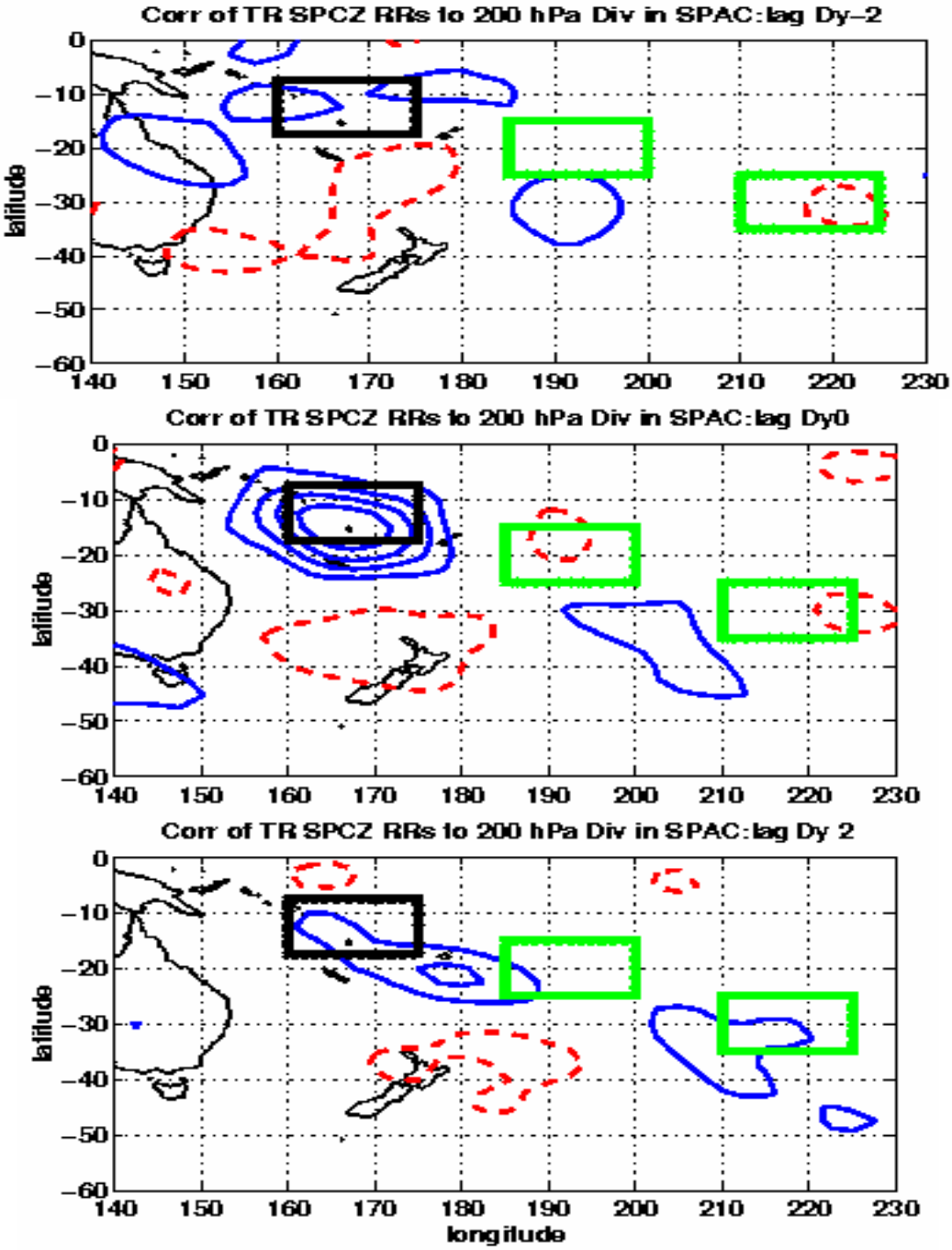

Figure 50: Backward and forward lag correlation results of rain rates within the TR SPCZ test region (black box) with 200 hPa divergence across the rest of the South Pacific. Each solid and dotted contour begins with the value 0.1 and is incremented by 0.1. The base region is denoted by the black rectangle and the zero contour has been omitted.

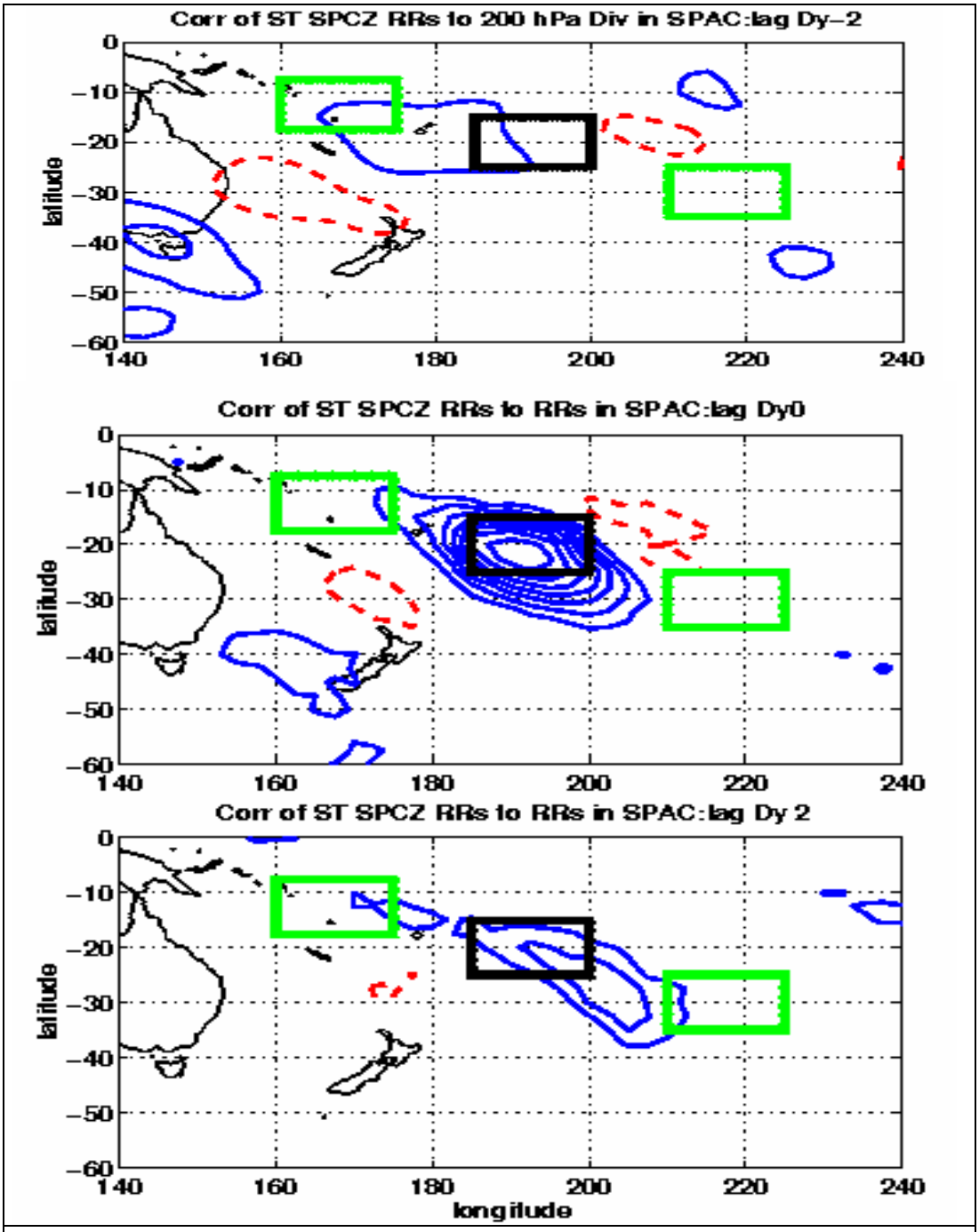

Figure 51: Same as figure 50 except for the ST SPCZ.

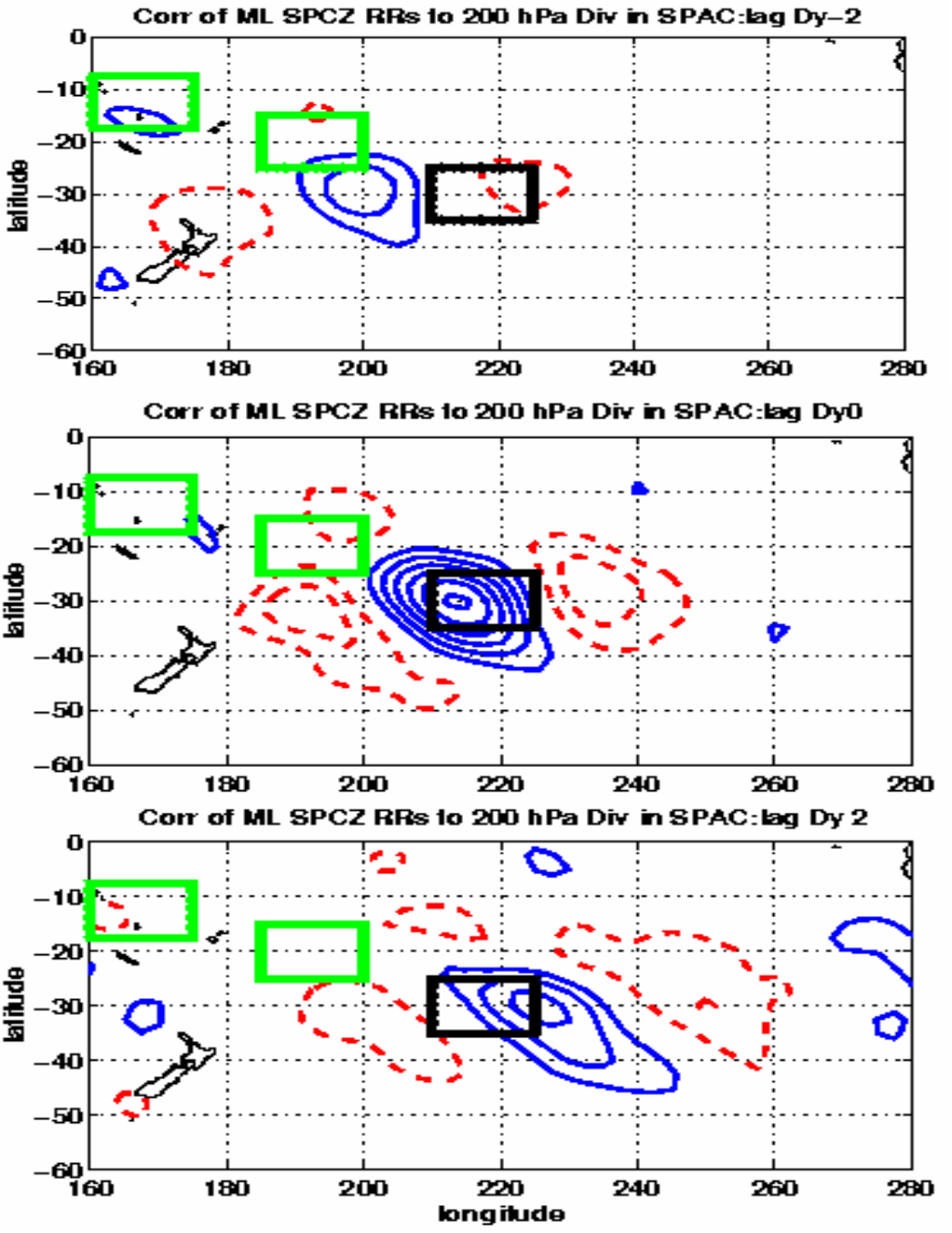

Figure 52: Same as figure 50 except for the ML SPCZ.

negative correlation minima are weaker in magnitude than the positive ones but they form a wave like pattern, suggesting that upper level divergence in the ML, and to a lesser extent in the ST SPCZ, is associated with mid-latitude waves. The location and the spatial scale of the

dominant correlation maxima are each similar to those found in the rain rate vs. rain rate correlation analysis. This is not surprising, as regions of upper level divergence (convergence) anomalies should correspond to regions of positive (negative) rainfall anomalies. The average phase speed of the dominant correlation maximum during lag days -1 to +1 is in the in the 5.1 to 5.5 m/s range for the TR and ST SPCZ and 8.5 m/s in the ML; these values are also very similar so those found in the previous correlation analysis. The direction of propagation is east-southeastward at distances of 550 km in the TR to 900 km in the ML SPCZ. As with the previous correlation analysis, the current results indicate a weak relationship between adjacent regions of the SPCZ, but near independence between the TR and ML SPCZ.

Lag Correlation Using Rain Rate and Height Anomalies

The rain rate vs. 200 hPa divergence correlation pattern suggests that wave like phenomenon may be important in the development of rainfall in the ST and ML SPCZ regions. The next question to answer is how important upper level troughs, in the present case negative height anomalies, are to the development of rainfall in these areas? To answer this, rain rate anomalies in the TR, ST and ML SPCZ were correlated against 200 and 500 hPa height anomalies in the South Pacific Ocean. The results indicated very similar correlation maxima and minima but the 500 hPa data exhibited slightly stronger correlation values; these are shown in figures 53 through 55. The magnitudes of the correlation coefficients are not as high as in the previous two analysis but they show distinct wave like patterns in the South Pacific when the ST and ML SPCZ test regions are used. The half wavelength of the dominant correlation maximum and minimum is ~ 2500 km in the ST and ~2300 km in the ML SPCZ at lag day 0. The dominant correlation minima, which I am interpreting as upper level troughs associated with positive rain rate anomalies, were located west-southwest of both the ST and ML SPCZ. This makes sense, as positive divergence and rain rate anomalies are more likely to occur east of a trough rather than

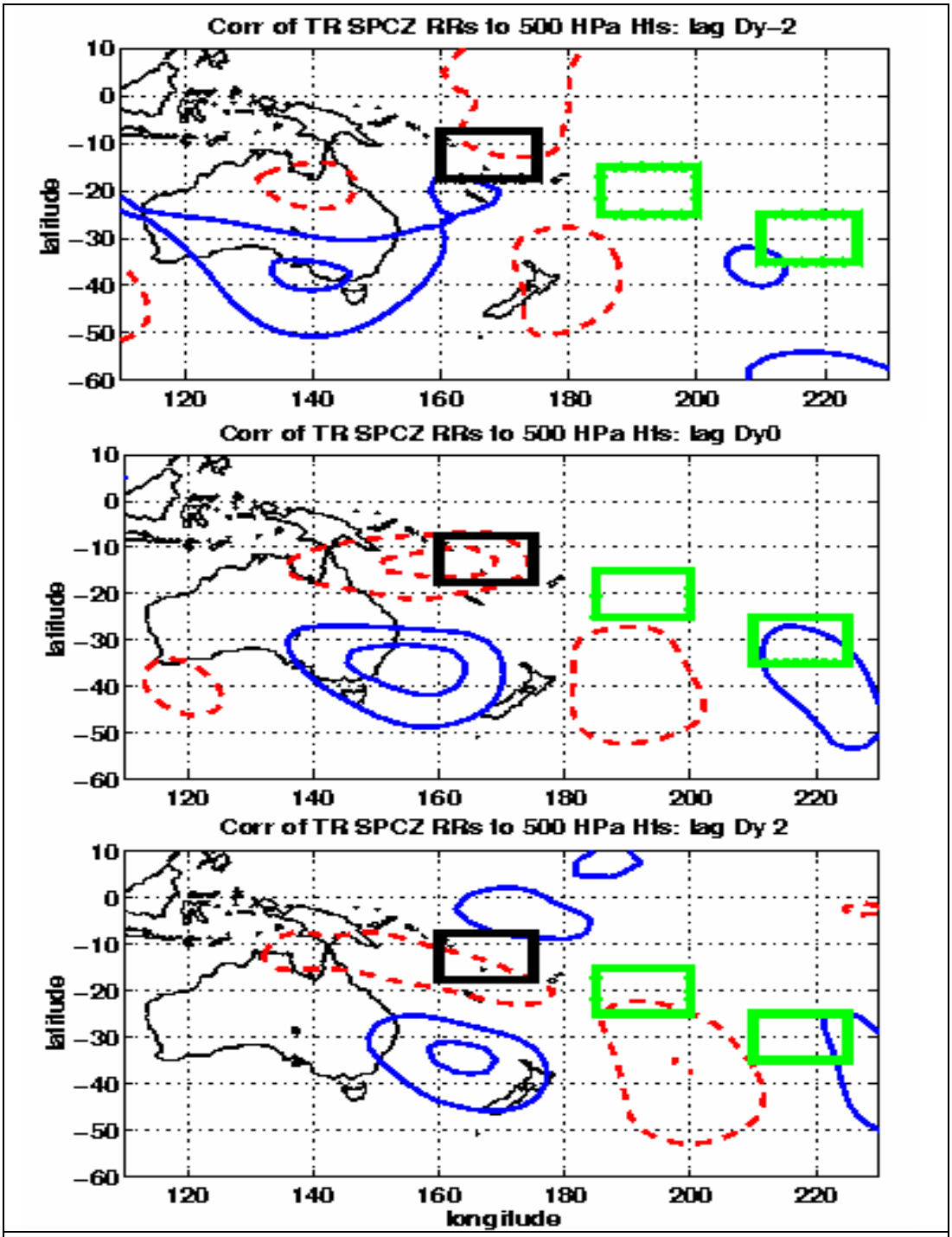

Figure 53: Backward and forward lag correlation results of rain rate anomalies within the TR SPCZ test region (black box) with 500 hPa height anomalies across the rest of the South Pacific. Each solid and dotted contour begins with the value 0.1 and is incremented by 0.1. The base region is denoted by the black rectangle and the zero contour has been omitted.

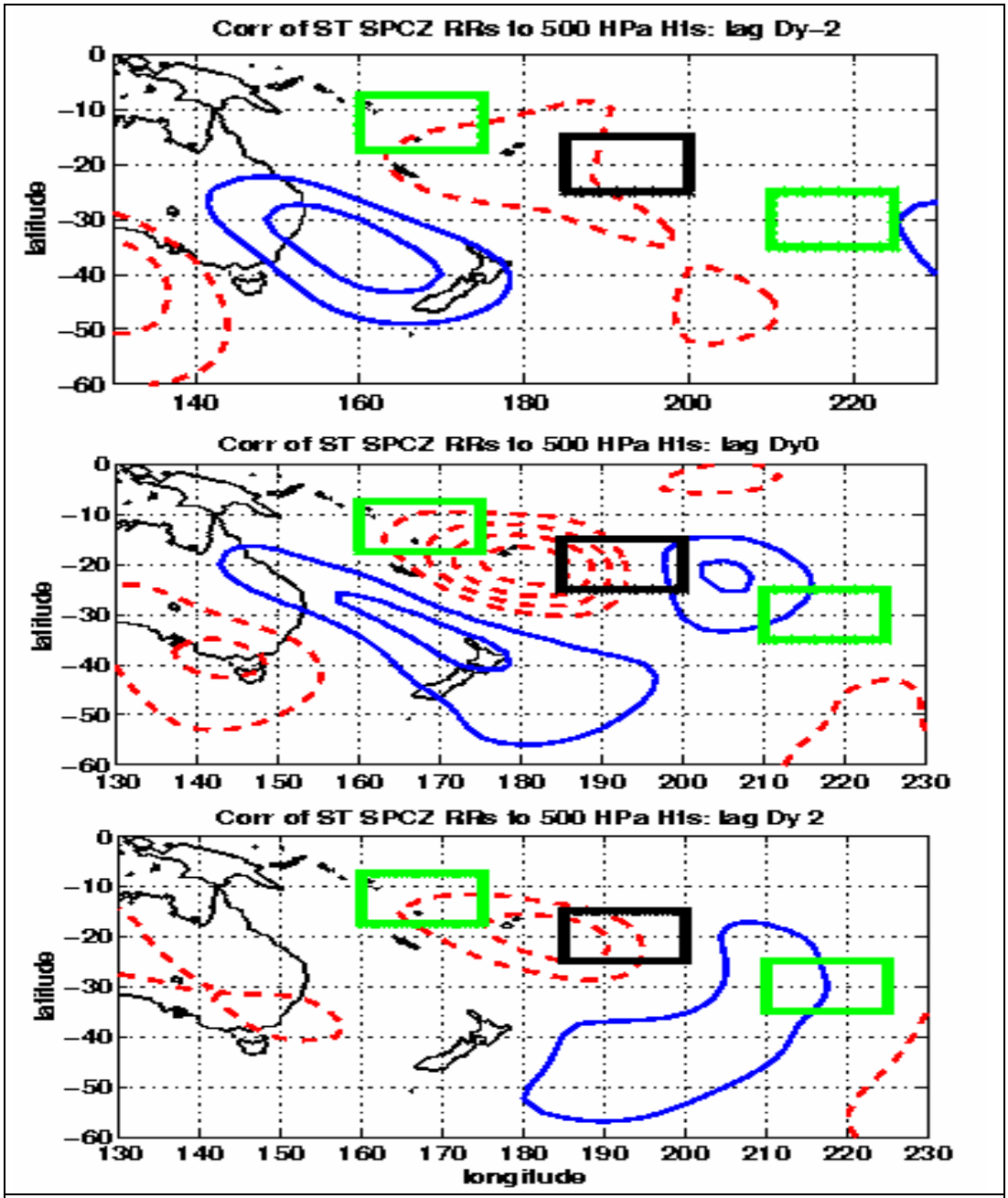

Figure 54: Same as figure 53 except for the ST SPCZ.

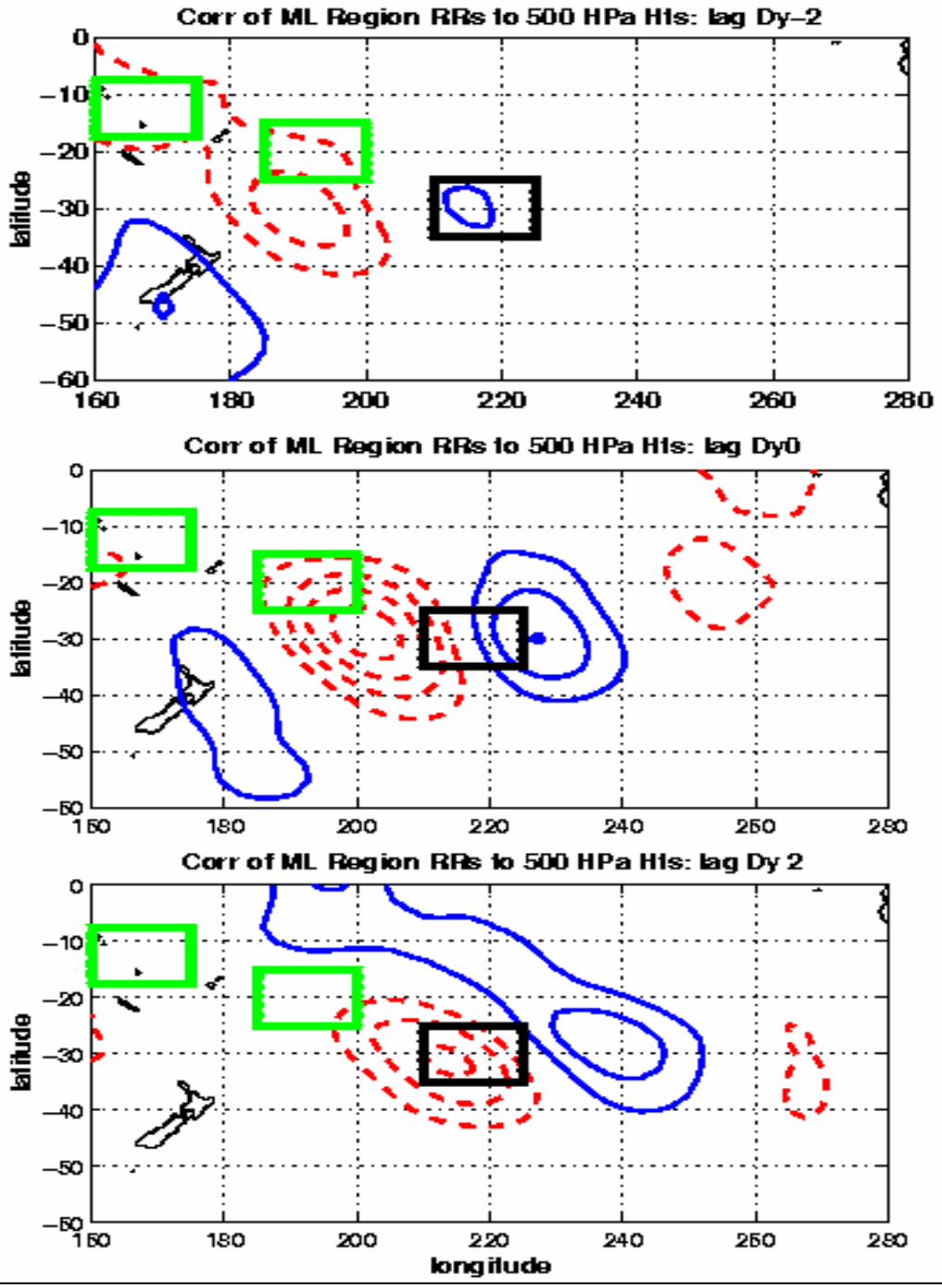

Figure 55: Same as figure 53 except for the ML SPCZ.

west of it outside of tropical regions. The phase speed of the dominant correlation minimum in the ML SPCZ is near 6 m/s, or about 3 m/s slower than that observed in the rain rate vs. divergence analysis. In the ST SPCZ, the phase speed of the dominant minimum is 3.9 m/s, about 1.6 m/s slower than that observed in the rain rate vs. divergence analysis. It is not fully understood why there is a speed discrepancy between the correlation minima associated with 200 hPa height data and those maxima associated with the 200 hPa divergence. In the TR SPCZ, the correlation pattern is extremely weak so no generalizations could be made about wave patterns and their affect on the region. However, at higher latitudes there is a dominant maximum and minimum which likely correspond to an upper level ridge and trough located southwest and southeast of the TR SPCZ respectively.

Summary

The data results suggest the entire SPCZ diagonal, about 10000 km in length as measured in the three year climatology, does not become convectively active at any one time. Rain rate vs. upper level divergence analysis revealed that a portion of the diagonal, on the order of 4500 km, becomes convectively active. Strong rain rate and divergence correlation maxima did not propagate large distances from one region of the SPCZ to another; instead they tended to propagate east-southeastward for about 500 to 1000 km. The results do suggest a weak relationship between adjacent regions of the SPCZ, but very little relationship between the TR and ML SPCZ at least in the long term statistical sense. Although correlation minima are present in the rain rate vs. 200 hPa divergence analysis, they tended to have much lower magnitudes than maxima. Nevertheless, the wave like patterns formed by correlation maxima and minima suggest strongly that upper level divergence and rainfall are associated with upper level troughs in the ST and ML SPCZ. Maxima and minima near the SPCZ test regions moved east-southeastward at speeds of 5.1 to 8.5 m/s, the higher speeds occurring in the ML SPCZ.

Lag correlation analysis of rain rates in the ST and ML SPCZ vs. upper level height anomalies revealed more distinct wave like patterns in the South Pacific. The half wavelength of the wave patterns ranged from 2300 to 2500 km and this is comparable with the half wavelength values observed by Kalnay et al (1986) in the meridional wind. The phase speeds of maxima and minima near the SPCZ test regions ranged from 3.9 to 5.3 m/s, a slower speed than in the previous two correlation analysis. The orientation of the wave patterns from higher to lower latitudes suggest mid-latitude cyclones may be dynamically important in the development of rain at sub-tropical and mid-latitude portions of the SPCZ. The magnitude of the highest correlation values were in the 0.2 to 0.5 range for most of the results implying a weak to moderate relationship at best. However, correlation analysis uses the entire data record which includes heavy, moderate and light rain events. A clearer signal may be present if heavy rain events alone are considered. The next chapter will focus on compositing only the heavy rain events within different regions of the SPCZ and will examine their spatial and vertical structure.

CHAPTER VI

COMPOSITES OF HIGH AND LOW RAIN RATE EVENTS

Lag correlation analysis using rain rates in a given test region correlated to 200 hPa divergence and height anomalies showed evidence of wave trains directed toward the ST and ML SPCZ regions. As peak magnitudes of the correlation coefficients ranged from 0.3 to 0.55, the signal was, at most, weak to moderate. This may be the result of using the entire data record for the analysis which includes light, moderate and heavy rain fall events. I now examine composites of high and low rain rate events to see if they reveal stronger wave signals in the height anomaly patterns.

Compositing Methodology

To create composites of high and low rain events I calculated rain rate time series for each SPCZ test region, the same as those defined in chapter II. Once a time series was created, high and low rain rate days were defined as a date where the average rain rate over a test region was greater than one standard deviation above or less than 0.75 standard deviations below the mean respectively. The reason for the unusual criteria for low rain rate days is due to the skewed distribution of the rain rates previously discussed in chapter II. If a single standard deviation was used to delineate low rain rate days there would be none in the TR and very few in the ST and ML SPCZ.

Once high and low rain rate days are determined for each test region, oscillations with periods greater than 32 days were removed from the height anomaly data via the Fourier analysis method discussed in Chapter V. I did not filter the rain rate data as the goal was to look at what the anomaly and raw values were so as to get an idea of how the rain rate pattern appears during low or high rainfall events. An effort to determine the statistical significance of the height anomaly patterns soon revealed some complex problems related to the temporal independence of

observations within a dataset. For instance, a set of observations at a given gridpoint in space may be temporally related to one another. From chapter V, autocorrelation patterns within the SPCZ regions indicate a time scale for height anomalies of approximately five days. In other words, an independent observation occurs every five days. To test for statistical significance, I consider the null case where the population mean is considered to be zero. I will reject the null hypothesis as long as the test statistic falls outside of the 95 percent confidence level. Rejecting the null hypothesis means the height anomaly sample mean is something other than zero, and hence the mean has some significance. The test statistic used is given by:

$$Z = (X-\mu_o)N^{0.5}/S \qquad (12)$$

where 'X' is the sample mean, 'μ' the population mean which is assumed to be zero in our case, 'N' the total number of independent samples within the composite and 'S' the sample variance. It may be argued that the variance of the 200 hPa height anomalies is unknown as well as the true data distribution, therefore a 'Z' distribution should not be used to determine significance. However, in cases where the sample size is somewhat large, that is $N \geq 30$, the Central Limit Theory allows the use of equation 12 with $S/N^{0.5}$ an appropriate estimate for the population variance (Montgomery and Runger, 1999). In our present case, the number of independent observations for each composite is at least ≥ 58, so I can apply with some confidence the Central Limit Theorem.

Seasonal Trends for High and Low Rain Rate Days

Once High Rain Rate Days (HRRDs) and Low Rain Rate Days (LRRDs) are defined for each test region it is important to know how relevant these classifications are. One way to do this is to see how much rainfall each classification contributes to the total rainfall. To determine this, the

Table 2: The percentage of HRRD, VHRRD and LRRD days comprising the dataset and the percentage of rain contributed to the total rainfall for each SPCZ test region.

Test Region	**Percent Days Comprising Data-set**	**Percent Rainfall Contribution to The Total**
TR SPCZ		
HRRD	**13.0%**	**37.4%**
LRRD	**23.0%**	**3.9%**
ST SPCZ		
HRRD	**13.6%**	**45.2%**
LRRD	**22.6%**	**1.3%**
ML SPCZ		
HRRD	**14.3%**	**46.6%**
LRRD	**27.0%**	**1.6%**

rain rates were summed for each SPCZ region and divided by the total amount of rain for the same location during the three year data period. The results are shown in Table 2. For each SPCZ test region, HRRDs make up approximately 14% of the dataset; yet, the contribution to the total rainfall ranges from 37 to 47%, a factor of three to four higher depending on the test region. Clearly, HRRDs are relatively rare in the dataset but contribute disproportionately to the total rainfall in each SPCZ test region. The reverse is true for the LRRDs; they make up a larger percentage of the dataset, yet the total contribution to the rainfall is very small. These results confirm the utility of making composites based on the HRRD and LRRD classification scheme.

Using these classifications, a histogram analysis is used to determine if seasonal differences between the TR, ST and ML SPCZ composites exist. Histograms, shown in figures 56 and 57, were created by binning HRRDs and LRRDs into the months of the year. The results over the TR and ST SPCZ indicate a broad maximum in HRRDs throughout the summer and fall and a distinct minimum during winter. The broad maximum from late spring to late fall corresponds to a period where, climatologically speaking, warm SSTs, low surface pressures and moist east-

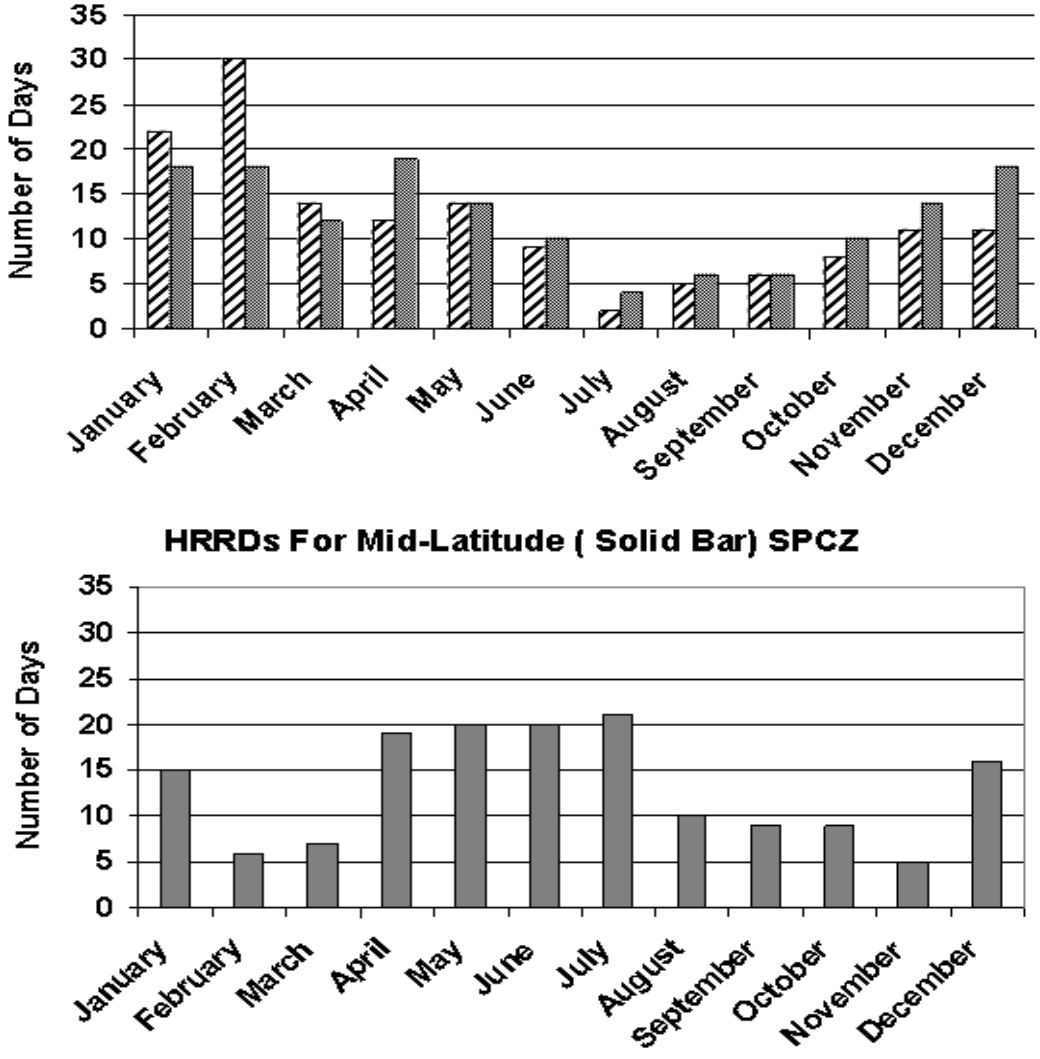

Figure 56: Histograms of High Rain Rate Days (HRRDs) by month for the TR, ST (top) and ML SPCZ (bottom).

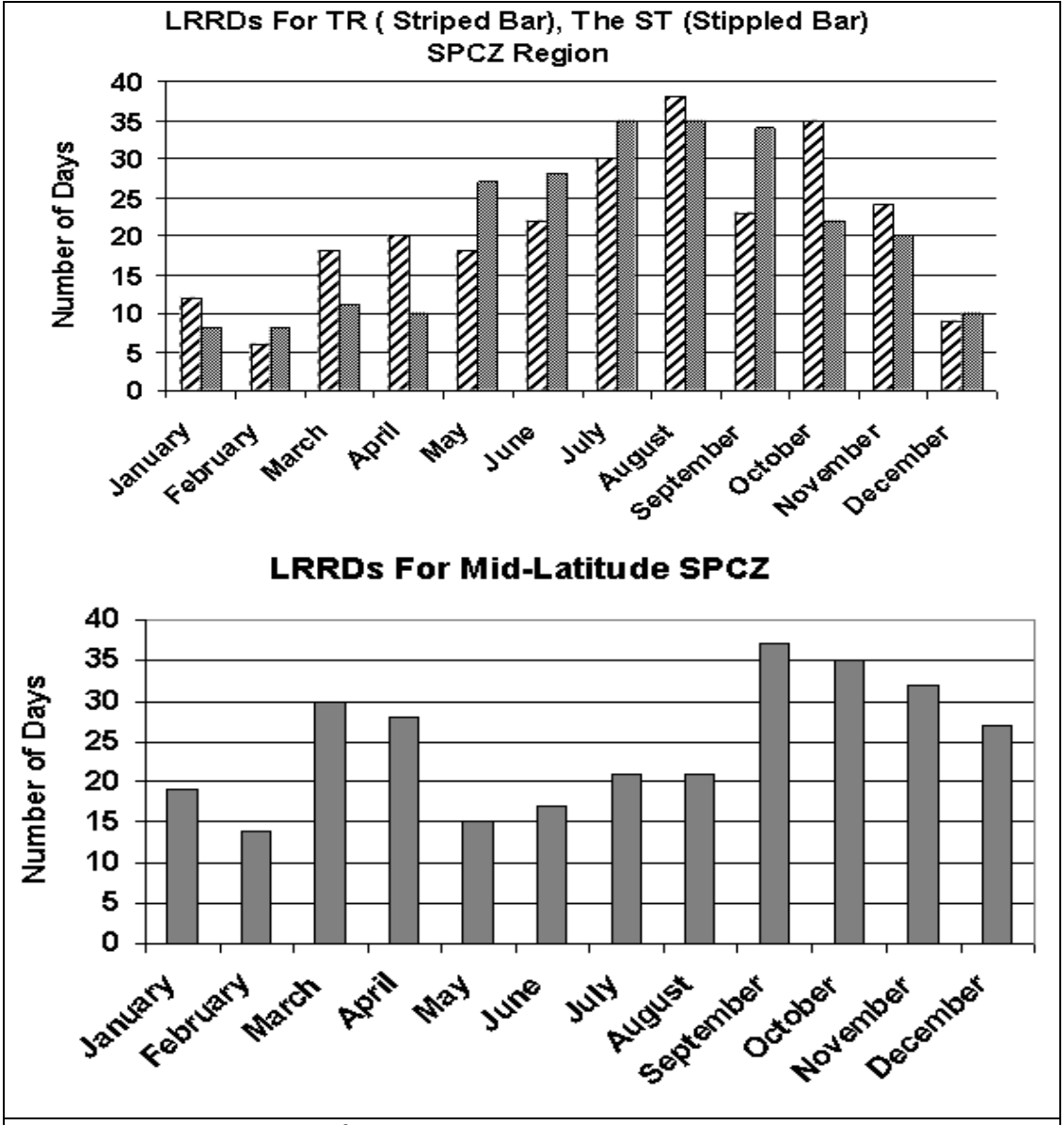

Figure 57: Same as 56 except for Low Rain Rate Days (LRRDs).

northeasterly tradewind flow is present. The minimum is likely due to the presence of strong east-southeasterly tradewind flow as the surface based sub-tropical high strengthens during late winter and spring. This type of surface wind flow is very dry with little moisture convergence, hence the minimum in HRRDS and the maximum in LRRDs.

The histogram for the ML SPCZ is different in that there are two distinct maxima and minima in the ML SPCZ. In the ML SPCZ, HRRD maxima are present during the months of fall/early winter and early summer. The fall/early winter maximum is likely due to strengthening of the polar jet along with increased large scale lift from passing mid-latitude cyclones. HRRD minima are present during late summer/early fall and during the late winter/spring. The minimum during late winter/spring is likely due to the strengthening of the sub-tropical high and the poleward migration of the polar jet. It is not understood what causes the early summer maximum and the late summer/early fall minimum but the sample size is rather small meaning these features may not be significant in a much larger dataset. Overall, the HRRD and LRRD histograms indicate distinct differences between the TR/ST and the ML SPCZ corroborating the results found in the seasonal distributions and lag correlation analysis. However, this does not mean these regions are completely independent of each other as the ML SPCZ maxima do overlap with portions of the broad TR/ST SPCZ maxima.

HRRD Composites of the SPCZ Test Regions

Using the techniques outlined earlier, HRRD composites were created for the SPCZ test regions using the 200 hPa height anomaly and the raw rain rate fields. The analysis revealed that each test region exhibited a series of maxima and minima in the height anomaly data with the resulting pattern, from this point on, referred to as a wave train. Spacing of maxima and minima, orientation of the wave train patterns and zonal phase speeds are discussed below.

Tropical SPCZ Region

Figure 58 shows the high rain rate composites for the TR SPCZ region. In comparison to the other HRRD composites, the height anomaly patterns are weak with only a small portion of it considered statistically significant. At composite Day -2, a slightly undulating wave train pattern is present poleward of 30°S and is oriented in a west-to-east direction with a half wavelength distance of approximately 2400 km, a value that corresponds to wave number 8. This distance

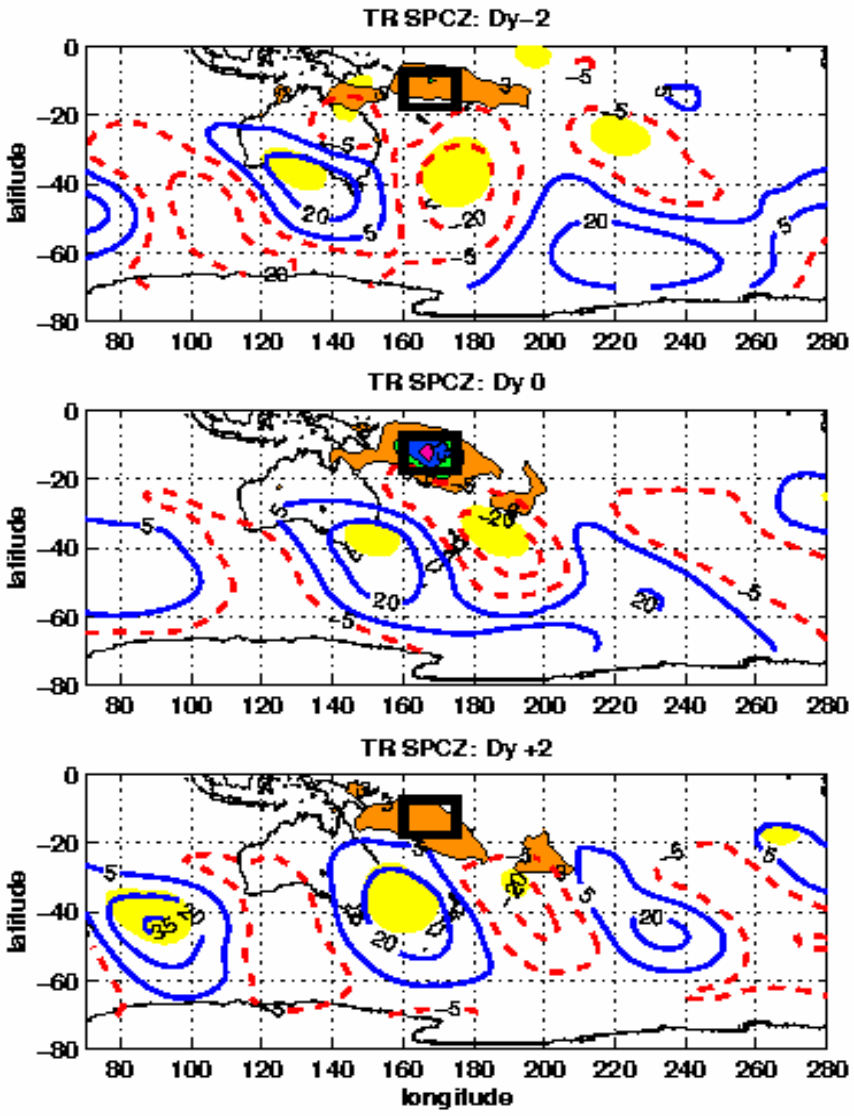

Figure 58: Composite of HRRDs over the TR region. Rain rate anomalies are shaded every 5 mm/dy with the first shade 3mm/dy; 200 hPa height anomalies are solid (positive) and dashed (negative) lines. Height anomalies begin at ± 5 meter contour and incremented every 15 meters. Height anomalies that are significant to the 95 percent confidence level are shaded gray.

does not change appreciably through the compositing time period. Directly south of the test region in the middle latitudes is a trough; in the tropics over Northern Australia, there is a very weak negative height anomaly which is located southwest of the test region. Rain rate anomalies

≥ 3 mm/dy are confined to tropical latitudes and stretch approximately 5500 km in a west-to-east direction.

At Day 0, the weak west-to-east oriented wave train remains although it has shifted eastward. The negative height anomaly at mid-latitudes, previously located south of the TR SPCZ, is now linked to the weaker anomaly over Northern Australia. The result is a single, northwest-to-southeast oriented negative height anomaly that lies nearly adjacent to the southern boundary of the rain rate anomaly pattern. The dominant maximum and minimum, in the center of the figure, are moving predominantly eastward at approximately 7.5 m/s. The rain rate anomaly pattern has taken on a more northwest-to-southeast direction with a length scale of approximately 4000 km and now has much higher values.

At Day +2, the tropical portions of the northwest-to-southeast oriented negative height anomaly has dissipated; a positive height anomaly is now just southwest of the TR SPCZ. The mid-latitude positive and negative height anomalies have continued to propagate eastward at speeds of around 5 m/s. Rain rates are much weaker with the pattern continuing in a northwest-to-southeast orientation and extending approximately 6000 km in a discontinuous fashion. Despite the weak signal, the composite height anomaly pattern and its subsequent time evolution is strongly similar to that observed in the correlation maxima and minima of the rain rate vs. 500 hPa height anomaly lag correlation analysis.

Sub-Tropical SPCZ

Figure 59 shows the high rain rate composites for the ST SPCZ. In contrast to the TR SPCZ, much of the height anomaly patterns in this set of composites are considered statistically significant. At Day -2, a well defined wave train pattern is present and extends west-southwest-to-east-northeast from the Eastern Indian Ocean into the Southwest Pacific. The half wavelength of this pattern is approximately 2500 km corresponding to a wave number 8. A northwest-to-

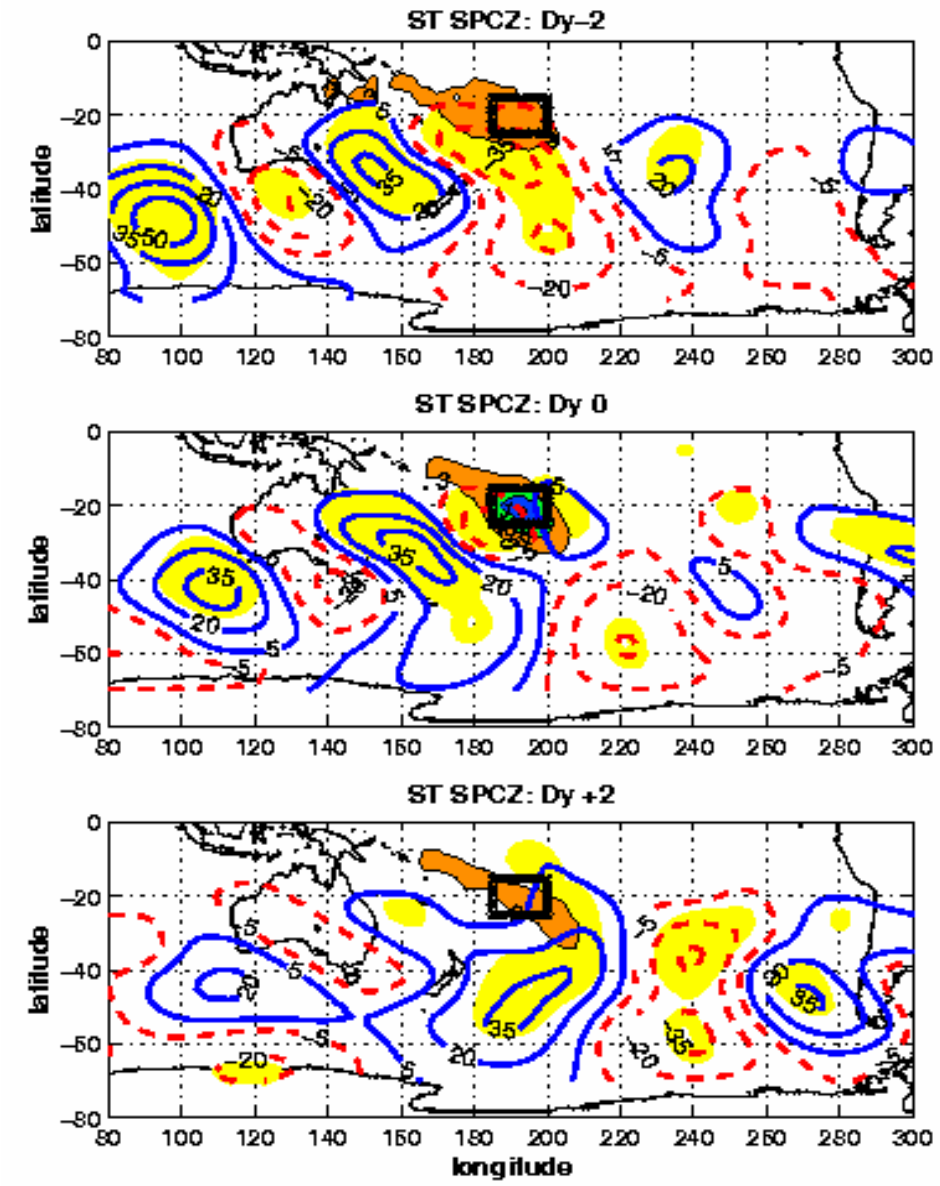

Figure 59: Same as figure 58 except for the ST SPCZ.

southeast oriented pair of negative height anomalies, one at 34°S 168°W and another 52°S 158°W, extends from mid-latitudes towards the southwestern portion of the ST SPCZ region. Rain rate anomlies ≥ 3 mm/dy extend from New Guinea about 4300 km southeastward into the test region.

At Day 0, the entire western section of the wave train has shifted equatorward with a slightly smaller half wavelength value of approximately 2400 km. The pair of negative height anomalies has split with one anomaly shifting equatorward and slightly eastward into a position that lies directly over the southwestern portion of the test region. The behavior noted here is reminiscent of the development of a 'cut-off' low, or a cyclone that has become isolated from the mid-latitude westerly flow. The higher latitude negative height anomaly continues to track eastward and slightly poleward at a speed near 10 m/s. Height anomalies west of 160°E are moving eastward at an average speed of approximately 6 m/s. At this time, a negative and positive height anomaly couplet has developed across the test region. The negative height anomaly over the southwestern portion of the test region is weaker than it was at Day -2 while the positive anomaly to the east has only just developed. The development of this couplet along with the orientation of the overall wave train pattern gives the suggestion that energy is propagating into the ST SPCZ then east-southeastward out of it. During this time, rain rate anomalies ≥ 3 mm/dy continue to extend approximately 4300 km in a southeasterly direction.

On composite Day +2, the wave train west of the ST SPCZ has weakened considerably. South and east of the test region, a high latitude wave train has developed with anomalies traveling eastward at approximately 7 m/s. The negative height anomaly immediately adjacent to the test region on Day 0 has given way to positive anomalies to the south and east of it on Day +2. Rain rate anomalies ≥ 3 mm/dy make up a relatively narrow, northwest-to-southeast oriented band that stretches for approximately 4600 km.

Mid-Latitude SPCZ

Figure 60 shows the high rain rate composites for the ML SPCZ. The wave train pattern present in this set of composites is more regional in scale than the ST SPCZ. At Day -2, a southwest-to-northeast oriented couplet of positive and negative height anomalies is located west-to-southwest of the test region. The half wavelength distance is approximately 2900 km

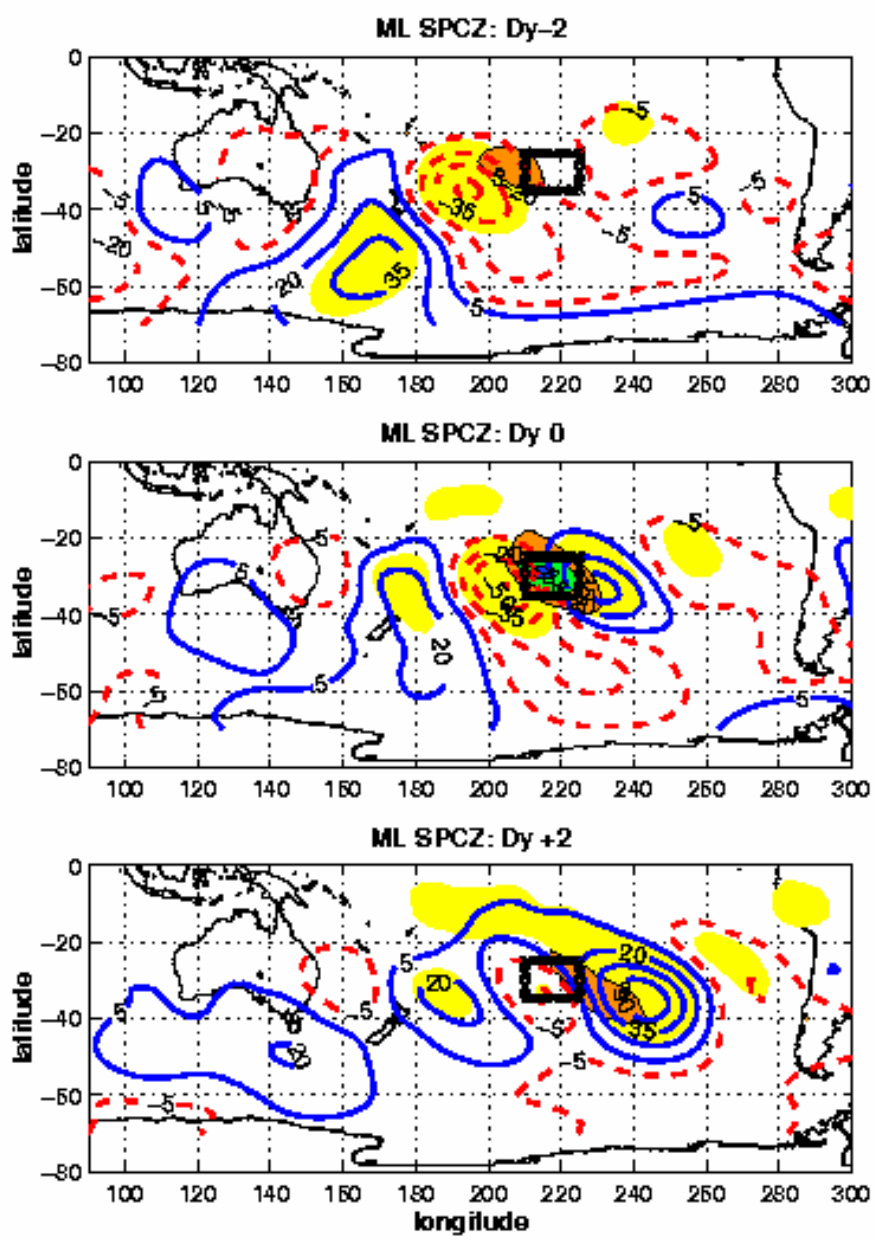

Figure 60: Same as figure 58 except for the ML SPCZ.

corresponding to a wavenumber 7. An area of rain rates ≥ 3 mm/dy is located west of the test region and stretches 1900 km southeastward. At Day 0, both the positive and negative height anomalies from Day -2 have shifted westward and equatorward to a position adjacent to the western boundary of the ML SPCZ while a new positive anomaly has developed east of the

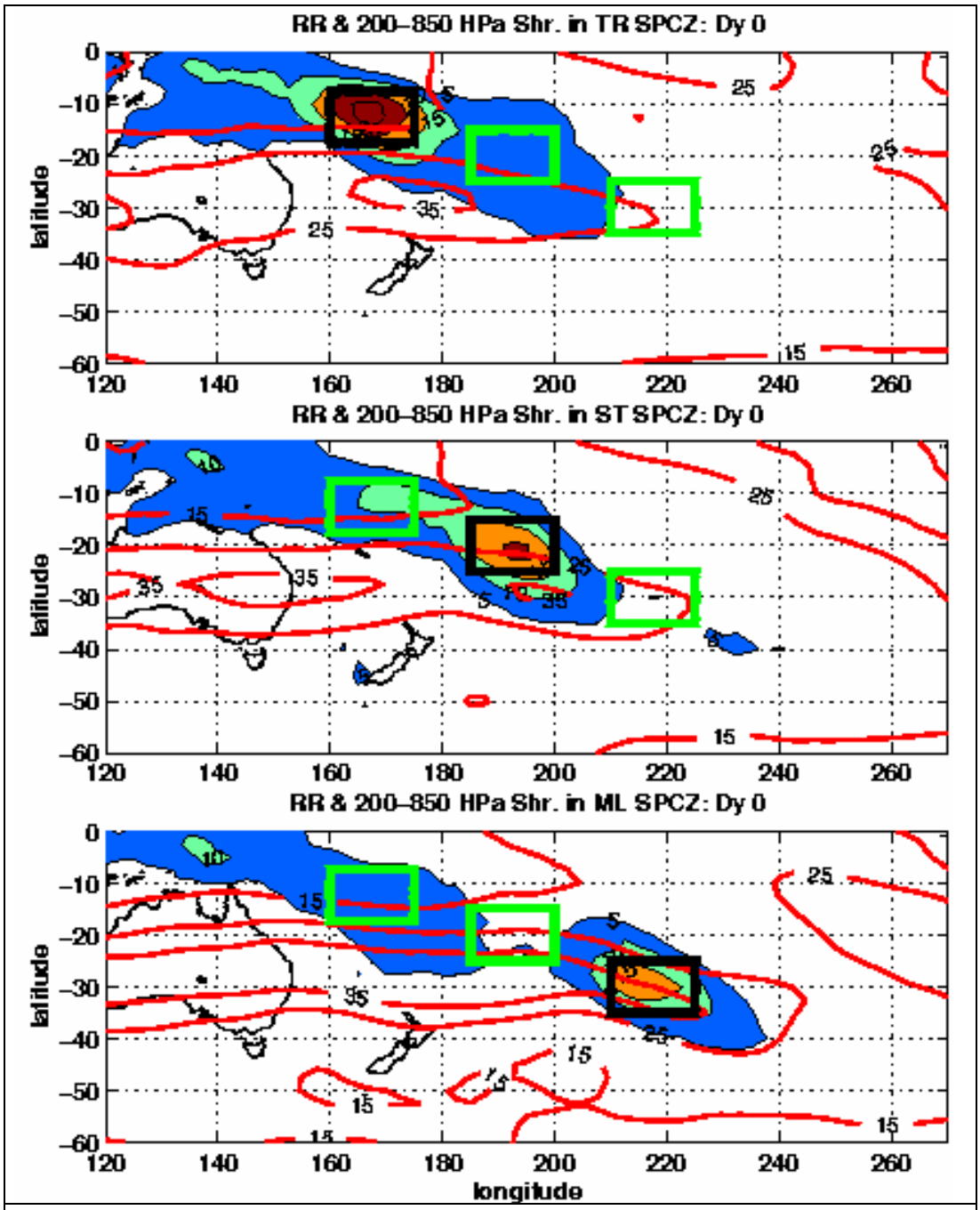

Figure 61: Raw rain rates (shaded) and 200-850 hPa shear for HRRD composite Day 0 for the various SPCZ test regions. Shear values begin at 5 m/s contour and are incremented every 10 m/s. Rain rates shown start at 5 mm/dy and are shaded every 5 mm/dy thereafter. The active composite region is outlined in black.

region. The resulting wave train pattern is west-to-east oriented with a half wavelength distance of approximately 2400 km, still corresponding to a wavenumber 8. Height anomalies progressed

eastward at phase speeds of approximately 6 m/s. The rain rate anomaly pattern is very well defined at this time and extends approximately 2600 km towards the southeast. At Day +2, the negative anomaly adjacent to the test region on Day 0 has weakened substantially while the downstream positive anomaly has strengthened. Rain rate anomalies ≥ 3 mm/dy are now in a relatively narrow band and extend approximately 2600 km southeastward. The progression observed for this set of composites is very reminiscent of that observed in the ST SPCZ composites; that is, energy appears to move from higher to lower latitudes into the test region then move eastward out of it.

In chapters III and IV, I examined the annual and seasonal distributions in vertical wind shear across the SPCZ and noted the higher magnitudes over the ST and ML regions. I now want to know if the vertical shear, and therefore baroclinicity, is present during HRRDs as well. Previously, I had used only rain rate anomalies in the composites but for this next figure I will use raw rain events to determine how much significant rainfall occurs along the SPCZ during HRRDs. Figure 61 shows the composite Day 0 200-850 hPa vertical wind shear and raw rain rate distribution for the TR, ST and ML SPCZ.

In each case a maximum in shear is present between the latitudes of 20° and 40°S; there is little difference in the magnitude in the various composites. As observed in chapter III and four, the shear is substantially lower in the tropics than at higher latitudes. For composite Day 0, shear values in the TR SPCZ range from 10 to 20 m/s range. Note that rain rates of 5 -9 mm/dy extend well into the ST SPCZ but never fully into the ML SPCZ. However, the very highest rain rates, values ≥ 10 mm/dy, extend from the New Guinea into the TR SPCZ test region and just northwest of the ST SPCZ region. The raw rain rate pattern for composite Day 2 (not shown) did not indicate high rain rates extending into the ST or ML SPCZ although significant rain rates of 5-9 mm/dy did extend all the way into the ML SPCZ.

In the ST SPCZ, shear values range from 20 to 30 m/s and rain rates ≥ 10 mm/dy extend from the TR SPCZ well into the base region itself. Lighter rain rates exhibit a pattern similar to that seen for composite Day 0 in the TR SPCZ. As in the TR SPCZ, rain rates ≥ 10 mm/dy in later composites never propagate into the ML SPCZ. However, the pattern made by lighter rain rates is very similar to the TR SPCZ results. In both regions, the raw rain rate pattern exhibited a pattern reminiscent to the climatological rain rate maximum observed in the SPCZ. In the ML SPCZ, vertical wind shear ranging from 25 to 35 m/s and rain rates ≥ 10 mm/dy were pretty much centered on the test region. Lighter rain rates form a discontinuous pattern with little rain occurring in the ST SPCZ region; the pattern is very reminiscent of the winter and spring SPCZ rain rate maxima.

In the ML SPCZ, significant amounts of baroclinicity, as indicated by the presence of vertical wind shear, are available for transient waves. This combined with the west-to-east height anomaly wave patterns suggest baroclinic dynamics are important during HRRDs in this region. In the TR SPCZ, the vertical shear and the very weak height anomaly patterns suggest that equivalent barotropic dynamics are more important in this region. For the time being, however, it is likely that rainfall in the TR SPCZ is governed by barotropic processes such as those described by Kodama (1999). That is, an off equatorial heat source, such as positive SST anomalies or heating induced by a land mass such as New Guinea, induces the development of boundary layer low pressure and moisture convergence, convection and rainfall with outflow aloft contributing to the development of a sub-tropical jet. For the ST SPCZ, significant amounts of vertical shear and height anomaly wave train patterns are oriented from higher to lower latitudes west of the base region suggesting the importance of mid-latitude dynamics. However, the presence of a nearly stationary negative height anomaly isolated from the mid-latitude westerly flow is something observed in the sub-tropical and tropical latitudes (for example, Sadler (1977), Schapiro (1986) as well as the personal forecasting experience of the

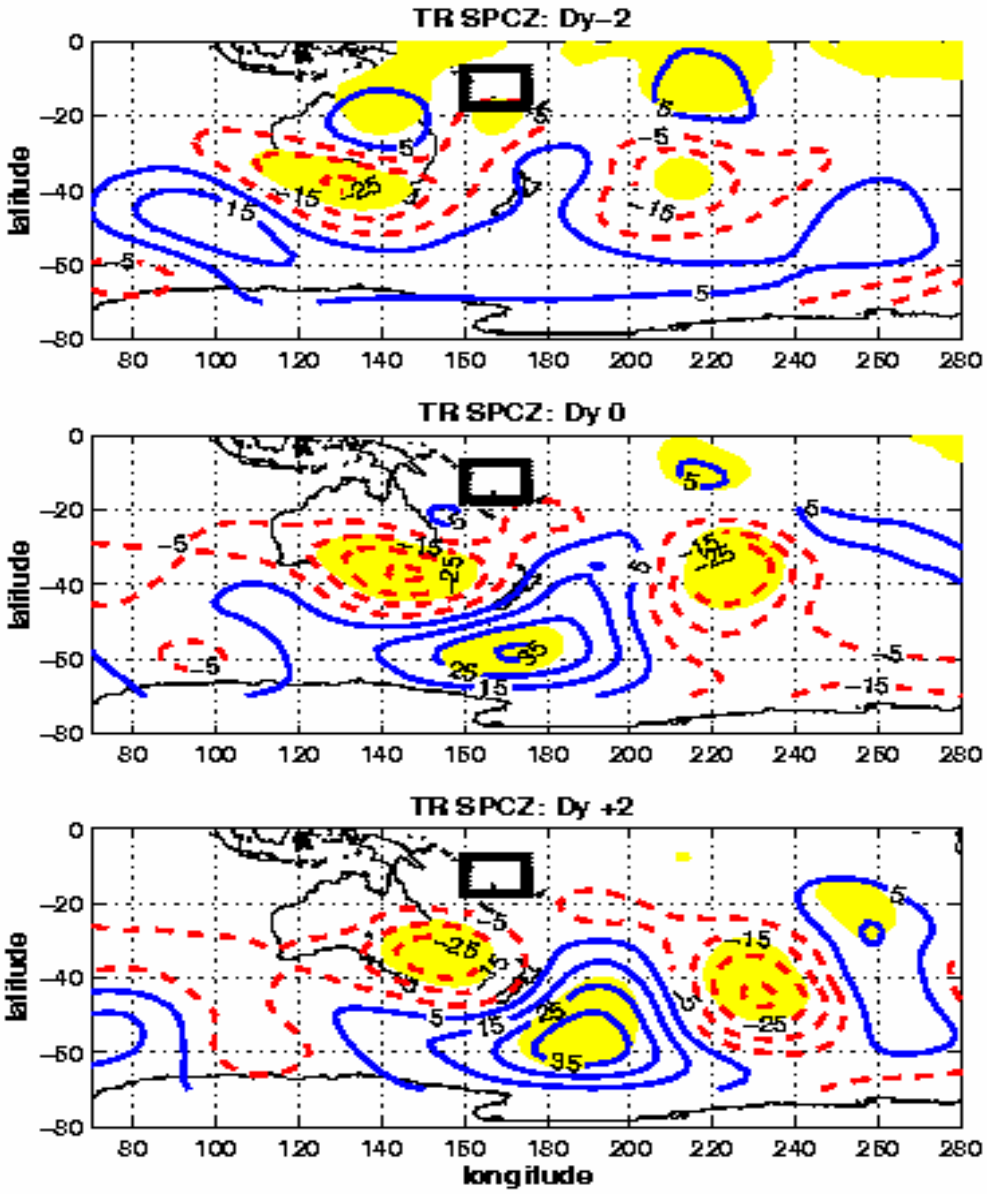

Figure 62: Composite of LRRDs over the TR region. Rain rate anomalies are shaded every 5 mm/dy with the first shade 3mm/dy; 200 hPa height anomalies are solid (positive) and dashed (negative) lines. Height anomalies begin at ± 5 meter contour and incremented every 15 meters. Height anomalies that are significant to the 95 percent confidence level are shaded gray.

author). Additionally, the composite Day 0 rain rate pattern was similar to that observed in the TR SPCZ and is suggestive of the poleward advection of moisture, again, associated with an off

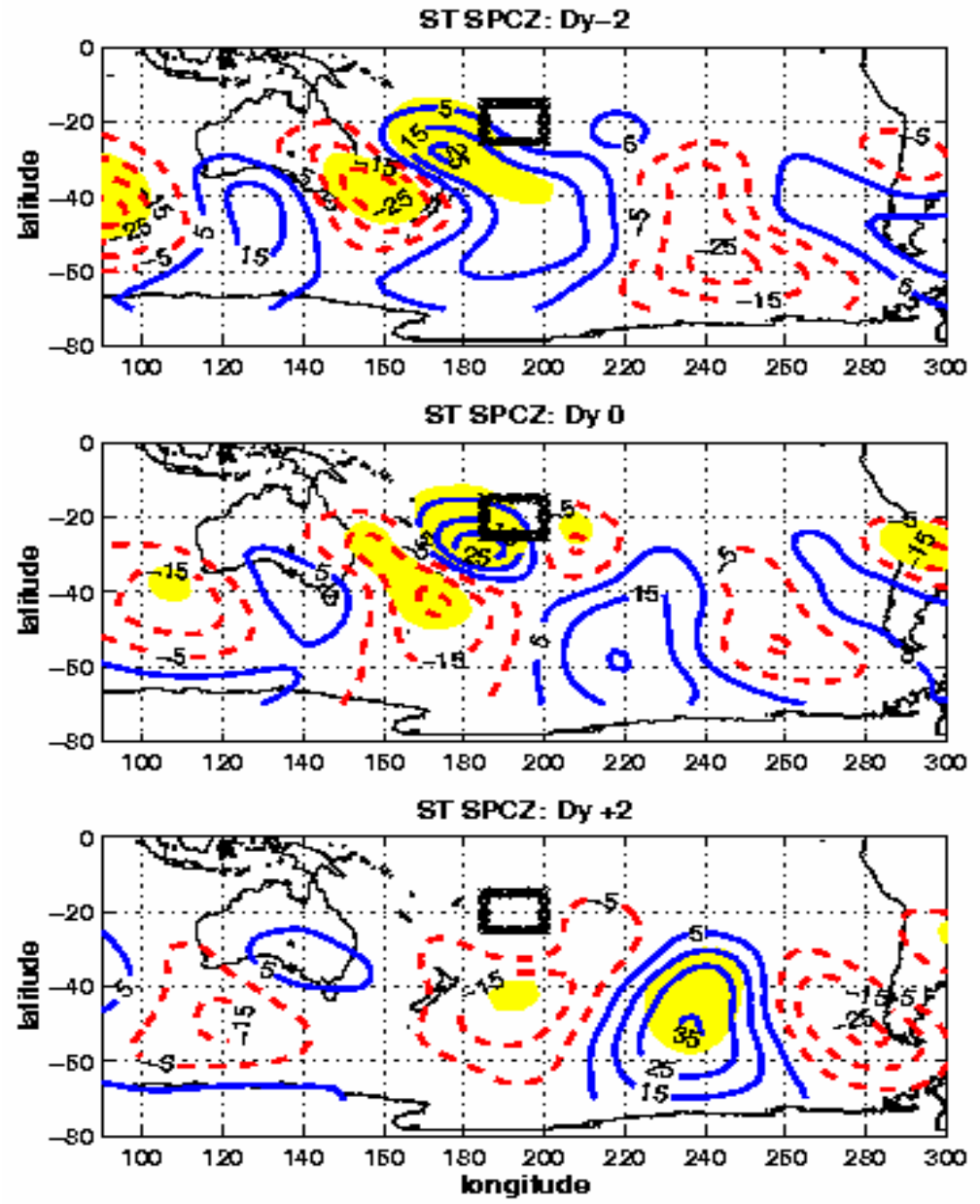

Figure 63: Same as 62 except for the ST SPCZ.

equatorial heat source (Kodama, 1999). This may suggest that both baroclinic and some implicit equivalent barotropic processes are important within this region.

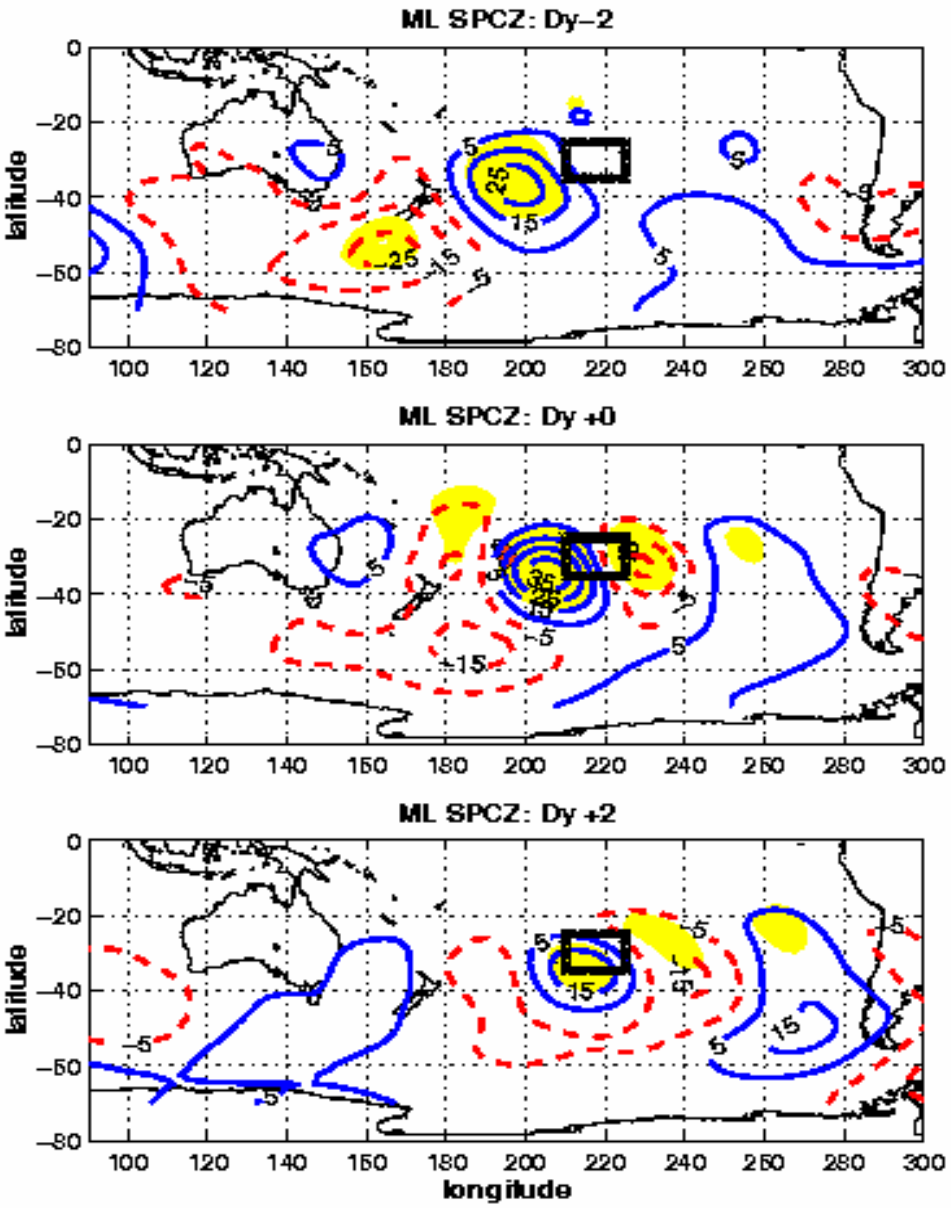

Figure 64: Same as figure 62 except for the ML SPCZ.

LRRD Composites of the SPCZ Test Regions

Using the techniques highlighted earlier in the chapter, composites of LRRDs were created and are shown in figures 62 through 64. In each SPCZ test region, the height anomaly patterns displayed are very similar to those seen in the HRRDs except *all of the wave trains are 180° out of phase*. For example, figure 63 shows the LRRD composites for the ST SPCZ. On Day 0,

note that instead of a negative height anomaly west of the test region, as seen in the HRRD composite, there is now a positive one; east of the test region, instead of a positive there is now a negative anomaly. It should not be construed that the out of phase nature is due to LRRDs occurring several days after the HRRDs; instead, they reflect seasonal differences between the two set of composites as was discussed earlier in the chapter. Figure 65 shows the 200-850 hPa vertical wind shear for LRRDs in the South Pacific. The shear magnitudes are higher in the TR and ST SPCZ as LRRDs are predominantly occurring during winter and spring. In the ML SPCZ, the values are lower as LRRDs in this region occur more in the spring and summer. Note that substantial values of shear are present in the SPCZ during LRRDs yet high rain rates are not present. Clearly baroclinicity is a necessary but not a sufficient condition for heavy rain in the ST and ML SPCZ. What is important, evident from the both the HRRD and LRRD composites, is the presence of a synoptic scale cyclone which provides the lift necessary to set the stage for heavy rainfall.

Vertical Structure of Height Anomalies for HRRD Composites

HRRD composite analysis indicated that mid-latitude dynamics may be important within the ST and ML SPCZ. I now use the 850, 500 and 200 hPa height anomaly composites to examine the vertical structure of low pressure with height within the SPCZ test regions. The goal is to determine whether the tilt with height of negative height anomalies is more reminiscent of a equivalent barotropic or baroclinic cyclone. Before I introduce the results, I briefly describe the vertical structure of low pressure with height in barotropic, equivalent barotropic and baroclinic atmospheres. A barotropic atmosphere is one characterized by the absence of horizontal temperature gradients such that density is a function of pressure only. This means the speed and direction of the geostrophic wind is independent with height (Wallace and Hobbs, 1977). In such an atmosphere, pressure features, such as ridges and troughs, have little or no tilt

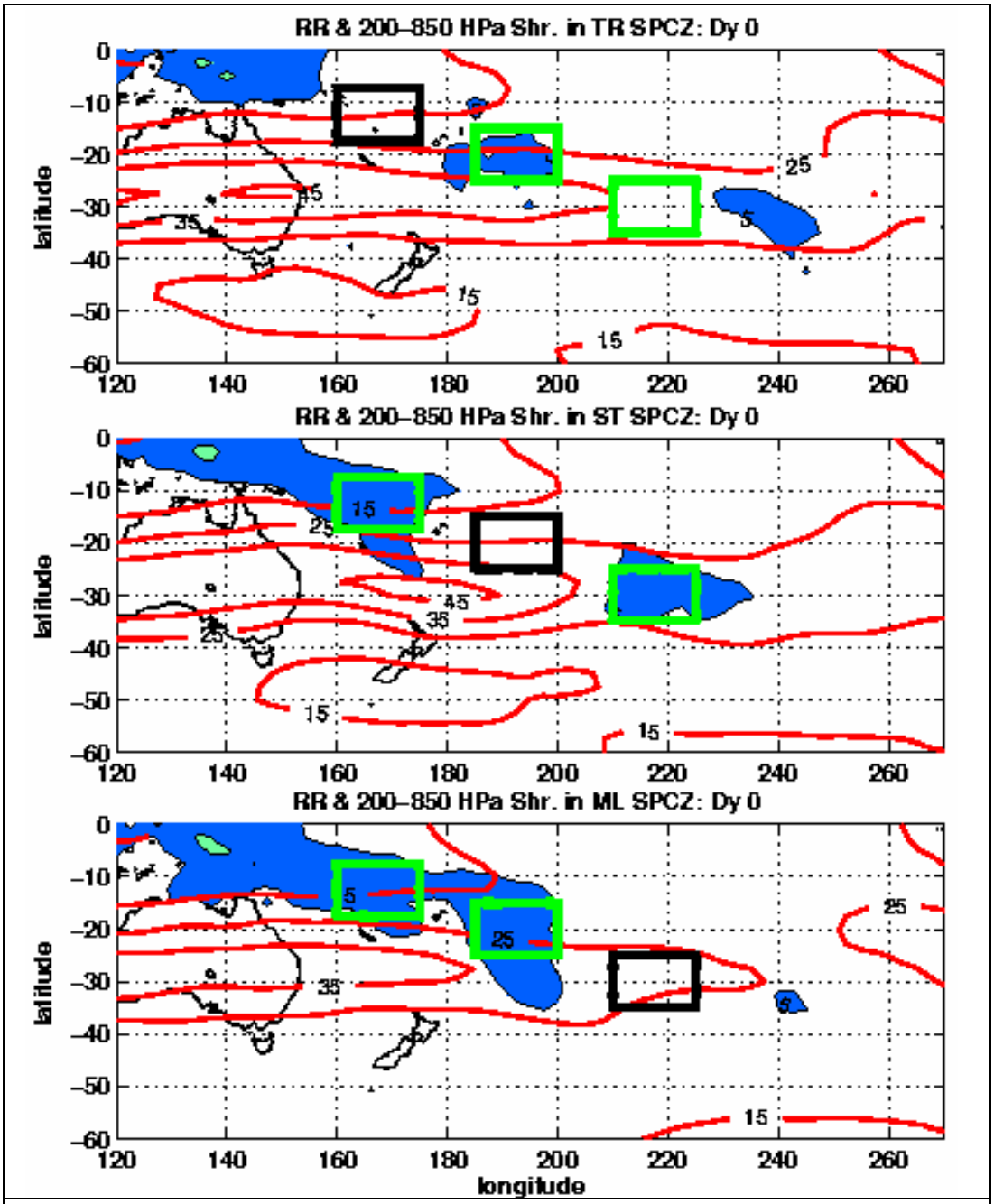

Figure 65: Raw rain rates (shaded) and 200-850 hPa shear for LRRD composite Day 0 for the various SPCZ test regions. Shear values begin at 5 m/s contour and are incremented every 10 m/s. Rain rates shown start at 5 mm/dy and shaded every 5 mm/dy thereafter. The active composite region is outlined in black.

with height and little or no geostrophic vertical wind shear. Large areas of the tropics are barotropic in nature due to the near absence of horizontal temperature gradients. An equivalent

barotropic atmosphere is one where a horizontal temperature gradient exists but isotherms remains parallel to height contours throughout the atmospheric column; this means temperature advection is not present. Once again, ridges and troughs exhibit little or no tilt with height in such an atmosphere. However, because a horizontal temperature gradient exists, the geostrophic wind direction, not the speed, does change with height (Wallace and Hobbs, 1977). In a baroclinic atmosphere, a horizontal temperature gradient is present and temperature advection is significant. The temperature gradient is important because it is the energy source for atmospheric jets via the thermal wind relation; strong thermal advection acts to tighten the temperature gradient and strengthen the jet. Because a horizontal temperature gradient is present, baroclinic systems are characterized by substantial geostrophic vertical wind shear. Baroclinic cyclones typically exhibit a westward tilt with height between the surface and upper level trough (Holton, 1992; Randel and Stanford, 1985). This westward tilt is necessary so that the developing disturbance can tap into the potential energy available within the mean flow.

Cyclones in the mid-latitudes go through a typical life cycle (Holton, 1992; Randel and Stanford, 1985). As they are developing, there may be a weak temperature gradient and the tilt with height between the surface and upper level trough may be small. As the cyclone intensifies temperature advection increases tightening the temperature gradient resulting in more available potential energy which in turn strengthens the wind flow. During intensification, the tilt between the surface and upper level trough may is the largest observed during the cyclones life cycle. As a cyclone matures, temperature advection decreases which eventually leads to a weaker temperature gradient. The weaker temperature gradient leads to a reduction in the conversion of potential to kinetic energy. Not surprisingly, the tilt between the surface and upper level troughs

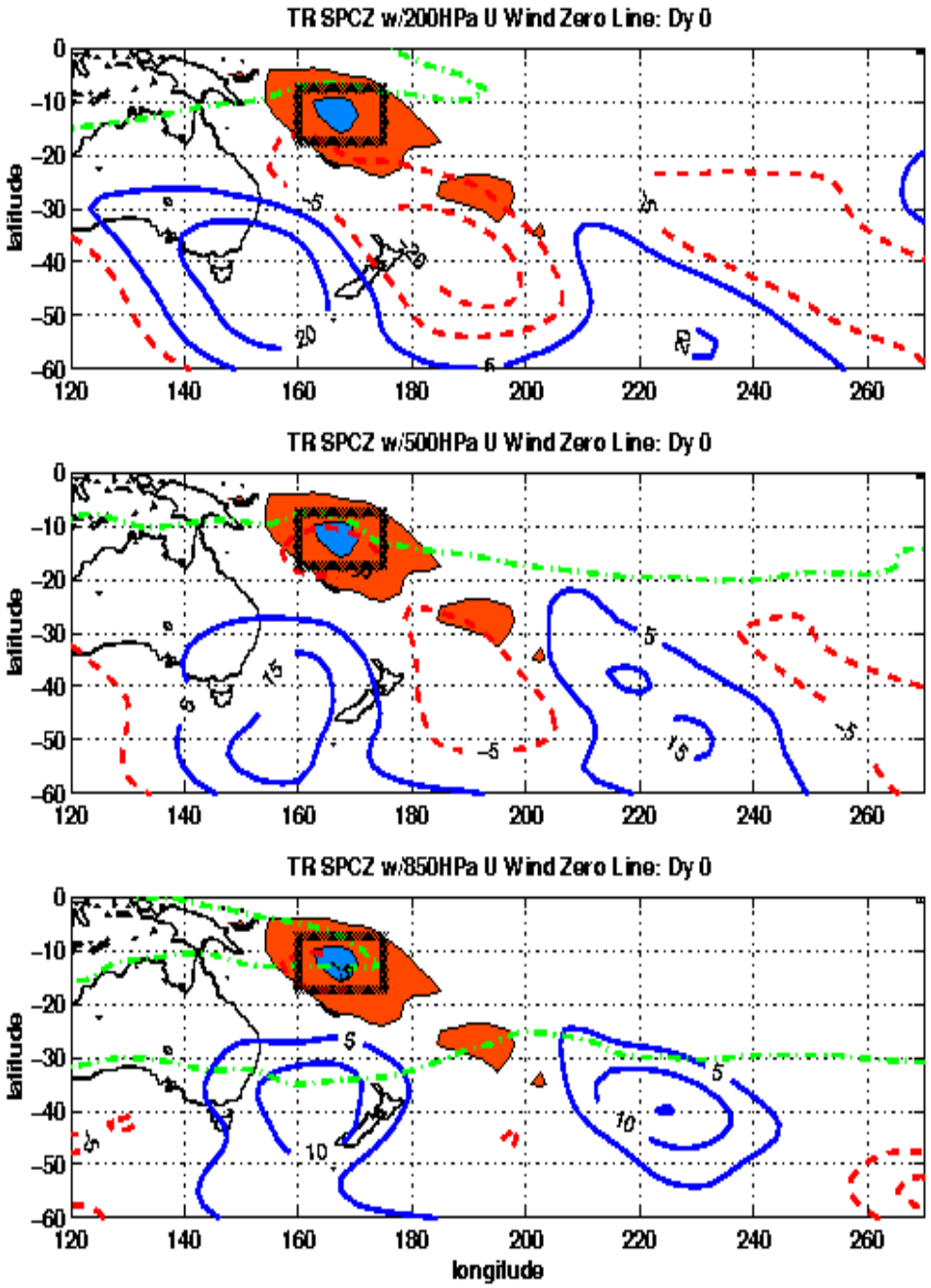

Figure 66: Day 0 composite with 200, 500 and 850 hPa height anomalies (solid/dashed lines), rain rates (shaded) and the zero contour of the mean zonal wind (dash-dot) for TR SPCZ. Height anomalies begin at ± 5 meter contour for each pressure level. However, the 200 hPa level is incremented every ± 15 meters, the 500 hPa level every 10 meters and the 850 hPa level every 5 meters.

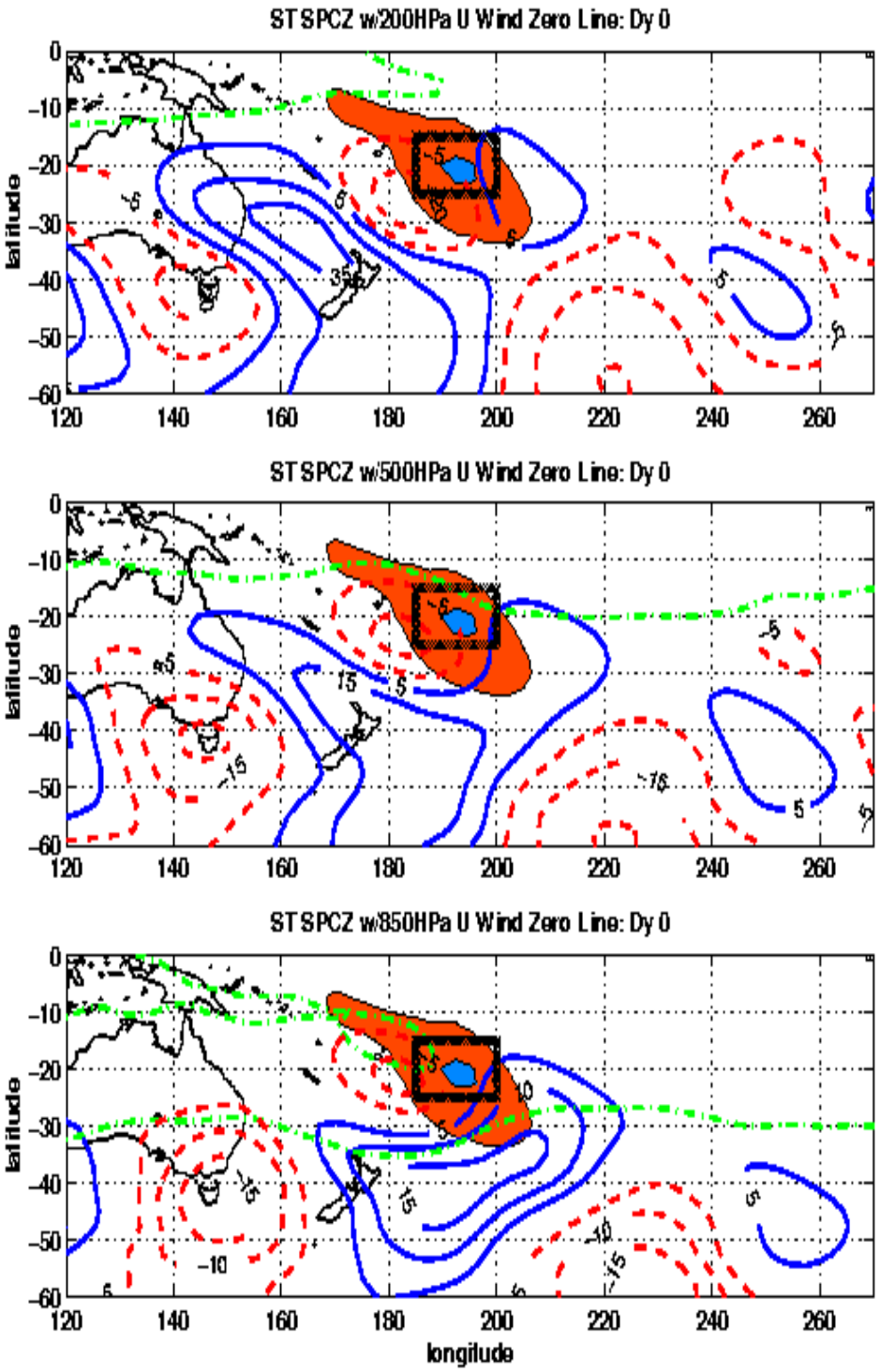

Figure 67: Same as figure 66 except for the ST SPCZ.

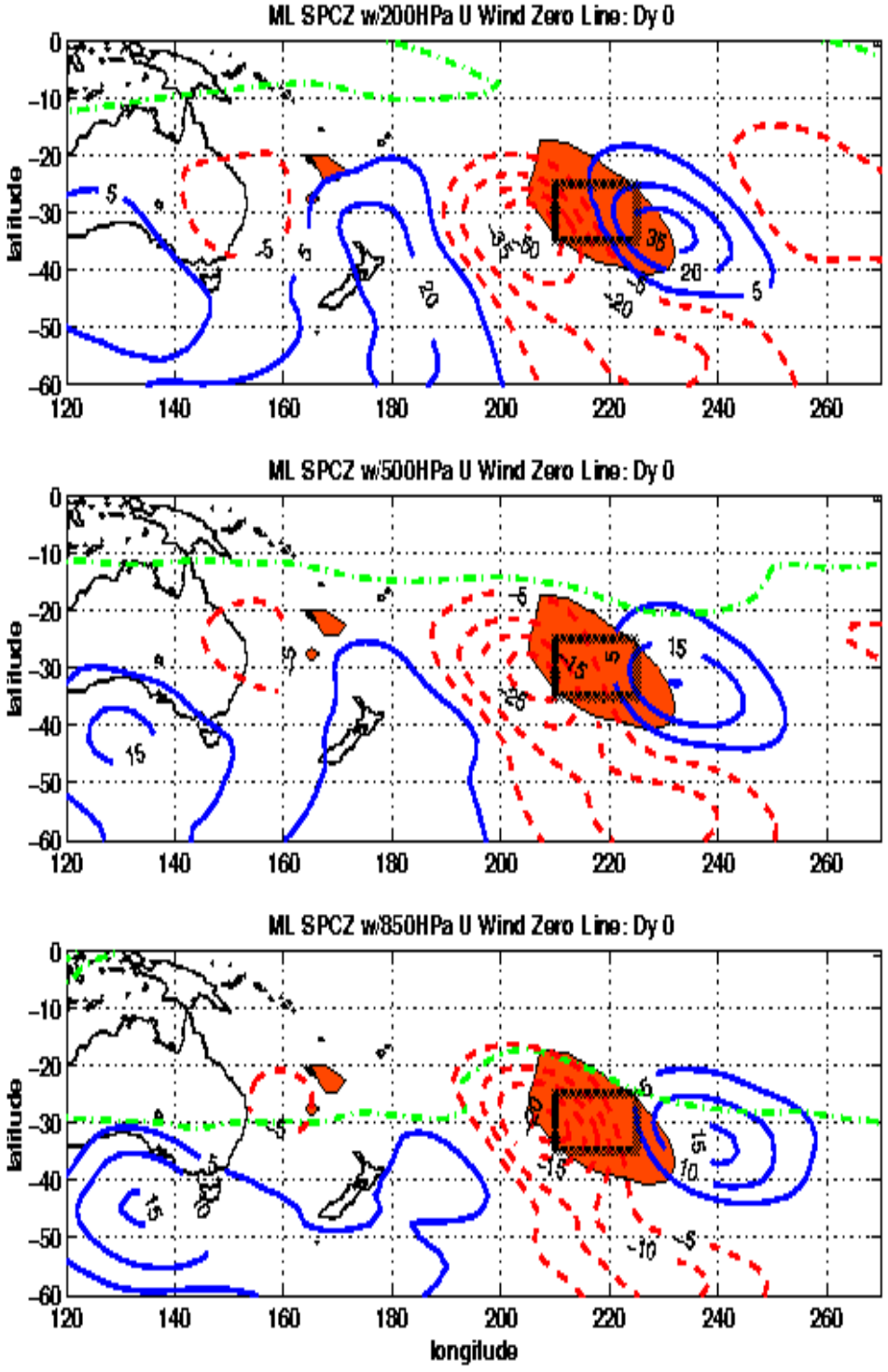

Figure 68: Same as figure 66 except for the ML SPCZ.

becomes less and exhibits a structure reminiscent of an equivalent barotropic cyclone. At this point, the cyclone may decay and dissipate altogether, or it may undergo additional cyclogenesis depending on the environmental conditions. Using this information, I can evaluate whether the vertical structure of negative height anomalies resembles more of an intensifying or a weakening type of mid-latitude cyclone. At this point it should be noted that although baroclinicity is more rare in the tropics, the tilt between the surface and upper level troughs in waves may be westward or eastward with height depending upon the synoptic environment it is embedded within (Riehl, 1954; Schapiro, 1986; Lau and Lau, 1990). Therefore, if tilt is observed in the tropical sections of the SPCZ, it could be difficult to determine whether the system is truly baroclinic. However, if the height anomaly pattern is weak it is likely I am dealing with very weak temperature gradients and hence a low vertical wind shear environment as opposed to a baroclinic one.

Figures 66 through 68 show the extent of 3mm/dy rain rates, 200, 500 and 850 hPa height anomalies for the TR, ST and ML SPCZ for composite Day 0. I have also included the zero contour line of the zonal wind of which I will discuss shortly. All of the composites show wave train patterns that are strongest at upper levels and weakest near the surface. The structure of the trough near the TR SPCZ region (figure 66) indicates a poleward tilt with increasing height from 500 to 200 hPa. However, the pattern in this region is very weak and questionable enough to conclude that the atmosphere is likely not baroclinic in nature, especially as the 200-850 hPa vertical wind shear in this region is predominantly in the 10 to 15 m/s range (as seen in figure 61). The negative height anomalies just southwest of the ST SPCZ region (figure 67) has a slight tilt poleward and eastward but are essentially stacked on top of each other. From quasi-geostrophic theory an eastward tilt with height to low pressure is indicative of a cyclone in a decaying stage (Holton, 1992). As the negative anomalies near the test region are in 20 to 30 m/s shear (see figure 61) I interpret the composite to predominantly represent cyclones that have

already reached maturity and have started weakening. The ML SPCZ (figure 68) is the only region where negative height anomalies exhibit a distinct westward tilt with increasing height two days prior to (not shown) and during HRRDs. In this region, it is clear the upper and lower level negative height anomalies substantially increase in magnitude as they approach the test region. As the negative height anomalies are located within 20 to 35 m/s 200-850 hPa vertical shear, it is likely that this composite represents intensifying baroclinic mid-latitude cyclones within this part of the SPCZ.

In both the ST and ML SPCZ, the placement of the zonal zero contour line at 500 hPa is just north of the rain rate anomaly pattern. Webster and Holton (1982) found that for Rossby wave energy to propagate from higher to lower latitudes, a duct of westerly winds, with a size comparable to the disturbance itself, must be present. At 500 hPa a duct of westerly wind is not found in either the ST or ML SPCZ and this could be interpreted to mean wave energy has been reflected by the easterly flow preventing cross-equatorial energy propagation. The zonal zero contour line at 200 hPa indicates westerly flow does exist north and east of the ST SPCZ. However, figure 59 shows no evidence of a height anomaly pattern continuing towards the equator. The author speculates that perhaps the combination of the easterly flow at 500 hPa and active convection that prevents wave energy from propagating across the equator. The author is not aware of any studies that suggest convection alone can refract wave energy but nonetheless I speculate that it may be possible.

Summary

Analysis of high and low rain rate events in the SPCZ revealed many interesting observations. High rain rate events are relatively rare in the data record yet they contribute disproportionately to the total rainfall in the region. Low rain rate events are more common, yet they contribute very little to the total rainfall. This suggests that composite analysis of high rain rates (HRRDs) and low rain rates (LRRDs) would be useful to examine. Rain rate histogram analysis showed

HRRDs are least common during the austral summer and fall in the TR and ST SPCZ; LRRDs are more common during winter and spring. The maximum in HRRDs is rather broad and distributed throughout spring through fall. HRRDs in the ML SPCZ have a bimodal distribution with the primary maximum and minimum occurring during late fall through winter and late winter through early spring respectively.

Composites of HRRDs exhibited well defined wave train patterns in the height anomaly fields for the ST and ML SPCZ. In the case of the ST SPCZ, the Day 0 composite exhibits a wave train pattern that extends approximately 12000 km across the South Indian and Pacific Oceans. The wavelength spacing for the wave trains range from 4800 to 5800 km and are slightly larger than the distance found between successive minima or maxima in the correlation analysis of chapter V. Individual height anomaly maxima and minima had a strong eastward component in the phase velocity with speeds of 6 to 8 m/s, about twice as fast as the speeds found from correlation maxima and minima in chapter V. It is unclear why there are considerable differences in phase velocity between the composites and the correlation analysis. The author speculates the differences could be related to the smaller subset of observations used in the composite. In the case of each SPCZ test region, a negative height anomaly was present at Day -2 and Day 0 of the composites. In the case of the TR SPCZ, the negative anomaly and the accompanying pattern is near the “noise” level of the data and little could be concluded other than the results are largely similar to those found in the rain rate vs. height anomaly correlation analysis. In the ST and ML SPCZ, negative height anomalies are much stronger and lay adjacent to the rain rate anomaly pattern on composite Day 0. The rain rate anomaly patterns, as expected, are highest on composite Day 0 and typically extend from 2600 to 4300 km in a northwest-to-southeast direction. Vertical wind shear for composite Day 0 clearly showed much stronger values in the ST and ML SPCZ during HRRDs.

For LRRD composites, wave train patterns of similar wavelengths and orientation were found although the patterns were approximately 180° out of phase with the HRRD composites. Shear values for Day 0 of LRRD composites indicate values comparable to that seen in the HRRD composites. Clearly, vertical shear is not a sufficient ingredient for the development of heavy rain in the ST and ML SPCZ. Instead, what is important is the presence of synoptic scale lift downstream from an approaching upper level trough. For the TR SPCZ, I speculate tropical wave activity is likely important to the development of heavy rain although I did not attempt to show this in this study.

The vertical structure of the height anomaly and zonal wind flow patterns for HRRDs were examined to determine if any baroclinic characteristics are present. Typically, the wave train patterns were stronger at the upper levels than in the lower levels of the atmosphere. In the TR SPCZ, the pattern was very weak and this, combined with 200 – 850 hPa shear values of 10 to 15 m/s, suggests an atmosphere dominated by latent heat processes. In the case of the ST SPCZ, negative height anomalies are tilted slightly poleward and eastward and this, combined with 20 to 30 m/s vertical shear values, suggests the composite represents cyclones that are past maturity. The westward tilt with height of the negative height anomalies in the ML SPCZ composite suggests the composite represents baroclinic cyclones that are intensifying.

Examination of the positions of the zonal mean zero contour line at 500 hPa does not reveal a large duct of westerly flow necessary for the propagation of wave energy equatorward. However, at 200 hPa a duct of westerly flow is present. Nonetheless, the height anomaly fields suggest energy does not continue equatorward but is reflected near the positive rain rate anomaly pattern towards the east. The author suspects that the combination of the lack of westerly flow at 500 hPa plus active convection is the reason the height anomaly pattern, and hence wave energy, does not continue equatorward.

CHAPTER VII

SUMMARY AND CONCLUSIONS

The focus of this research project was to provide answers to a number of questions concerning the nature of the SPCZ. To do this, I examined the horizontal and vertical structure of a number of physical parameters within the SPCZ for annual, seasonal and higher frequency oscillations.

The three year mean revealed a northwest-to-southeast oriented SPCZ rain rate maximum, the sub-tropical and mid-latitude portions of which lay across a significant gradient in SSTs. Not surprisingly, substantial vertical wind shear, hence baroclinicity, was also in these regions. Seasonal analysis indicated the presence of a single rain rate maximum during summer and fall that essentially splits into two maxima during winter and spring. During summer, rain rates in the tropical sections of the SPCZ reach their highest magnitudes and the maximum is oriented in a west-northwest-to-east-southeast direction. Vertical wind shear is present only over the poleward-most sections of the rain rate maximum, implying that much of the heavy rainfall during this season is likely related to equivalent barotropic dynamics. During fall, rain rates in the tropics begin to decrease but the rain rate maximum extends well into mid-latitudes with a northwest-to-southeast orientation. Substantial vertical wind shear is present over much of the rain rate maximum at sub-tropical and mid-latitudes suggesting the potential for baroclinic cyclone activity. Two rain rate maxima, one over tropical and another at higher latitudes, were present during winter and spring. Vertical wind shear and the variability of the meridional wind indicated the higher latitude rain rate maximum is nothing more than the equatorward extension of the Southern Hemisphere storm track during winter and, to a lesser extent, in spring. In the tropics, rainfall continues to occur within a low vertical wind shear environment.

Annual and seasonal analysis indicated surface convergence, SST and rain rate maxima were generally co-located along the NHITCZ and the tropical portions of the SPCZ. However, at subtropical and higher latitudes the rain rate maximum was over a region of cool SSTs and large areas of divergence. Even at seasonal time scales, substantial areas of divergence was present along the rain rate maximum at the higher latitudes. Seasonal analysis indicated surface convergence in the tropical sections of the SPCZ expanded eastward within a narrow corridor at equatorial latitudes during summer and fall. By fall, twin surface convergence and rain rate maxima were present in the equatorial regions of the Southern and Northern Hemisphere. These observations suggest atmospheric and oceanic dynamics may link tropical sections of the SPCZ to the development of the SEITCZ.

Examination of the NCEP 1000 hPa convergence field revealed a similar pattern as that observed in the satellite derived data; that is, convergence maxima are zonally oriented across the South Pacific. However, this pattern changes in the vertical as convergence becomes more closely co-located with the SPCZ rain rate maximum at 850 hPa and 700 hPa. It is during summer that boundary layer convergence is present throughout much of the SPCZ rain rate maximum. During other seasons, there is a substantial amount of surface divergence in sub-tropical and mid-latitudes of the SPCZ that cuts across the rain rate maximum. Scatter plots of rain rates vs. divergence across selected portions of the SPCZ showed that surface convergence is important to the development of clouds and precipitations in the tropics but much less important at sub-tropical and mid-latitudes. Seasonal scatter plots indicate an increase in the number of rain days with surface divergence from summer into fall and winter over sub-tropical and mid-latitude portions of the SPCZ. This suggests that clouds and precipitation are not produced by surface convergence, but rather by convergence above the surface or via the

mechanical lifting of moist atmospheric layers, both of which are associated with extra-tropical cyclones.

All of the results strongly suggest that throughout each season the SPCZ is composed of two distinct dynamical regions. In the tropics, warm SSTs, abundant boundary layer convergence and low vertical wind shear sets up a barotropic atmosphere where deep convection and copious amounts of rain persist throughout the year. In mid-latitude sections, cool SSTs and substantial vertical wind shear is indicative of a baroclinic environment where transient mid-latitude cyclones are likely important to the development of rainfall. The presence of surface divergence in the rain rate maximum is indicative of clouds and precipitation arising from regions of moisture convergence aloft or the forced lifting or moist air associated with passing mid-latitude cyclones (Matejka et al., 1980).

Comparisons of NCEP and satellite derived rain rates revealed substantial differences in the location of the SPCZ rain rate maximum, a characteristic observed by other investigators (such as Janowiak, et al. 1998). However, I also found that the satellite derived surface convergence pattern was more closely co-located with the NCEP rain rate maximum. As the surface convergence and SST maxima are co-located in the tropics I believe the results suggest the NCEP precipitation algorithm may be overly dependent on the SST field. Kalnay et al. (1996) indicates that a simplified Arakawa-Schubert convective parameterization developed by Pan and Wu (1994) is used to create the NCEP re-analysis precipitation fields. Pan and Wu (1994) noted that the changes in the convective parameterization allowed for “a more realistic precipitation-SST correlation.” Parameterization changes and their relationship to the SST fields are not explicitly discussed in the paper; therefore the authors cannot comment on why NCEP precipitation fields appear overly dependent on SST fields.

Next I learned through lag correlation analysis that, in a statistical sense, the entire SPCZ region does not become convectively active for a given time period on a regular basis. Instead, the results suggest that convection develops in close proximity to a given SPCZ region then propagates east-southeastward for about 500 to 1000 km. The results suggest convection may propagate, to a certain extent, into adjacent regions of the SPCZ but generally does not travel from the tropics into middle latitudes. It should be noted that rain rates in tropical sections of the SPCZ are only weakly related to rain rates in the mid-latitude sections. These weak correlations could be due to the presence of high rain rate events in the data that are relatively rare.

Correlations between rain rates in the sub-tropical and mid-latitude portions of the SPCZ vs. middle and upper level height anomalies revealed wave train patterns in the South Pacific. The wavelengths ranged from 4600 to 5000 km which are slightly smaller than wavelengths observed in meridional wind data by Kalnay et al. (1986). The wave trains exhibited a west-southwest-to-east-northeast orientation suggesting that mid-latitude energy could be propagating from higher to lower latitudes. Additionally, the results indicate positive rain rate anomalies occur on the eastern side of middle and upper level troughs in sub-tropical and mid-latitude portions of the SPCZ. These results complement those found in chapter IV and suggest that mid-latitude cyclones play an important part in producing rainfall in these regions.

High rain rate days in the SPCZ, depending on the location within the SPCZ, contribute from 37 to 47 percent of the total rainfall despite making up approximately 14 percent of the data record. The reverse was true for low rain rate days as they made up about a quarter of the data set, yet contributed very little to the total rainfall. This means much of the rainfall in the SPCZ is based on relatively rare events and that there are a large number of days where very little rainfall occurs. On the basis of these findings, I made high and low rain rate composites for different sections of the SPCZ. High rain rate days (HRRDs) showed a distinct seasonality as

they are more common during summer and fall in the TR and ST SPCZ and during late fall and early winter in the ML SPCZ. Low rain rate days (LRRDs) are more common during winter and spring in the TR and ST SPCZ and during late winter and early spring in the ML SPCZ. In terms of these rain rate classifications, the distinct seasonality in HRRDs and LRRDs continues to illustrate the difference between tropical and middle latitude sections of the SPCZ. In terms of the seasonal characteristics of HRRDs and LRRDS, the ST SPCZ is more similar to the TR SPCZ than the ML SPCZ.

Composites of HRRDs exhibited well defined wave train patterns in the height anomaly fields for the ST and ML SPCZ. Wavelengths ranged from 4800 to 5800 km or slightly larger than the spacing between successive correlation maxima or minima in chapter V. On composite Day 0 in the ST and ML SPCZ, an upper level trough was immediately upstream from positive rain rate anomalies with ample amounts of vertical wind shear present. The horizontal and vertical structure of the trough in the ML SPCZ is characteristic of an intensifying baroclinic cyclone. In the ST SPCZ, the height anomaly progression in the composites is very suggestive of the southern portion of a mid-latitude trough elongating with time then becoming isolated from mid-latitude westerly flow, so called “cut off” lows. On composite Day 0, negative height anomalies only show a slight eastward and poleward tilt in the ST SPCZ and this combined with the ample amounts of vertical shear would be consistent with a “cut off” low. In the TR SPCZ, the composite patterns are fairly weak and this combined with low vertical wind shear suggests that HRRDs are more likely associated with equivalent barotropic dynamics. Composites of the raw rain rate patterns suggest that strong convection occurs only in a portion of the SPCZ and does not typically extend from the tropics into the mid-latitudes. However, lighter rain and weak convection may extend clear from the tropical well into sub-tropical latitudes. Interestingly enough, the LRRD composites exhibited wave train patterns that were 180° out of phase with the

HRRD composites. Additionally, vertical shear during theses events were very similar to that seen in the HRRD composites. This highlights the importance of an upper level trough to provide the dynamics necessary for heavy rainfall in the sub-tropical and mid-latitude portions of the SPCZ.

At this point, I need to go back and determine if I have answered the questions I asked at the beginning of this study. First, I wanted to know what kind of relationship exists between convection in tropical and middle latitude sections of the SPCZ. The answer is that during most heavy rainfall events, there is little relationship between strong convection in tropical and middle latitude portions of the SPCZ. That is, only a given portion of the SPCZ becomes convectively active at a given time. However, during these high rain rate days, stratiform and weak convective rain may extend from the tropics into the mid-latitudes. I also wanted to know if there were any seasonal variations to the SPCZ rain rate maximum and the answer is yes. In fact, much of the heavy rain rate events in mid-latitudes sections of the SPCZ occur during late fall and winter and are strongly associated with the Southern Hemisphere storm track. Heavy rain in the TR and ST SPCZ is more likely to occur during summer and fall.

I also wanted to know how important mid-latitude cyclones are to the development of rainfall within the SPCZ. The answer is they appear to be quite important in the ML SPCZ, and to a lesser extent in the ST SPCZ during high rain rate events. In the sub-tropical portions of the SPCZ our analysis suggests passing mid-latitude troughs may fracture with the equatorward sections becoming isolated from mid-latitude westerly flow. This cut-off upper low is still important to the development of clouds and precipitation within this section of the SPCZ. Height anomaly patterns suggest energy is propagating from higher latitudes into and out of the ST and ML SPCZ during heavy rain events again suggesting the importance of mid-latitude

dynamics. However, in the tropics the results are weak enough to draw the conclusion that mid-latitude cyclones don't affect this region the majority of the time.

This research project also generated some new questions. Are events in parts of the Western South Pacific somehow related to the development of the SEITCZ? Or, is the development of the SEITCZ in the Eastern South Pacific causing changes in the convergence pattern in the Western South Pacific? The weak results from the correlation and composite analysis in the TR SPCZ suggested that baroclinic dynamics are not important to the development of heavy rainfall events. However, it would be interesting to see if there are notable cases where mid-latitude dynamics had a strong affect on tropical convection and to see if wave train patterns would indicate the propagation of energy from higher to lower latitudes. Additionally, there is still the question of why rain preferentially develops within this part of the world? These topics are prime areas for future research.

REFERENCES

Adler, R. F., A. J. Negri, P. E. Keehn and I. M. Hakkarinen, 1993: Estimation of Monthly Rainfall over Japan and Surrounding Waters from a Combination of Low-Orbit Microwave and Geosynchronous IR Data. *J. App. Met*., **32**, 335-356

Arkin, P. A., 1979: The Relationship between Fractional Coverage of High Cloud and Rainfall Accumulations during GATE over the B-Scale Array. *Mon. Wea. Rev*., **107**, 1382-1387

Arkin, P. A. and B. N. Meisner, 1987: The Relationship between Large-Scale Convective Rainfall and Cold Cloud over the Western Hemisphere during 1982-84. *Mon. Wea. Rev*., **115**, 51-74

Bourassa, M. A., 2002: Personal Communication, Florida State University, Tallahassee, FL

Bourassa, M. A., D. M. Legler, J. J. O'Brien and S. R. Smith, 2003: Sea Winds Validation with Research Vehicles. *J. Geophys. Res*, **108**, 1-16

Berg, W., C. Kummerow and C. A. Morales, 2002: Differences between East and West Pacific Rainfall Systems. *J. Climate*., **15**, 3659-3672

Emery, W. J., S. Castro, G. A. Wick, P. Schluessel and C. Donlon, 2001: Estimating Sea Surface Temperature from Infrared Satellite and In Situ Temperature Data. *Bull. Amer. Meteor. Soc*., **82**, 2773-2784

Gill, A. E., 1980: Some Simple Solutions for Heat Induced Tropical Circulation. *Quart. J. Roy. Meteor. Soc*., **106**, 447-462

Gill, A. E., 1982: *Atmosphere-Ocean Dynamics*. Academic Press. 662 pp

Godshall, F. A., 1968: The Intertropical Convergence Zone and Mean Cloud Amount in the Tropical Pacific Ocean. *Mon. Wea. Rev*., **96**, 172-175

Graham, N. E. and T. P. Barnett, 1987: Sea Surface Temperature, Surface Wind Divergence, and Convection over Tropical Oceans. *Science*, **238**, 657-659

Gray, W. M., 1968: Global View of the Origin of Tropical Disturbances and Storms. *Mon. Wea. Rev*., **96**, 669-700

Gray, W. M., 1975: Tropical Cyclone Genesis. Dept. Atmos. Sci. Paper 323, Colorado State University, Fort Collins, CO

Gray, W. M. and R. W. Jacobson, 1977: Diurnal Variation of Deep Cumulus Convection. *Mon. Wea. Rev*., **105**, 1171-1188

Gruber, A., 1972: Fluctuations in the Position of the ITCZ in the Atlantic and Pacific Oceans. *J. Atmos. Sci*., **29**, 193-197

Hendon, H. H., 1986: The Time-Mean Flow and Variability in a Non-Linear Model of the Atmosphere with Tropical Diabatic Forcing. *J. Atmos. Sci*., **43**, 72-88

Holton, J. R., 1992: *An Introduction to Dynamic Meteorology*. Academic Press, 149 pp

Houze, R. A., 1993: *Cloud Dynamics*. Academic Press, Inc., 438 pp

Houze, R. A., 1997: Stratiform Precipitation in Regions of Convection: A Meteorological Paradox? *Bull. Amer. Meteor. Soc.*, **78**, 2179-2196

Huang, H-J and D.G. Vincent, 1983: Major Changes in Circulation Features over the South Pacific During FGGE, 10-27 January 1979. *Mon. Wea. Rev*., **111**, 1611-1618

Huffman, G. J., R. F. Adler, P. Arkin, A. Chang, R. Ferraro, A. Gruber, J. Janowiak, A. McNab, B. Rudolf and U. Scneider, 1997: The Global Precipitation Climatology Project (GPCP) Combined Precipitation Dataset. *Bull. Amer. Meteor. Soc.*, **78**, 5-20

Huffman, G. J., R. F. Adler, P. Arkin, M. M. Morrissey, D. T. Bolvin, S. Curtis, R. Joyce, B. McGavock, and J. Susskind, 2001: Global Precipitation at One-Degree Daily Resolution from Multisatellite Observations. *J. Hydromet*., **2**, 36-50

Huffman, G. J., 2002: Personal Communication, NASA Goddard Space Flight Center, Silver Springs, MD

Hurrell, J. W., H. van Loon and D. J. Shea, 1998: The Mean State of the Troposphere. *Meteorology of the Southern Hemisphere, Meteor. Monogr*., No. 49, Amer. Meteor. Soc, 1-46

Janowiak, J. E., A. Gruber, C. R. Kondragunta, R.E. Livezey, G. J. Huffman, 1998: A Comparison of the NCEP-NCAR Reanalysis Precipitation and the GPCP Rain Gauge-Satellite Combined Dataset with Observational Error Considerations. *J. Climate*, **11**, 2960-2979

Kalnay, E., K. C. Mo and J. Paegle 1986: Large Amplitude, Short-Scale Stationary Rossby Waves in the Southern Hemisphere: Observations and Mechanistic Experiments to Determine Their Origin. *J. Atmos. Sci.*, **43**, 252-275

Kalnay, E., M. Kanamitsu, R. Kistler, W.Collins, D. Deaven, L. Gandin, M. Iredell, S. Saha, G. White, J. Woolen, Y. Zhu, M. Chelliah, W. Ebisuzaki, W. Higgins, J. Janowiak, K. C. Mo, C. Ropelewski, J. Wang; A. Leetmaa, R. Reynolds, R. Jenne and D. Joseph; 1996: The NCEP/NCAR 40-Year Reanalysis Project. *Bull. Amer. Meteor.* Soc., **77**, 437-471

Kidder, S. Q. and T. H. Vonder Haar, 1995: *Satellite Meteorology: An Introduction*. Academic Press Inc., 245-248

Kiladis, G. N.; H. von Storch and H. van Loon, 1989: Origin of the South Pacific Convergence Zone. *J. Climate*, **2**, 1185-1195

Kiladis, G. N. and K. M. Weickmann, 1992a: Circulation Anomalies Associated with Tropical Convection during Northern Winter. *Mon. Wea. Rev*., **120**, 1900-1923

Kiladis, G. N. and K. M. Weickmann, 1992b: Extratropical Forcing of Tropical Pacific Convection during Northern Winter. *Mon. Wea. Rev*., **120**, 1924-1938

Kistler, R., E. Kalnay; W. Collins, S. Saha, G. White, J. Woollen, M. Chelliah, W. Ebisuzaki, M. Kanamitsu, V. Kousky, H. Van Den Dool, R. Jenne and M. Fiorino, 2001: The NCEP-NCAR 50 Year Reanalysis Monthly Means CD-ROM and Documentation. *Bull. Amer. Meteor. Soc*., **82,** 247-267

Kodama, Y., 1992: Large-Scale Common Features of Subtropical Precipitation Zones (the Baiu Frontal Zone, the SPCZ and the SACZ): Part I: Characteristics of Subtropical Frontal Zones. *J. Meteor. Soc. Japan*, **70**, 813-834

Kodama, Y., 1993: Large-Scale Common Features of Subtropical Precipitation Zones (the Baiu Frontal Zone, the SPCZ and the SACZ): Part II: Conditions of the Circulations for Generating the STCZs. *J. Meteor. Soc. Japan*, **70**, 581-608

Kodama, Y., 1999: Roles of the Atmospheric Heat Sources in Maintaining the Subtropical Convergence Zones: An Aqua Planet GCM Study. *J. Atmos. Sci*., **56**, 4032-4049

Kummerow C., L. Giglio, 1995: A Method for Combining Passive Microwave and Infrared Rainfall Observations. *J. Atmos. & Ocn. Tech*., **12**, 33-45

Kummerow C., W. Barnes, T. Kozu, J. Shiue and J. Simpson, 1998: The Tropical Rainfall Measuring Mission (TRMM) Sensor Package. *J. Atmos. & Ocn. Tech*., **15**, 809-817

Lau, K-H and Lau N-C, 1990: Observed Structure and Propagation Characteristics of Tropical Summertime Synoptic Scale Disturbances. *Mon. Wea. Rev*., **118**, 1888-1913

Lucas, C., E. J. Zipser and M. A. Lemone; 1994: Vertical Velocity in Oceanic Convection off Tropical Australia. *J. Atmos. Sci*., **51**, 3183-3193

Mapes, B. E. and R.A. Houze; 1993: Cloud Clusters and Superclusters over the Oceanic Warm Pool. *Mon. Wea. Rev*., **121**, 1398-1415

Mapes, B. E. and R.A. Houze; 1995: Diabatic Divergence Profiles in Western Pacific Mesoscale Convective Systems. *J. Atmos. Sci*., **52**, 1807-1828

Matejka, T. J., R. A. Houze, P. V. Hobbs; 1980: Microphysics and Dynamics of Clouds Associated with Mesoscale Rainbands in Extra-tropical Cyclones. *Quart. J. R. Met. Soc*., 29-56

McBride, J. L. and W. M. Gray; 1980: Mass Divergence in Tropical Weather Systems: Paper I. *Quart. J. R. Met. Soc*., 501-516

Mitchell, T. P. and J. M. Wallace, 1992: The Annual Cycle in Equatorial Convection and Sea Surface Temperature. *J. Climate*, **5**, 1140-1156

Mohr, K. I., J. S. Famiglietti, E. J. Zipser, 1999: The Contribution to Tropical Rainfall with respect to Convective System Type, Size, and Intensity Estimated from the 85-GHz Ice-Scattering Signature. *J. App. Met*., **38**, 596-606

Montgomery, D. C. and G. C. Runger, 1999: *Applied Statistics and Probability for Engineers*. John Wiley & Sons Inc., 282-284 and 328

Pan, H-L and W-S Wu, 1994: Implementing a Mass Flux Convective Parameterization Package for the NMC Medium-Range Model. Preprints, *10th Conf. on Numerical Weather Prediction*, Portland, OR, 96-98

Pegion, P. J., M. A. Bourassa, D. M. Legler and J. J. O'Brien, 2000: Objectively Derived Daily "Winds" from Satellite Scatterometer Data. *Mon. Wea. Rev*., **128**, 3150-3168

Putman, W. M., D. M. Legler and J. J. O'Brien, 1999: Interannual Variability of Synthesized FSU and NCEP-NCAR Reanalysis Pseudostress Products over the Pacific Ocean. *J. Clim*ate, **13**, 3003-3016

Randel, W. J. and J. L. Stanford, 1985: An Observational Study of Medium-Scale Wave Dynamics in the Southern Hemisphere Summer. Part I: Wave Structure and Energetics. *J. Atmos. Sci.*, **42**, 1172-1188

Rao, V. B., A. M. C. Do Carmo and S. H. Franchito, 2002: Seasonal Variations in the Southern Hemisphere Storm Tracks and Associated Wave Propagation. *J. Atmos. Sci.*, **59**, 1029-1040

Richards, F. and P. Arkin, 1981: On the relationship between satellite-observed cloud cover and precipitation. *Mon. Wea. Rev*., **109**, 1081-1093

Riehl, H., 1954: *Tropical Meteorology*. McGraw-Hill, 392 pp.

Sadler, J. C., 1975: The Upper Tropospheric Circulation Over The Global Tropics. Technical Bulletin UHMET-75-05, Department of Meteorology, University of Hawaii, Manoa, HI

Sadler, J. C., 1987: Tropical Marine Climatic Atlas, Volume II: Pacific Ocean. Technical Bulletin 87-02, Department of Meteorology, University of Hawaii, Manoa, HI

Schapiro, L. J., 1986: The Three Dimensional Structure of Synoptic Scale Disturbances over the Tropical Atlantic. *Mon. Wea. Rev*., **114**, 1876-1891

Schlax, M. G., D. B. Chelton and M. H. Freilich, 2000: Sampling Errors in Wind Fields Constructed from Single and Tandem Scatterometer Datasets. *J. Atmos. Ocn. Tech*., **1**8, 1014-1036

Schrage, J. M. and D. G. Vincent, 1996: Tropical Convection on 7 - 21 Day Timescales over the Western Pacific. *J. Climate*, **9**, 587-607

Serke, D. J., 1996: Evolution of the Southeast Pacific ITCZ in Boreal Spring as Viewed From SSM/I and SSM/T2, M.S.Thesis, Texas A&M University

Sinclair, M. R., 1994: An Objective Cyclone Climatology for the Southern Hemisphere. *Mon. Wea. Rev*., **122**, 2239-2256

Spencer, R. W., 1993: Global Oceanic Precipitation from the MSU during 1979-91 and Comparisons to Other Climatologies. *J. Climate*, **6**, 1301-1326

Streten, N. A., 1973: Some Characteristics of Satellite Observed Bands of Persistent Cloudiness over the Southern Hemisphere. *Mon. Wea. Rev*., **101**, 486-494

Streten, N. A., 1978: A Quasi-Periodicity in the Motion of the South Pacific Cloud Band. *Mon. Wea. Rev*., **106**, 1211-1214

Susskind, J., P. Piraino, L. Rokke, L. Iredell and A. Mehta, 1997: Characteristics of the TOVS Pathfinder Path-A Dataset. *Bull. Amer. Meteor. Soc.*, **78**, 1449-1472

Trenberth, K.E., 1976: Spatial and Temporal Variations of the Southern Oscillation. *Quart. J. Roy. Meteor. Soc*., **102**, 639-653

Trenberth, K.E. and D. J. Shea, 1987: On the Evolution of the Southern Oscillation. *Mon. Wea. Rev*., **115**, 3079-3096

Trenberth, K.E., 1991: Storm Tracks in the Southern Hemisphere. *J. Atmos. Sci*., **48**, 2159-2178

Vincent, D. G., 1982: Circulation Features over the South Pacific during 10-18 January 1979. *Mon. Wea. Rev*., **110**, 981-992

Vincent, D. G., 1985: Cyclone Development in the South Pacific Convergence Zone during FGGE, 10-17 January 1979. *Quart. J. R. Met. Soc*., **111**, 155-172

Vincent, D. G., 1994: The South Pacific Convergence Zone (SPCZ): A Review. *Mon. Wea. Rev*., **122**, 1949-1970

Vincent, D. G., 1998: Meteorology of the Tropics: The Pacific Ocean. *Meteorology of the Southern Hemisphere, Meteor. Monogr*., No. 49, Amer. Meteor. Soc., 101-117

Waliser, D. E.; C. Gautier, 1993: A Satellite Derived Climatology of the ITCZ. *J. Climate*, **6**, 2162-2174

Wallace J. M. and P. V. Hobbs, 1977: *Atmospheric Science, An Introductory Survey*. Academic Press, Inc.

Wallace, J. M., T. P. Mitchell and C. Deser, 1989: The Influence of Sea Surface Temperature on Surface Wind in the Eastern Equatorial Pacific: Seasonal and Interannual Variability. *J. Climate*, **2**, 1492-1499

Webster, P. J. and J. R. Holton, 1982: Cross Equatorial Response to Middle-Latitude Forcing in a Zonally Varying Basic State. *J. Atmos. Sci.*, **39**, 722-733

Weissman, D. E., M. A. Bourassa and J. Tongue, 2002: Effects of Rain Rate and Wind Magnitude on SeaWinds Scatterometer Wind Speed Errors. *J. Atmos. Oceanic Technol*., **19**, 738-746

Wentz, F. J., C. Gentemann, D. Smith and D. Chelton, 2000: Satellite Measurements of Sea Surface Temperature through Clouds. *Science*, **288**, 847-850

Wilheit, T. T. , J. S. Theon, W. E. Shenk and L. J. Allison, 1976: Meteorological Interpretations of the Images from the Nimbus 5 Electrically Scanned Microwave Radiometer. *J. App. Met*., **15**, 166-172

Wilheit, T. T., A. T. C. Chang, M. S. V. Rao, E. B. Rodgers and J. S. Theon, 1977: A Satellite Technique for Quantitatively Mapping Rainfall Rates over the Oceans. *J. App. Met*., **16**, 551-560

APPENDIX

CROSS-CORRELATION USING FOURIER ANALYSIS

The Fourier transform of a function f(t) is defined as:

$$F(w)=(1/2\pi)^{1/2}\int f(t)e^{-iwt}dt \qquad \text{A-1)}$$

where 'F(w)' is the Fourier Transform, 'w' denotes frequency space and the integral is taken from $-\infty$ to $+\infty$. Note that the new function created is now in frequency space; the Fourier transform of F(w) is given by:

$$f(t)=(1/2\pi)^{1/2}\int F(w)e^{iwt}dt \qquad \text{A-2)}$$

The normalized spectrum of a function f(t) is given by:

$$S(w)=F^{*}(w)F(w) \qquad \text{A-3)}$$

where '$F^{*}(w)$' is the complex conjugate of 'F(w).' To shorten the notation, the Fourier transform will be denoted as 'FT' from this point on. Now, the autocorrelation function for f(t) is nothing more than the Fourier transform of the spectrum divided by the variance of f(t):

$$A(t)=FT[S(w)/\sigma_t^2] \qquad \text{A-4)}$$

where 'A(t)' is the autocorrelation function and 'σ_t^2' is the variance of f(t). Lag correlation is an extension of eq. 4) except we are introducing a new function g(t) such that it's Fourier transform is given by:

$$G(w)=(1/2\pi)^{1/2}\int g(t)e^{-iwt}dt \qquad \text{A-5)}$$

and the cross spectrum of f(t) with g(t) is given by:

$$CS_{fg}(w)=F^{*}(w)G(w) \qquad \text{A-6)}$$

We go one step further to find the forward lag correlation of f(t) with g(t) using:

$$CR_f(t)=FT[CS_{fg}(w)/(\sigma_{f(t)}\,\sigma_{g(t)})^{1/2}] \qquad \text{A-7)}$$

where '$CR_f(t)$' is the forward lag correlation of f(t) with g(t) and is a vector containing the correlation coefficients for each lag; '$\sigma_{f(t)}$' and '$\sigma_{g(t)}$' are the standard deviations of f(t) and g(t)

respectively. As an example, $CR_f(0)$ represents the correlation of f(0) with g(0) while $CR_f(0)$ represents the correlation of f(0) with g(5). The correlation coefficients for backward time lags are given by:

$$CS_{fg}(w)=G^{*}(w)F(w) \quad \text{A-8)}$$

$$CR_b(t)=FT[CS_{gf}(w)/(\sigma_{f(t)}\,\sigma_{g(t)})^{1/2}] \quad \text{A-9)}$$

In our present study, f(t) will represent the spacially averaged time series for a given parameter and test region while g(t) will represent a time series for a different (or the same) parameter at various gridpoints.

VITA

Stephen B. Cocks was born in Birmingham, Alabama on January 3, 1964. He graduated from the Alabama School of Fine Arts in May of 1982 with an emphasis on, of all things, classical guitar. He earned his Bachelor of Science in meteorology from the University of Oklahoma in August of 1992. Shortly thereafter he was commissioned into the United States Air Force and continues to serve in the military up to the date of this dissertation. It is through the military services that he has learned a wealth of operational forecasting experience over the years at locations ranging from “Tornado Alley” in Oklahoma to “Typhoon Alley” in the Western Pacific. He earned his Master of Science in atmospheric sciences from Colorado State University in June of 1997. He entered the Ph.D. program at Texas A&M University in August 2000.

Correspondence during transitional periods may be directed to Stephen B. Cocks, 3435 Kildare Drive, Hoover, AL, 35266.